



UNIVERSIDADE FEDERAL DE SANTA CATARINA
CENTRO TECNOLÓGICO
PROGRAMA DE PÓS-GRADUAÇÃO EM ENGENHARIA MECÂNICA

Valquíria Bomfim Fernandes

Experimental and theoretical studies of a PCM heat storage system coupled with a two-phase thermosyphon

Florianópolis
2022

Valquíria Bomfim Fernandes

Experimental and theoretical studies of a PCM heat storage system coupled with a two-phase thermosyphon

Dissertação/Tese submetida ao Programa de Pós-Graduação em Engenharia Mecânica da Universidade Federal de Santa Catarina para a obtenção do título de Mestre em Engenharia Mecânica.
Orientador: Prof. Fernando H. Milanese, Dr. Eng.
Coorientador: Prof. Luis Hernán Rodríguez Cisterna, Dr. Eng.

Florianópolis

2022

Ficha de identificação da obra elaborada pela autora,
através do Programa de Geração Automática da Biblioteca Universitária da UFSC.

Fernandes, Valquíria

Experimental and theoretical studies of a PCM heat storage system coupled with a two-phase thermosyphon / Valquíria Fernandes; orientador, Fernando Henrique Milanese, coorientador, Luis Hernán Rodríguez Cisterna, 2022.

132 p.

Dissertação (mestrado) - Universidade Federal de Santa Catarina, Centro Tecnológico, Programa de Pós-Graduação em Engenharia Mecânica, Florianópolis, 2022.

Inclui referências.

1. Engenharia Mecânica. 2. Thermal energy storage. 3. Phase change material. 4. Closed two-phase thermosyphon. 5. Solidification. I. Milanese, Fernando Henrique. II. Rodríguez Cisterna, Luis Hernán. III. Universidade Federal de Santa Catarina. Programa de Pós-Graduação em Engenharia Mecânica. IV. Título.

Valquíria Bomfim Fernandes

**Experimental and theoretical studies of a PCM heat storage system coupled
with a two-phase thermosyphon**

O presente trabalho em nível de mestrado foi avaliado e aprovado por banca
examinadora composta pelos seguintes membros:

Prof. Marcia B. H. Matelli, Ph.D

Universidade Federal de Santa Catarina (UFSC)

Prof. Juan Pablo Florez Mera, Dr.Eng.

Universidad de Pamplona

Prof. Samuel Luna Abreu, Dr.Eng.

Instituto Federal de Educação, Ciência e Tecnologia de Santa Catarina (IFSC)

Certificamos que esta é a **versão original e final** do trabalho de conclusão que foi
julgado adequado para obtenção do título de mestre em Engenharia Mecânica.

Prof. Paulo de Tarso R. de Mendonça, Dr. Eng.

Coordenador do Programa

Prof. Fernando H. Milanese, Dr. Eng

Orientador

Florianópolis, 2022.

To my parents, who always believed in me.

AGRADECIMENTOS

Agradeço primeiramente aos meus pais, Aparecida e Henrique, pela fé que sempre tiveram em mim, sem reservas, e por todo o apoio que me deram. Agradeço ao meu irmão Átila e à minha cunhada Verônica pelo incentivo e suporte. Eu gostaria de ter palavras melhores para expressar a imensa sorte que é ter o apoio da minha família.

Agradeço ao meu coorientador, Dr. Luis Hernán Rodríguez Cisterna, que esteve presente e me ajudou durante toda a pesquisa, por todas as turbulências. Além da orientação, obrigada por me emprestar um pouco da sua perseverança e coragem. Ao meu orientador Dr. Fernando H. Milanese pelos conselhos e atenção.

Agradeço também à equipe do LABTUCAL, em especial Andreza, Leandro, Juan, Nelson e João Victor. Aos colegas de equipe da Alta Temperatura: Felipe “Mineiro”, Fernando, Luciano, Alice, Gianpiero e Élviz.

Aos meus amigos, que compartilharam essa estrada comigo e que levarei do mestrado para o resto da vida: Alice, Thianne, Iana, Larissa, Mateus e Élviz.

Por fim agradeço ao CNPq - Conselho Nacional de Desenvolvimento Científico e Tecnológico – pela concessão de uma bolsa de mestrado, e à UFSC pela oportunidade.

It is no little matter, this round and delicious globe, moving so exactly in its orbit
forever and ever, without one jolt or the untruth of a single second.

(WHITMAN, 1855)

ABSTRACT

Thermal energy storage using phase change materials suffers from low energy efficiency as the material typically absorbs energy at high heat transfer rates and releases energy at low heat transfer rates. Despite recent efforts to improve the storage system's overall heat transfer coefficient, the problem lies in the nature of the liquid – solid phase change, since the phase change material immediately adjacent to a heat exchanger solidifies first, forming a solid layer with low thermal conductivity that insulates the heat exchanger surface from the remaining liquid material. The present work investigates the early stages of PCM heat release, in order to study of the effectiveness of latent heat storage as a function of solid layer thickness, and defines a critical layer thickness beyond which heat transfer becomes too ineffective. In order to test the hypothesis that the highest discharge rates occur during the formation of this critical layer, a visualization experiment was conducted. The experiments used a closed two-phase thermosyphon charged with refrigerant R141-b as the heat exchanger, and a container filled with naphthalene as the phase change material. The evaporator of the two-phase thermosyphon was inserted into the phase change material container, and the condenser was initially left exposed to ambient air for visualization, and later inserted in a wind tunnel for more controlled experiments. The temperatures and heat transfer rates were measured during both steady state operation and transient discharge. The visualization results confirmed the hypothesis of the critical layer. From the experiments with the wind tunnel, proposed correlations agreed with the experimental data within a maximum error of $\pm 25\%$ and a mean error of $\pm 13\%$. These results are considered satisfactory as a simplified model for a complex heat transfer phenomenon. The models proposed here can be used as design tools for phase change materials coupled with heat exchangers, in order to improve the energy efficiency during latent heat extraction and in order to optimize the volume to surface area ratio of the heat exchanger, avoiding the waste of valuable resources such as storage room, construction materials and stored energy.

Keywords: Thermal energy storage. Phase change material. Closed two-phase thermosyphon. Refrigerant R141-b. Naphthalene. Solidification.

LIST OF FIGURES

Figure 2.1. Schematics of the operating principle of a closed two-phase thermosyphon. Adapted from Mantelli (2021).....	19
Figure 2.2. Merit number (solid lines) and saturation pressure (dashed lines) as functions of operating temperature for selected low and medium temperature working fluids (BELLANI, 2017).	20
Figure 2.3. Simplified schematic of the experimental solar air heating system, using PCM storage units in a cascade configuration. Adapted from Diao <i>et al.</i> , 2021.	24
Figure 2.4. Structure of the LHSU detailing the different operating sections of the heat pipe depending on the phase of the charge-discharge cycle. Adapted from Diao <i>et al.</i> , 2021.	24
Figure 2.5. Simulation results for a complete charge/discharge cycle of a PCM in a shell-tube heat exchanger in vertical orientation. The water flows in the inner pipe from top to bottom. Figure (a): recorded melt percentage and water temperature;(b): a snapshot of PCM state (2D, cut through the middle) at 20 and 80 min, respectively. Adapted from Luu <i>et al.</i> (2020).	27
Figure 2.6. Two distinct TBL (thermal barrier layer) topologies, and their effect on the water outlet temperature (WOT) during PCM solidification. On the left is the most undesirable case, and on the right is the desirable outcome, using optimized design parameters. Adapted from Luu <i>et al.</i> (2020).	27
Figure 2.7. Water outlet temperature during discharge, for the base case (blue solid line), and for improved PCM tube designs 1 (black solid line) and 2 (red solid line). Adapted from Luu <i>et al.</i> (2020).	28
Figure 2.8. Liquid fractions at selected time instants during solidification, where t_f, s^* is the time required for full solidification in the optimized design. Adapted from Pizzolato <i>et al.</i> (2017).	29
Figure 2.9. Average conductive and convective heat transfer rates during solidification. Adapted from Pizzolato <i>et al.</i> (2017).	30
Figure 3.1. Diagram of the experimental setup: (1) ultra-high temperature heating tape Omega STH series;(2) power supply MCE 1310; (3) data acquisition system CR1000 Datalogger, Campbell Scientific; (4) computer; (5) twenty type K thermocouples Omega; (6) wind tunnel; (7) frequency inverter; (8) closed two-phase thermosyphon ; (9) Swagelok SS series valve; (10) PCM container.	32

Figure 3.2. Picture of the full experimental setup showing components as described in Figure 3.1.....	32
Figure 3.3. Test section: a) covered with insulating glass wool; b) bare.	33
Figure 3.4. Helium leak detector, Pfeiffer Vacuum ASM 340.....	36
Figure 3.5. Closed two-phase thermosyphon being evacuated by a liquid ring vacuum pump.	36
Figure 3.6. Charging of the thermosyphon with refrigerant R141b.....	38
Figure 3.7. Melting and measuring of naphthalene.....	38
Figure 3.8. Diagram of the thermocouple placement on the thermosyphon and PCM container, according to Table 3.3.	39
Figure 4.1. Energy balances considered for the steady state analysis, over control volumes, C.V., signaled by dashed lines surrounding: (a) the PCM container; (b) the thermosyphon.	49
Figure 4.2. Simplified thermal resistance circuit for the complete system, combining both energy balances in Figure 4.1.....	49
Figure 4.3. Thermal resistance circuit of a closed two-phase thermosyphon. Adapted from Mantelli (2021).	50
Figure 4.4. Two-dimensional rectangular enclosure with isothermal side walls. Adapted from Bejan (2013).....	56
Figure 4.5. Energy balances on the control volumes, C.V., defined by dashed lines: (a) PCM container, where q_{PCM} is the heat rate leaving the PCM; (b) thermosyphon, which receives q_{PCM} from the PCM container, and releases q_{out} to the heat sink (wind tunnel)..	61
Figure 4.6. Simplified thermal resistance circuit for the energy balance of Figure 4.5 (b).	62
Figure 5.1. Nusselt versus Reynolds for tests A to I (Table 3.5), and comparison with three correlations from the literature, and one semi-empiric correlation proposed in this study.	77
Figure 5.2. Close-up photo of the thermosyphon condenser confined inside the wind tunnel.	78
Figure 5.3. Scatter plot of the predicted versus experimental values of Nusselt number for tests A to I (Table 3.5), using the semi-empiric correlation.	78
Figure 5.4. Scatter plot of the proposed versus experimental Nusselt numbers for tests J to Q (Table 3.5).	79

Figure 5.5. Temperature variation with time for Test 1 (Table 3.4), using PCM container A: (1) steady state; (2) power supply shut down; (3) beginning of the critical solidification period, at $T_e = T_{e,0}$; (4) peak latent heat rate; (5) end of critical solidification period, at $T_e = T_{e,0}$; (6) power supply restored. Interval (A), in red, marks the liquid sensible cooling regime; interval (B) in purple stands for latent cooling; and interval (C) in blue represents the solid sensible cooling regime. 81

Figure 5.6. Temperature variation with time for Test 2 (Table 3.4), using PCM container A and interrupted by removing the evaporator from the PCM. Interval (A), in red, marks the liquid sensible cooling regime; and interval (B) in purple stands for latent cooling. The solid sensible cooling regime is not present here, due to the extraction from the PCM. ..83

Figure 5.7. Pictures of the evaporator after removal from PCM container A ($D_o = 2''$), from Test 2 (Table 3.4): a) next to a steel ruler, for scale; b) close up near the top of the evaporator. 85

Figure 5.8. Temperature variations with time for Test 3 (Table 3.4), using PCM container B. Interval (A), in red, marks the liquid sensible cooling regime; interval (B) in purple stands for latent cooling; and interval (C) in blue represents the solid sensible cooling regime. 86

Figure 5.9. Temperature variations with time for Test 4 (Table 3.4), using PCM container B and interrupted by removing the evaporator from the PCM. Period (A), in red, marks the liquid sensible cooling regime; and interval (B) in purple stands for latent cooling. The solid sensible cooling regime is not present, due to the extraction. 87

Figure 5.10. Pictures from the evaporator after removal from PCM container B ($D_o = 112''$), from Test 4 (Table 3.4): a) next to a steel ruler, for scale; b) close up near the top of the evaporator. 88

Figure 5.11. Temperature variations with time for Test 5 (Table 3.4). 89

Figure 5.12. Temperature variations with time for Test 6 (Table 3.4), interrupted by removing the evaporator from the PCM. 89

Figure 5.13. Picture from the evaporator after removal from 114'' PCM container, from Test 6 (Table 3.4), with a digital caliper measuring the solidified layer thickness at one of the points where it was intact. 90

Figure 5.14. Temperature variations with time for Test 7 (Table 3.4), with heat inputs of $q_{in} = 40 \text{ W}$ and $v^\infty = 4,45 \text{ m/s}$ 92

Figure 5.15. Temperature variations with time for Test 12 (Table 3.4), with heat inputs of $q_{in} = 80$ W and $v_{\infty} = 12,93$ m/s.....	92
Figure 5.16. Temperature variations with time for Test 13 (Table 3.4), with $q_{in} = 50$ W and $v_{\infty} = 4,45$ m/s.....	94
Figure 5.17. Temperature variations with time for Test 16 (Table 3.4), with $q_{in} = 80$ W and $v_{\infty} = 12,93$ m/s.	94
Figure 5.18. Temperature variations with time for Test 17 (Table 3.4), with $q_{in} = 50$ W and $v_{\infty} = 4,45$ m/s.....	95
Figure 5.19. Temperature variations with time for Test 20 (Table 3.4), with $q_{in} = 80$ W and $v_{\infty} = 12,93$ m/s.	95
Figure 5.20. Temperature variations with time for Test 21 (Table 3.4), with $q_{in} = 50$ W and $v_{\infty} = 4,45$ m/s.....	96
Figure 5.21. Temperature variations with time for Test 24 (Table 3.4), with $q_{in} = 80$ W and $v_{\infty} = 12,93$ m/s.	96
Figure 5.22. Nusselt number, Nud, x , versus total cooling time, Δt_c , for all tests from the main experiment (Table 3.4).....	97
Figure 5.23. Cooling time versus PCM mass comparison between baseline test 12 and main experiment tests 16 (container A), 20 (container B) and 24 (container C) (Table 3.4), all subjected to $v_{\infty} = 12.93$ m/s. Δt_s was measured for a temperature drop of $\Delta T_a = 10$ °C, while Δt_c was obtained for a temperature drop of $\Delta T_a = 20$ °C.	99
Figure 5.24. Cooling time versus PCM mass comparison between baseline test 7 and main experiment tests 13 (container A), 17 (container B) and 21 (container C) (Table 3.4), all subjected to $v_{\infty} = 4.45$ m/s. Δt_s was measured for a temperature drop of $\Delta T_a = 10$ °C, while Δt_c was obtained for a temperature drop of $\Delta T_a = 15$ °C.	99
Figure 5.25. Experimental evaporator thermal resistance versus heat transfer rate and analytical models for Re_{vap} with correlations from Kiyomura, Groll & Rosler, and Farsi.	102
Figure 5.26. Experimental condenser thermal resistance versus heat transfer rate and analytical models for R_{cond} with correlations from Kaminaga, Groll & Rosler, and modified Nusselt.	103
Figure 5.27. Comparison between experimental and theoretical values of $RCTPT$ with the two best combinations of Re_{vap} and R_{cond} from Table 5.3.....	104
Figure 5.28. Theoretical and experimental values of $RCTPT$ for Re_{vap} and R_{cond} from Table 5.3, $RCTPT, 3$ and $RCTPT, 5$	105

Figure 5.29. Experimental values of thermal resistance versus heat transfer rate. ..	106
Figure 5.30. Comparison between experimental and theoretical total resistance. ...	106
Figure 5.31. Theoretical and experimental temperatures at the different thermosyphon sections.	107
Figure 5.32. Dimensionless values of Rayleigh number and aspect ratio versus PCM diameter for the three PCM containers, and for all tests of the main experiment (tests 13 to 24 in Table 3.4).....	108
Figure 5.33. Comparison between the semi-empirical model and experimental data for effective conductivity, k_{eff} , versus Ra_{kl}	109
Figure 5.34. Comparison between experimental data and analytical model predictions for dimensionless temperature, θ , as a function of dimensionless time, Fo , for Test 13 (Table 3.4).....	112
Figure 5.35. Comparison between experimental data and analytical model predictions for dimensionless temperature, θ , as a function of dimensionless time, Fo , for Test 20 (Table 3.4).....	113
Figure 5.36. Comparison between experimental and analytical model predictions for the total dimensionless time, Fo , for tests 13 to 24 (Table 3.4).	114
Figure 5.37. Experimental evaporator and PCM resistances as a function of time for test 13 (Table 3.4), with PCM container (A).	116
Figure 5.38. Experimental evaporator and PCM resistances as a function of time for test 21 (Table 3.4), with PCM container (C).	116
Figure 5.39. Experimental ratio η compared to the critical value, $\eta_{cr} = 1,6$ for tests 13 to 16 (Table 3.4), with PCM container (A).	117
Figure 5.40. Experimental ratio η compared to the critical value, $\eta_{cr} = 1,6$ for tests 17 to 20 (Table 3.4), with PCM container (B).	118
Figure 5.41. Experimental ratio η compared to the critical value, $\eta_{cr} = 1,6$ for tests 21 to 24 (Table 3.4), with PCM container (C).	118
Figure 5.42. Dimensionless parameters $Focr$ versus Bis for the critical latent period, with experimental data from PCM containers (A), (B), and (C) and the proposed semi-empiric correlation.....	119
Figure 5.43. Comparison between experimental and analytical values of Foc for the critical latent period, and for the main experiment with PCM containers (A), (B), and (C)..	120

Figure 5.44. PCM latent heat effectiveness, ψ_{PCM} , versus Biot ratio Bid/Bis for the analytical model predictions and experimental data from PCM containers (A), (B), and (C).	122
Figure 5.45. Comparison between experimental and analytical values of PCM latent heat effectiveness, ψ_{PCM} , for the main experiment and with PCM containers (A), (B), and (C).	122
Figure B.1. Temperatures as a function of time for Test 8 (Table 3.4).....	148
Figure B.2. Temperatures as a function of time for Test 9 (Table 3.4).....	149
Figure B.3. Temperatures as a function of time for Test 10 (Table 3.4).....	149
Figure B.4. Temperatures as a function of time for Test 11 (Table 3.4).....	150
Figure B.5. Temperatures as a function of time for Test 14 (Table 3.4), with inputs of $q_{in} = 60$ W and $v^\infty = 6,83$ m/s.....	150
Figure B.6. Temperatures as a function of time for Test 18 (Table 3.4).....	151
Figure B.7. Temperatures as a function of time for Test 19 (Table 3.5).....	151
Figure B.8. Temperatures as a function of time for Test 15 (Table 3.4), with inputs of $q_{in} = 70$ W and $v^\infty = 9,94$ m/s.....	152
Figure B.9. Temperatures as a function of time for Test 22 (Table 3.4).....	153
Figure B.10. Temperatures as a function of time for Test 23 (Table 3.4).....	153
Figure B.11. Experimental evaporator and PCM resistances as a function of time for test 14 (Table 3.4), with PCM container (A).....	154
Figure B.12. Experimental evaporator and PCM resistances as a function of time for test 15 (Table 3.4), with PCM container (A).....	154
Figure B.13. Experimental evaporator and PCM resistances as a function of time for test 16 (Table 3.4), with PCM container (A).....	155
Figure B.14. Experimental evaporator and PCM resistances as a function of time for test 17 (Table 3.4), with PCM container (B).....	155
Figure B.15. Experimental evaporator and PCM resistances as a function of time for test 18 (Table 3.4), with PCM container (B).....	156
Figure B.16. Experimental evaporator and PCM resistances as a function of time for test 19 (Table 3.4), with PCM container (B).....	156
Figure B.17. Experimental evaporator and PCM resistances as a function of time for test 20 (Table 3.4), with PCM container (B).....	157
Figure B.18. Experimental evaporator and PCM resistances as a function of time for test 22 (Table 3.4), with PCM container (C).....	157

Figure B.19. Experimental evaporator and PCM resistances as a function of time for test 23 (Table 3.4), with PCM container (C).....	158
Figure B.20. Experimental evaporator and PCM resistances as a function of time for test 24 (Table 3.4), with PCM container (C).....	158

LIST OF TABLES

Table 2.1 – Maximum merit number for selected medium temperature working fluids.	21
Table 2.2 – Thermal characteristics of selected PCMs for a medium temperature range. Adapted from CUNHA; EAMES (2016).	22
Table 3.1– Dimensions of the thermosyphon, where do , di , le , la , lc and lt are, respectively, outer and inner diameter of the tube walls, evaporator length, adiabatic section length, condenser length, and total tube length.	34
Table 3.2 – Dimensions of the PCM containers.....	36
Table 3.3– Thermocouple positions on the thermosyphon, from the origin $x=0$ at the bottom of the evaporator.....	38
Table 3.4 – Tests performed with controlled power oscillations in the heat source. .	41
Table 3.5 – Tests performed to obtain a correlation for external heat transfer coefficient on the wind tunnel, h_{∞}	44
Table 3.6 – Coefficients used in Zukauskas’ correlation, Eq. (3.4).	45
Table 4.1 – Dimensionless variables for the 1D transient heat conduction analyses.	64
Table 5.1 – Total duration of the transient cooling regime, Δtc , for each PCM container used on the complete visualization tests (1, 3 and 5 on Table 3.4).	83
Table 5.2 – Average solid layer thickness, critical layer PCM mass and total PCM mass data for each interrupted test (2, 4 and 6 on Table 3.4).	85
Table 5.3 – Matrix of combinations among condenser and evaporator models.....	103
Table 5.4 – Variables and results of dimensionless BiL for the main experiment, tests numbered 13 to 24 (Table 3.4).	110

LIST OF ABBREVIATIONS

ASHRAE	American Society of Heating, Refrigerating and Air-Conditioning Engineers
B.C.	Boundary condition
C.V.	Control volume
EPE	Energy research company (empresa de pesquisa energética)
JCGM	Joint Committee for Guides in Metrology
LABTUCAL	Heat Pipe Laboratory of the Federal University of Santa Catarina (laboratório de tubos de calor)
PCM	Phase change material
TES	Thermal energy storage

LIST OF SYMBOLS

Latin alphabet:

A	[m ²]	Area
Bi	[-]	Biot number
B_1	[-]	Constant 1 of the PDE
B_2	[-]	Constant 2 of the PDE
B_3	[-]	Constant 3 of the PDE
C_0	[-]	Dimensionless constant for the critical Fourier semi-empirical correlation
C_1	[-]	Dimensionless constant for the effective conductivity semi-empirical correlation (1)
C_2	[-]	Dimensionless constant for the effective conductivity semi-empirical correlation (2)
C_3	[-]	Dimensionless constant for the effective conductivity semi-empirical correlation (3)
C_4	[-]	Dimensionless constant for the effective conductivity semi-empirical correlation (4)
c_p	[J/(kg.K)]	Specific heat
C_Z	[-]	Dimensionless Zukauskas coefficient
D_{cr}	[m]	Critical diameter
d_i	[m]	Inner diameter of the thermosyphon
D_i	[m]	Inner diameter of the PCM container
d_o	[m]	Outer diameter of the thermosyphon
D_o	[m]	Outer diameter of the PCM container
E	[-]	Energy
Fo	[-]	Fourier number
g	[m/s ²]	Acceleration of gravity on Earth
H	[m]	Height of liquid container, for Rayleigh analysis
h_{∞}	[W/(m ² .K)]	Convection heat transfer coefficient from condenser to ambient air
h_{eq}	[W/(m ² .K)]	Equivalent heat transfer coefficient from evaporator to ambient air
h_{sl}	[J/kg]	Latent heat of fusion/solidification
J_0	[-]	Bessel function of the first kind, of order zero
J_1	[-]	Bessel function of the first kind, of order one
k	[W/(m.K)]	Thermal conductivity
l	[m]	Length
L	[m]	Length of liquid container, for Rayleigh analysis
L_c	[m]	Characteristic length of the PCM container coupled with the thermosyphon
L_{cc}	[m]	Critical characteristic length
m	[kg]	Mass
Nu	[-]	Nusselt number
\dot{q}	[W]	Heat rate
r	[m]	Radius
R	[K/W]	Thermal resistance
R^2	[-]	Coefficient of determination
Ra	[-]	Rayleigh number

Ra_H	[-]	Rayleigh number based on H dimension
Ra_{Lc}	[-]	Rayleigh number based on characteristic length, L_c
Ra_{Lc}^*	[-]	Equivalent Rayleigh number
Re	[-]	Reynolds number
t	[s]	Time
Δt	[s]	Timespan
T	[°C]	Temperature
ΔT	[°C]	Temperature difference
v_∞	[m/s]	Air velocity within the wind tunnel
x	[m]	Position
Y_0	[-]	Bessel function of the second kind, of order zero
Y_1	[-]	Bessel function of the second kind, of order one

Greek alphabet:

α	[m ² /s]	Thermal diffusivity
β	[1/K]	Thermal expansion coefficient
δ_c	[m]	Critical solid layer thickness
ε	[-]	Error
η	[-]	Ratio of PCM to evaporator thermal resistances, R_{PCM}/R_e
θ	[-]	Dimensionless temperature
λ	[-]	Eigenvalue for the PDE
μ	[Pa.s]	Dynamic viscosity
ν	[m ² /s]	Cinematic viscosity
ξ	[-]	Dimensionless radius
ρ	[kg/m ³]	Specific mass
Σ	[-]	Sum
ϕ	[-]	Ratio of PCM heat capacity and latent heat to the system's overall temperature difference.
ψ	[-]	PCM effectiveness

Subscripts:

a	Adiabatic section of the thermosyphon
c	Condenser of the thermosyphon
cr	Critical latent heat cooling
d	Diameter of the thermosyphon
e	Evaporator of the thermosyphon
exp	Experimental
i	Index for the PDE solution sum
l	Liquid
m	Melting/solidification
max	Maximum
$mean$	Mean or average
min	Minimum
mid	Midsection
n	Total number of elements for the PDE solution sum
$peak$	Peak of the critical latent cooling

<i>s</i>	Solid
<i>sl</i>	Solidification
<i>SS</i>	Steady state
<i>v</i>	Vapor
∞	Ambient air

TABLE OF CONTENTS

1.	INTRODUCTION	15
1.1	PROBLEM STATEMENT	16
1.2	OBJECTIVES	16
1.2.1	SPECIFIC OBJECTIVES	17
1.3	STRUCTURE.....	17
2.	LITERATURE REVIEW	19
2.1	WORKING PRINCIPLES OF A CLOSED TWO-PHASE THERMOSYPHON	19
2.2	LATENT THERMAL ENERGY STORAGE	21
3.	EXPERIMENTAL STUDY	31
3.1	EXPERIMENTAL SETUP	31
3.1.1	thermosyphon AND PCM CONTAINERS	33
3.1.2	THERMOCOUPLE PLACEMENT.....	38
3.1.3	SELECTION OF A WIND TUNNEL AS HEAT SINK FOR THE thermosyphon CONDENSER	39
3.2	EXPERIMENTAL PROCEDURE	40
3.2.1	EXPERIMENT AND DATA REDUCTION METHOD TO OBTAIN NUSSELT NUMBERS IN THE WIND TUNNEL	42
3.2.2	VISUALIZATION EXPERIMENT	45
3.2.3	BASELINE EXPERIMENT	46
3.2.4	MAIN EXPERIMENT	47
4.	ANALYTICAL MODELS	48
4.1	MODELS FOR STEADY STATE OPERATION.....	48
4.1.1	THE thermosyphon THERMAL RESISTANCE	50
4.1.2	THE PCM CONTAINER THERMAL RESISTANCE	55
4.2	MODELS FOR TRANSIENT STATE: LIQUID SENSIBLE COOLING	60

4.2.1	LUMPED HEAT CAPACITANCE	62
4.2.2	1D TRANSIENT HEAT CONDUCTION	63
4.3	MODELS FOR TRANSIENT STATE: CRITICAL LATENT HEAT OF SOLIDIFICATION	68
4.3.1	CRITERION FOR THE CRITICAL SOLIDIFICATION REGIME.....	68
4.3.2	SEMI-EMPIRICAL CORRELATION FOR THE DURATION OF CRITICAL LATENT HEAT TRANSFER.....	70
4.3.3	LATENT HEAT EFFECTIVENESS.....	72
5.	RESULTS AND DISCUSSIONS.....	76
5.1	EXPERIMENTAL RESULTS	76
5.1.1	NUSSELT NUMBERS	76
5.1.2	VISUALIZATION EXPERIMENT	80
5.1.3	BASELINE EXPERIMENT	91
5.1.4	MAIN EXPERIMENT	92
5.2	ANALYTICAL MODELS RESULTS.....	101
5.2.1	MODELS FOR STEADY-STATE OPERATION.....	101
a)	<i>THERMOSYPHON MODELS</i>	<i>101</i>
b)	<i>PCM CONTAINER THERMAL RESISTANCE</i>	<i>108</i>
5.2.2	MODELS FOR TRANSIENT STATE: LIQUID SENSIBLE COOLING ..	109
5.2.3	MODELS FOR TRANSIENT STATE: CRITICAL LATENT HEAT OF SOLIDIFICATION	114
a)	<i>CRITERION FOR THE CRITICAL SOLIDIFICATION REGIME.....</i>	<i>114</i>
b)	<i>SEMI-EMPIRICAL CORRELATION FOR THE DURATION OF CRITICAL LATENT HEAT TRANSFER.....</i>	<i>118</i>
c)	<i>LATENT HEAT EFFECTIVENESS</i>	<i>120</i>
6.	CONCLUSIONS.....	124
6.1	SUGGESTIONS FOR FUTURE WORKS	125
	REFERENCES	127
	APPENDIX A.....	132

A.1 Measurement uncertainty	132
A.1.1 DIRECT MEASUREMENTS	133
<i>a) Length</i>	<i>134</i>
<i>b) Temperature</i>	<i>134</i>
<i>c) Air velocity in the wind tunnel</i>	<i>134</i>
<i>d) Electric current and tension</i>	<i>136</i>
A.1.2 INDIRECT MEASUREMENTS	138
<i>a) Electric power</i>	<i>138</i>
<i>b) Reynolds number</i>	<i>139</i>
<i>c) Experimental Nusselt number</i>	<i>141</i>
<i>d) Experimental thermal resistances</i>	<i>144</i>
REFERENCES FOR APPENDIX A	147
APPENDIX B	148
B.1 Baseline experiment	148
B.2 Main experiment	150
B.3 Critical latent period	154

1. INTRODUCTION

The need for energy storage is one of the main challenges for the implementation of renewable energies today. The natural resources that can be used for power generation are susceptible to seasonal and even daily variations, which are often not aligned with the energy demand. Brazil is affected by this issue, having one of the world's largest percentages in renewable sources due to the predominance of hydroelectric power plants, which correspond to 65% of the installed capacity for electricity generation (EPE, 2019). This natural resource suffers during sustained droughts, and the power generation needs to be supplemented by thermoelectric power plants, which burn fuel and emit large quantities of greenhouse gases. Therefore, increasing the contribution of other renewable energy sources and investing in energy storage solutions are necessary steps to reduce the reliance on thermoelectric plants while maintaining the country's energy supply security.

The current work studies a type of thermal energy storage system, one of the most researched storage solutions for solar power applications. Solar energy is amongst the most largely available natural resources in Brazil, with the country's Northeastern to the Midwestern regions showing potential for solar thermal power generation. However, one key obstacle for solar energy applications is the phenomenon of solar intermittency, which causes thermal oscillations that make power generation unreliable. In this context, thermal energy storage systems are added to the power plant, which charge by accumulating heat during periods of high solar incidence, and discharge by releasing heat to the thermal process as needed.

The system studied in this work stores energy in the form of latent heat, which promotes phase change. Because of this, the materials used for latent heat storage are called Phase Change Materials (PCMs) and typically making use of the solid – liquid transition. During high solar incidence, the initially solid PCM charges by melting, absorbing energy in the form of latent heat. Then, during discharge, it releases that heat and returns to its solid state. PCMs are capable of providing large energy densities to a thermal process, at approximately constant temperatures and small temperature gradients. However, the more commonly used PCMs have low thermal conductivities which make the extraction of heat from the storage more difficult. Another issue reported in the literature is that the solidification process occurs unevenly throughout the PCM volume, beginning on the surface of the heat exchanger and forming a solid layer with low thermal conductivity over the surface. This layer acts as a thermal barrier, impeding access to the energy stored in the remaining PCM volume.

Several solutions have been proposed to enhance heat transfer from latent thermal storage, either by altering the composition of the PCM itself or improving the performance of the heat exchanger connected to the thermal process, such as the addition of closed two-phase thermosyphons as heat exchangers connecting the energy storage and the thermal process, improving heat transfer due to their high thermal conductivity.

The current work was developed in the Heat Pipe Laboratory of the Federal University of Santa Catarina, LABTUCAL, which is specialized in heat pipes and two-phase thermosyphons. By making use of the laboratory's infrastructure and expertise, this study investigates a system composed of a thermosyphon coupled with a PCM storage container. The formation of a solid thermal barrier layer at the beginning of solidification is analyzed, as well as the efficiency of the PCM as a thermal storage device.

1.1 PROBLEM STATEMENT

Despite improvements to the overall heat transfer coefficient, it remains difficult to extract most of the latent heat stored in phase change materials, due to the nature of the solid – liquid phase change. During the heat discharge period, solidification does not occur simultaneously throughout the entire PCM volume, but rather starts on the surface of the heat exchanger with a solidified layer with low thermal conductivity, effectively insulating the surface from the remaining liquid material and impeding access to the stored energy. This results in a reduced heat transfer rate output to the thermal process.

In this context, this work proposes a study on the efficiency of latent thermal energy storage as a function of solid layer thickness and defines a critical layer thickness beyond which heat transfer becomes too ineffective to sustain the thermal process, so that the remaining latent heat in the PCM is virtually inaccessible. This value of critical layer can provide an important design parameter for storage tanks and heat exchangers, as it provides a limit ratio of useful volume of PCM per surface area of the heat exchanger, avoiding the waste of valuable resources such as storage room, material and stored energy.

1.2 OBJECTIVES

This work aims to develop a design parameter for latent heat storage units by studying both experimentally and analytically the process of solidification within a phase change

material (PCM) during the discharge phase of a thermal process. This design parameter comes in the form of an analytical model for a critical solidified layer on the heat transfer surface, that makes the heat transfer efficiency from the PCM to the thermal process reach a maximum, and beyond which the available energy in the remaining volume becomes virtually inaccessible.

1.2.1 SPECIFIC OBJECTIVES

In order to achieve the main objective described above, several specific objectives have been established as stepping stones:

1. To confirm the hypothesis that the peak heat transfer during phase change corresponds to the formation of a critical solidified layer;
2. To investigate the effect of the PCM volume on the solidification phenomenon, while maintaining a fixed heat transfer area;
3. To establish an analytical model for the PCM heat storage while operating under a sensible heat transfer regime;
4. To develop an analytical model for the critical solid layer that marks the peak efficiency of the latent heat transfer regime.

For these purposes, three containers were designed and manufactured for latent heat storage, with different sizes to study the impact of PCM volume on the heat transfer efficiency. The PCM containers were associated with a closed two-phase thermosyphon as a heat exchanger to extract the stored latent heat, and an experimental bench was also designed to conduct experiments on these devices.

1.3 STRUCTURE

In Chapter 2, the reader is given context in the form of a literature review for the devices and principles approached in this study. The first section introduces the working principles of closed two-phase thermosyphons. The next section discusses latent heat storage using phase change materials, PCMs, along with their properties, advantages over other forms of thermal storage, and expected challenges to their implementation.

Chapter 3 describes the experimental study conducted for this work, with the first section presenting the equipment, experimental set up and the devices that were designed and manufactured in the Heat Pipe Laboratory of the Federal University of Santa Catarina,

LABTUCAL. The next section details the experimental procedure, including the data reduction method used for establishing the Nusselt number relative to the external heat transfer coefficient from the thermosyphon condenser to the heat sink. Then, the preliminary tests made to visually assess the solidification phenomenon, the baseline tests performed to provide a basis for comparison to the main experiment and, lastly, the main experiment which studies the behavior of the proposed device during transient thermal oscillations, where the heat supply is interrupted and the stored energy in the PCM becomes the heat source for the thermal process.

Chapter 4 proposes and discusses analytical models for the transient cooling regime, beginning with the steady state operation as a foundation, choosing the appropriate models from the literature. Then, the following section discusses the model for sensible cooling. The last section analyzes the critical latent period, proposing a criterion to recognize it in the experimental results, then analytical models to predict its duration, and the corresponding effectiveness of the critical latent period, compared to the total energy stored as latent heat in the PCM.

Chapter 5 presents and discusses the results from both the experimental and analytical studies. The first section focuses on the experimental results, considering steady state operation as the start of the process and analyzing the transient cooling regime due to power oscillation. This is divided into a sensible cooling period, followed by a critical latent heat period and then a slower latent heat stage. Then, the next section discusses the analytical results, in comparison to the experimental data.

Finally, chapter 6 presents the main conclusions from this study, and suggests further studies and inquiries in this field.

2. LITERATURE REVIEW

In this chapter, a literature review is presented for closed two-phase thermosyphons and latent thermal energy storage using phase change materials (PCMs), pointing out the key concepts approached by this study. The main challenges of using PCMs are presented, along with some current solutions using closed two-phase thermosyphons.

2.1 WORKING PRINCIPLES OF A CLOSED TWO-PHASE THERMOSYPHON

As mentioned earlier, this work proposes the use of closed two-phase thermosyphons as heat exchangers connecting the thermal energy storage and the thermal process. Closed two-phase thermosyphons, which will from now on be referred to as simply thermosyphons, are highly efficient heat transfer devices that are basically composed of an evacuated tube charged with a working fluid that operates in a closed liquid – vapor phase change cycle. The fluid accumulates as a liquid pool in the bottom section of the device, called the evaporator, where it is heated and evaporates. The vapor then flows upwards into the condenser section, where it is cooled and returns to liquid state, flowing downwards and returning to the evaporator by gravity means. Therefore, thermosyphons are passive devices (MANTELLI, 2021), and their overall structure and operation is illustrated in Figure 2.1.

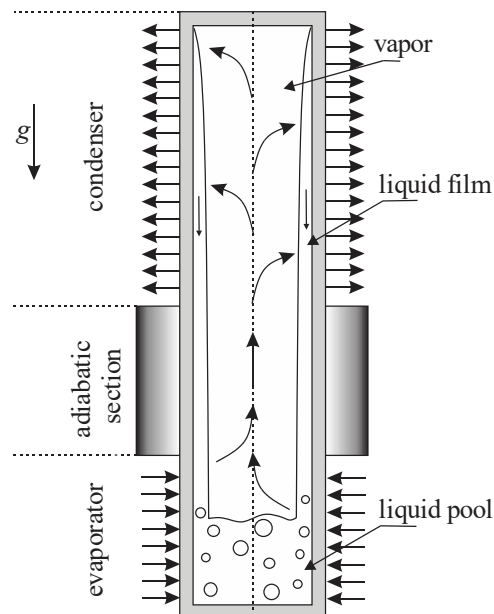


Figure 2.1. Schematics of the operating principle of a closed two-phase thermosyphon. Adapted from Mantelli (2021).

When designing a thermosyphon, the choice of an appropriate working fluid is essential. Each fluid has a range of operating temperatures, which corresponds to the maximum heat transfer capacity. This range is characterized by the merit number, M , defined by the thermophysical properties of the fluid according to:

$$M = \left(\frac{h_{lv} k_l^3 \rho_l^2}{\mu_l} \right)^{\frac{1}{4}} \quad (2.1)$$

where k_l , ρ_l and μ_l are its thermal conductivity, density and absolute viscosity, respectively, in liquid phase, and h_{lv} is its latent heat of vaporization. The working temperature range desired in this study is medium to low, for safety reasons. Table 2.1 shows the maximum merit number for some selected fluids operating at medium to low temperatures, with the highest overall merit number belonging to water at 180 °C. This information is complemented by Figure 2.2, which shows both the merit numbers (solid lines) and the saturation pressures (dashed lines), as functions of operating temperature, also for selected low and medium temperature working fluids, showing a smaller range of temperatures.

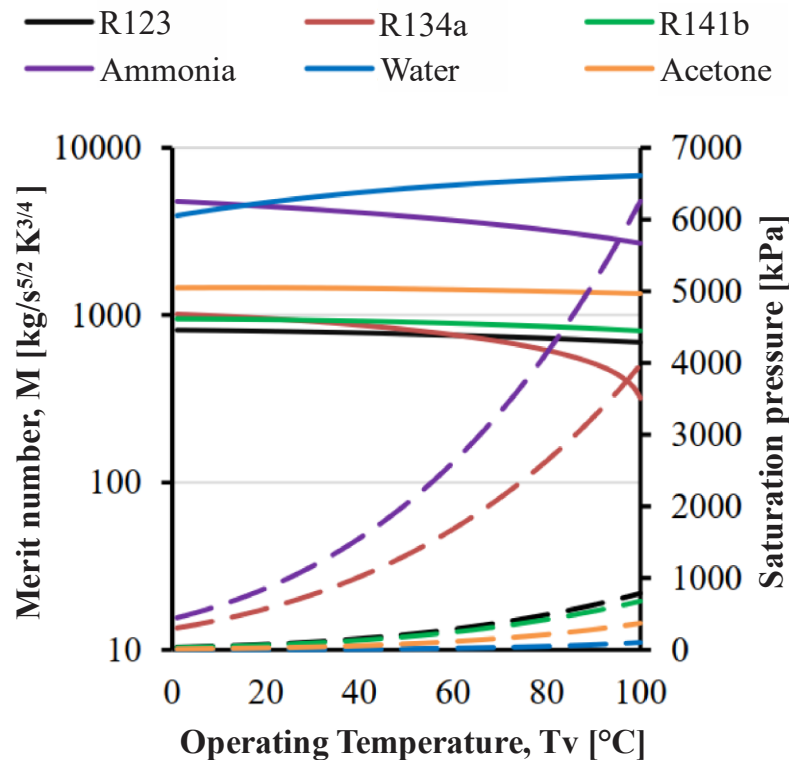


Figure 2.2. Merit number (solid lines) and saturation pressure (dashed lines) as functions of operating temperature for selected low and medium temperature working fluids (BELLANI, 2017).

Table 2.1 – Maximum merit number for selected medium temperature working fluids.

Fluid	Operating temperature, T_v [°C]	Maximum merit number, $M \left[\frac{kg}{K^4} S^{\frac{5}{2}} \right]$
Water	180	7542
Amonia	-40	4790
Methanol	145	1948
Acetone	0	1460
Toluene	50	1055
R141b*	-6,5	901

*Determined using the Eq. (2.1) and the Coolprop library for thermophysical properties.

Source: adapted from Reay *et al.* (2014).

In this study, two working fluids are necessary – the first is the thermosyphon working fluid, operating in a liquid-vapor phase change cycle, while the second is the PCM, which undergoes a liquid-solid phase change cycle during charge and discharge, with the main focus being on the liquid-solid change of the discharge period. The operating range of the first one, T_v , was selected according to the melting point of the second, T_m , so that the thermosyphon with $T_v > T_m$, ensuring that the PCM is completely melted at steady state operation. The selection of the PCM is discussed in the next section.

2.2 LATENT THERMAL ENERGY STORAGE

Thermal energy storage in the form of latent heat, using Phase Change Materials (PCMs) can be associated with solar thermal collectors and applied to medium and large scale systems such as centralized cooling, and district heating networks, as well as being potentially integrated into solar thermal energy generation systems based on the organic Rankine cycle (CUNHA; EAMES, 2016), which operates at medium temperature ranges (below 200 °C), to potentially stabilize the system against solar intermittency (HIGGO; ZHANG, 2015). PCMs can also be used to integrate multi-energy complementary systems due to their compact storage size and high energy density (HUANG *et al.*, 2022) by typically making use of the solid – liquid transition.

The most important requirements for the selection of a PCM are: high energy density of the storage material, heat transfer efficiency from the storage material to the heat transfer fluid (HTF), as well as chemical and mechanical stability of the storage material (GIL *et al.*, 2010). However, as mentioned in Chapter 1, the main challenge to the use of PCMs for thermal storage is their low conductivity, which makes for low heat transfer efficiency from the storage to the

desired thermal process. This becomes clear when observing Table 2.2, which shows the thermal properties of some commonly used PCMs for a medium temperature range. The listed thermal conductivities range from 0,13 to 0,73 (W/m.K) (CUNHA; EAMES, 2016), which are considered low.

Table 2.2 – Thermal characteristics of selected PCMs for a medium temperature range. Adapted from CUNHA; EAMES (2016).

Compound		T_m [°C]	ρ [kg/m ³]	h_{sl} [kJ/kg]	k_l [W/m K]	k_s [W/m K]
Organic:	Naphthalene	80	1145	148	0,13	0,34
	Paraffin wax	0–90	880–950	150–250	-	0,20
	Acetamide	82	1160	260	0,25	0,40
	Erythritol	117	1450	340	0,33	0,73
Salt hydrates:	Barium hydroxide octahydrate	78	2180	280	0,66	0,20
	Magnesium nitrate hexahydrate	89	1640	140	0,50	0,40
	Oxalic acid dihydrate	105	1653	264	0,70	0,73

Among the solutions proposed in the literature for this problem are the use of the PCM within a composite matrix, by embedding highly conductive materials, such as graphite particles (CHOI *et al.*, 2014), microencapsulation of the PCM (XIANG *et al.*, 2019), and embedding fins into the storage tank (AL-MUDHAFAR *et al.*, 2021), (GIL *et al.*, 2018). Moreover, several works propose the use of a thermosyphon to connect the PCM storage unit to the thermal process, since they are highly efficient thermal conductors. In fact, the application of heat pipes and thermosyphons embedded into PCM storage units is especially common in the field of cooling and temperature maintenance of electronics (BEHI *et al.*, 2021), (KANNAN; KAMACHI, 2021), (MADHAV *et al.*, 2021), (LIU *et al.*, 2006), which operate in temperate ranges typically lower than that of solar thermal energy.

Robak *et al.* (2011) performed an experimental analysis on the effect of embedding thermosyphons into a PCM storage unit versus a simple storage unit and one embedded only with fins. The authors used distilled water as the heat transfer fluid in the thermosyphon, and n-octadecane paraffin wax was used as the PCM, with a melting point of $T_m = 27,5$ °C. The

study observed a higher heat transfer rate from the storage unit to the working fluid in the case of embedded closed thermosyphons, resulting in faster charge and discharge cycles in the PCM. A similar system was studied by Nithyanandam and Pitchumani (2014), in this case for application in high temperature solar collectors, with PCM operating temperatures ranging from 300 to 600 °C. The heat transfer fluid considered was solar salt, composed of 60 % sodium nitrate and 40 % potassium nitrate, while the PCM was an unspecified molten salt, using thermophysical properties within the typical range reported in the literature. The authors used numerical simulations and developed a methodology to optimize the geometrical placement of the thermosyphons in the PCM container, with regards to storage costs and the efficiency standards defined by the SunShot Initiative of the U.S. Department of Energy. They simulated specific arrays of thermosyphons and their charge and discharge times, and concluded that there is a trade-off between closer spacing yielding higher storage cost and a larger spacing yielding limited heat transfer rates from the PCM to the working fluid.

Diao *et al.* (2021) propose the use of PCMs in a cascade configuration for thermal storage in a solar air-heating system in order to mitigate the solar intermittency and overcome time gaps between supply and demand of solar heat. These authors built an experimental system, seen in Figure 2.3, where during the charging process, a solar collector heats air to a high temperature, which then flows through the first latent heat storage unit, LHSU I, melting the paraffin wax PCM (with melting temperature range of $47 < T_m < 52$ °C), and then continues at a lower temperature to the second latent storage unit, LSHU II, where it melts the lauric acid within, which has a lower melting temperature range ($41 < T_m < 43$ °C). This cascade configuration makes use of the PCMs' different melting temperatures, since the hot air that leaves the first heat storage unit at a temperature lower than paraffin's melting point is still useful for melting lauric acid at the second heat storage unit. The charge and discharge cycles are shown in the schematics of Figure 2.3. In this article, the authors also point out the need for heat transfer enhancement from the thermal storage to the process and, in order to achieve this, they proposed the use of thermosyphons embedded into the storage units, as seen in Figure 2.4. Fins are also added to the extremities of the thermosyphons to improve heat transfer with the air ducts. These authors concluded that the charging process efficiency increased with air flow rate and temperature difference between hot air and PCM. However, during the discharge process, higher air flow rates caused the energy efficiency to decrease, especially for higher temperature differences between cool air and PCM. This negative result, despite the

enhancement of heat transfer rates added by the embedded thermosyphons, suggests that another mechanism is hindering the efficiency of the discharge process.

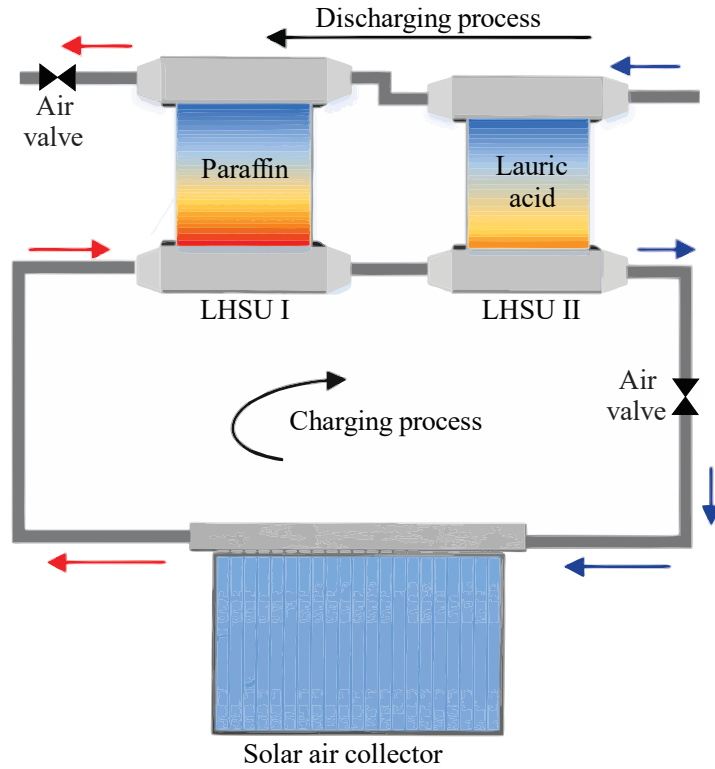


Figure 2.3. Simplified schematic of the experimental solar air heating system, using PCM storage units in a cascade configuration. Adapted from Diao *et al.*, 2021.

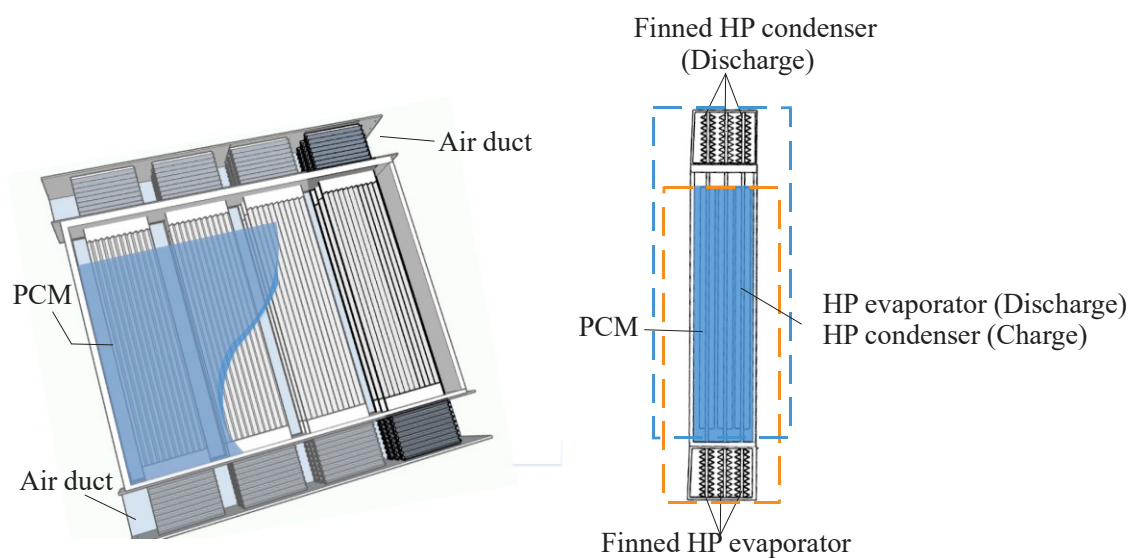
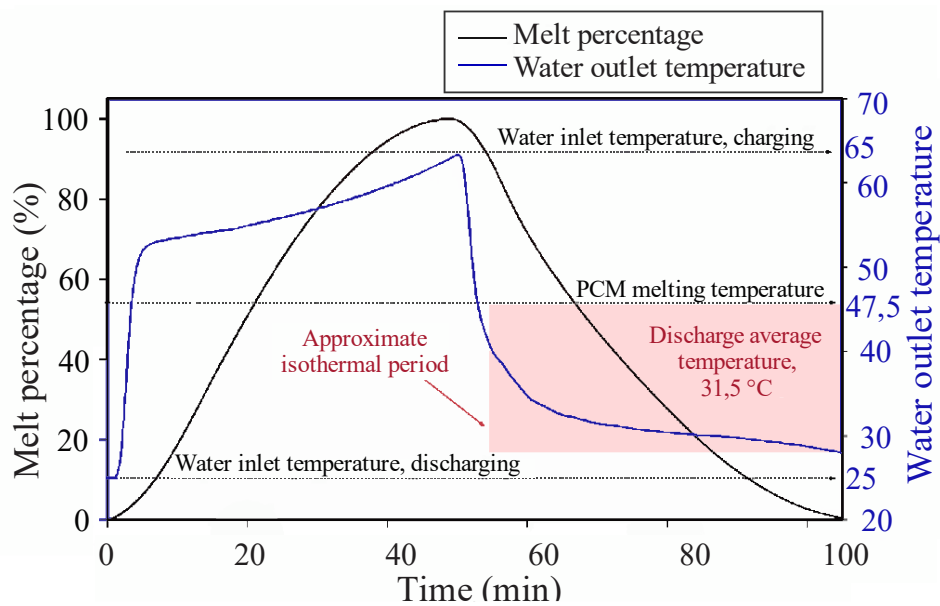


Figure 2.4. Structure of the LHSU detailing the different operating sections of the heat pipe depending on the phase of the charge-discharge cycle. Adapted from Diao *et al.*, 2021.

Luu *et al.* (2020) suggested a particular solidification phenomenon as responsible for low thermal efficiency in latent heat extraction. These authors used CFD simulations to develop a computational design method for increasing this efficiency in the case of a shell and tube heat exchanger associated with latent thermal storage. The working fluid considered was water, and the PCM was RT-50, commercially available from Rubitherm®, with $T_m = 47,5$ °C. Their approach is based on an exergy analysis pointing out that, while most of the current PCM research focuses on improving of heat transfer rates, the crux of the matter in terms of PCM energy efficiency is the temperature of the stored energy available to the working fluid, since the point of using latent heat storage is to retrieve thermal energy on demand and at the desired temperature range, surrounding the selected material's melting point. However, the accessible operating temperature during discharge typically drops considerably below the melting temperature (T_m), while the charging process requires heat to be provided at a higher temperature in order to melt the PCM, causing a large temperature difference in the working fluid between charge and discharge phases. This effect is seen in Figure 2.5 (a), which shows the simulation result for a complete charge/discharge cycle of a vertical shell-tube heat exchanger, where the shell is filled with PCM and water flows in the inner tube, from top to bottom. The dashed line shows the PCM melting temperature, while the solid black line represents the PCM melt percentage over time, marking the charge period as the initial time required for the melt percentage to go from zero (PCM is completely solid) to 100 % (PCM is completely liquid), and the discharge period as the remaining time, beginning at 100 % melted PCM and ending when the percentage returns to zero. The solid blue line shows the water temperature throughout the entire cycle, with an approximate average temperature during charging of 80 °C, which drops to 31,5 °C during discharge. In terms of an exergy efficiency analysis, the quality of thermal energy is associated to the temperature at which it is available, meaning that this temperature difference constitutes a loss in energy quality, and therefore exergy inefficiency.

Luu *et al.* (2020) then suggest that the cause for this problem is that, at the beginning of discharge, the PCM in the immediate vicinity of the heat transfer surface solidifies first, creating a thermal barrier layer, due to the solid PCM's low thermal conductivity, which effectively increases the thermal resistance from the liquid pool to the working fluid, requiring a larger temperature gradient and therefore lowering the fluid's operating temperature. Therefore, once this solid layer is formed, the remaining stored energy is virtually inaccessible to the thermal process, at least at the desired temperature range. This observation was confirmed by numerical

simulations of the solidification phenomena, as seen in Figure 2.5 (b), which shows the formation of a solid layer around the heat exchanger and associates it with the regimes in Figure 2.5 (a). The authors then developed an approach to mitigate the phenomenon by altering the geometry of the solid thermal barrier, increasing the time required for it to cover the entire heat transfer surface. This approach is demonstrated in Figure 2.6, which shows the simulation results for two distinct thermal barrier layer topologies, and the effect they have on the water outlet temperature during PCM solidification. The regime on the left is the most undesirable case, where the TBL quickly forms over the entire heat transfer surface and propagates radially, effectively hindering heat transfer from the liquid pool, in red, to the heat transfer fluid, in white. The regime on the right is a result of optimized design parameters and constitutes the most desirable outcome, where the TBL forms initially over only a fraction of the heat transfer surface and propagates axially, therefore leaving a portion of the liquid PCM pool in contact with the surface during most of the discharge regime.



(a)

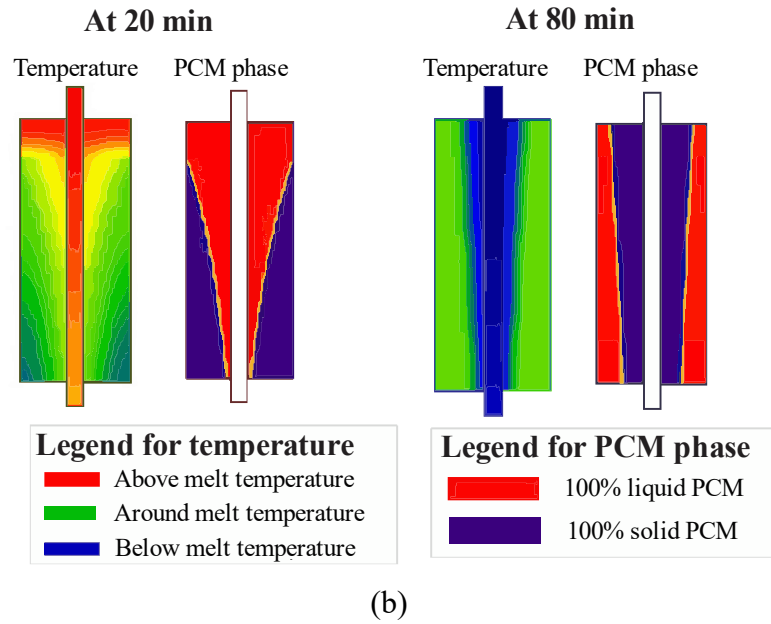


Figure 2.5. Simulation results for a complete charge/discharge cycle of a PCM in a shell-tube heat exchanger in vertical orientation. The water flows in the inner pipe from top to bottom. Figure (a): recorded melt percentage and water temperature; (b): a snapshot of PCM state (2D, cut through the middle) at 20 and 80 min, respectively. Adapted from Luu *et al.* (2020).

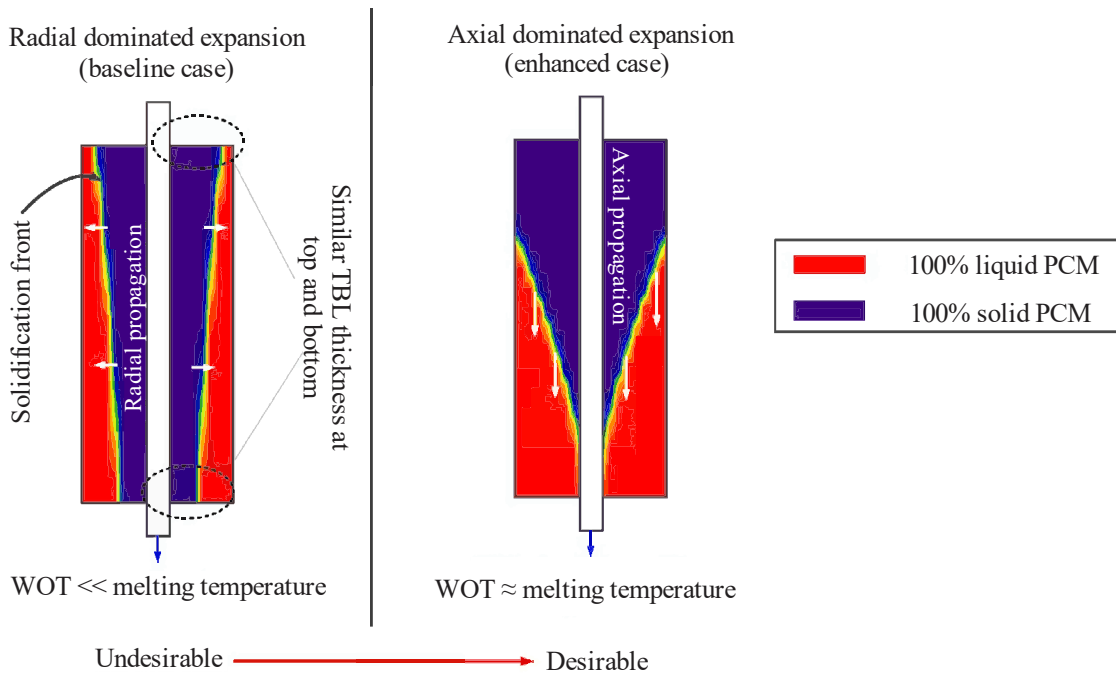


Figure 2.6. Two distinct thermal barrier layer (TBL) topologies, and their effect on the water outlet temperature (WOT) during PCM solidification. On the left is the most undesirable case, and on the right is the desirable outcome, using optimized design parameters. Adapted from Luu *et al.* (2020).

Figure 2.7 compares the numerical results of two optimized designs versus the base case represented by the left-hand side of Figure 2.6. The average temperature of the working fluid during discharge is shown as T_{DAT} , and the design parameter used by the authors was the Graetz

dimensionless number, Gz . The working fluid in all cases was water, and the PCM was RT-50, commercially available from Rubitherm® supplier, whose melting point is $T_m = 47,5 \text{ }^\circ\text{C}$. Both design case 1 and design case 2 outperform the base case, but each uses a different constraint. Design 1 assumes the need for a reduced number of water pipes to reduce the cost, and therefore suggests increasing the thermal conductivity of the PCM by 10 times. In contrast, design 2 assumes the need for a reduced water pipe length, as is the case for portable PCM storage units for carrying in cars, and suggests increasing the number of water pipes to up to 20, as well as increasing the PCM thermal conductivity. The results show that both optimized designs surpassed the desired target, showing a significant increase of the T_{DAT} .

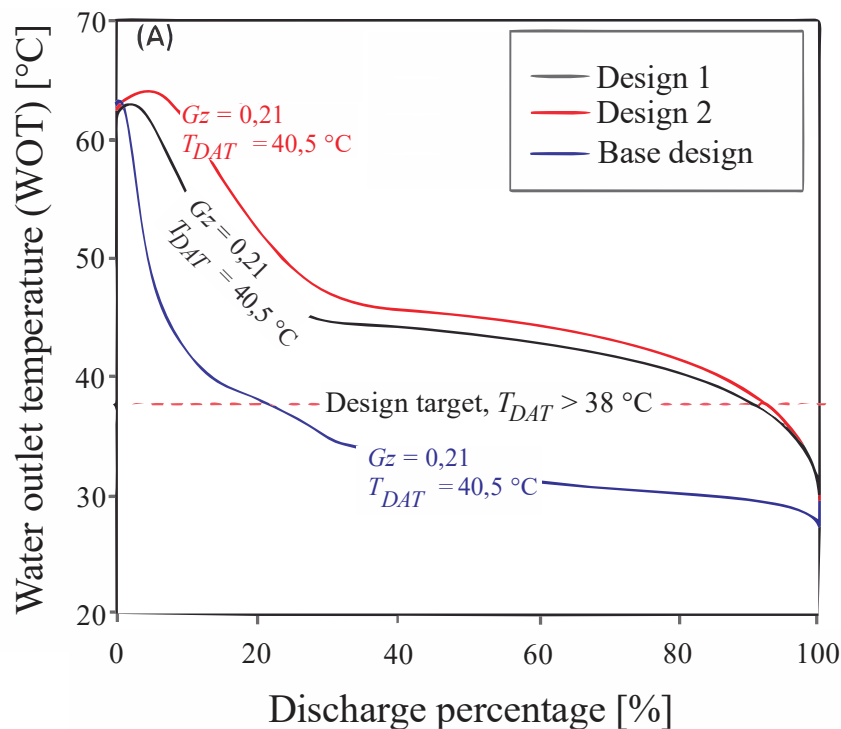


Figure 2.7. Water outlet temperature during discharge, for the base case (blue solid line), and for improved PCM tube designs 1 (black solid line) and 2 (red solid line). Adapted from Luu *et al.* (2020).

Pizzolato *et al.* (2017) also used numerical simulations to study the topology of solidification in a shell and tube configuration and remarked on the challenge posed by the uneven advance of the solidification front, leading to long discharge periods where the heat transfer surface is surrounded by solid PCM and the remaining phase change releases heat to the working fluid at a low rate. The authors proposed the use of highly conductive fins as a solution for this problem, and developed a fin design approach based on topology optimization and multi-phase computational fluid dynamics. No initial assumption was made on the fin layout and geometry and, instead, they were allowed to freely evolve according to the heat

transfer equations. The resulting optimized design is seen in Figure 2.8, along with a progression of the solidification front over time, showing that the PCM immediately surrounding the base of the fins solidified quickly, then the phase change progressed along the fins until it reached the outer wall of the PCM shell. This information is complemented by the average heat transfer rates due to convection and conduction over the total time for full solidification, $t_{f,s}^*$, as seen in Figure 2.9, which shows that the highest heat transfer rates were obtained near the outer tips of the fins, where the PCM retained a liquid fraction for longer than any other parts of the heat transfer surface. These results reinforce the point made by LUU *et al.* (2020), since they indicate that optimal fin design is not simply aimed at increasing the surface area for heat transfer, but rather at extending the surface area that is in contact with liquid PCM during most of the phase change, therefore avoiding the insulating effects of the solid thermal boundary layer described in the study of LUU *et al.* (2020).

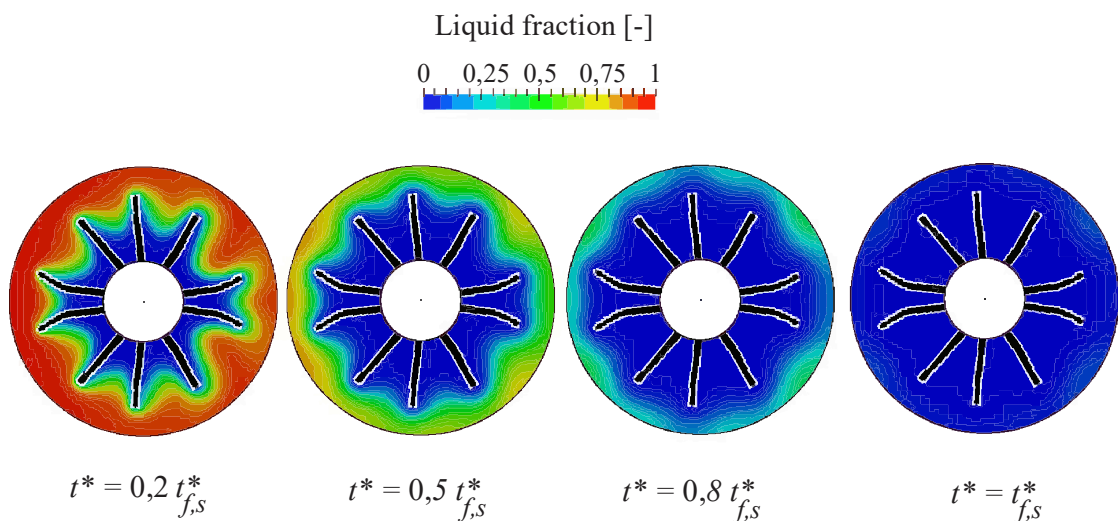


Figure 2.8. Liquid fractions at selected time instants during solidification, where $t_{f,s}^*$ is the time required for full solidification in the optimized design. Adapted from Pizzolato *et al.* (2017).

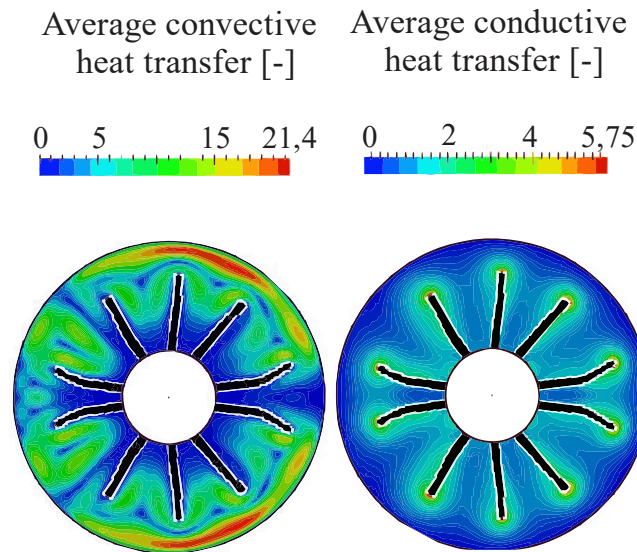


Figure 2.9. Average conductive and convective heat transfer rates during solidification. Adapted from Pizzolato *et al.* (2017).

As already presented here, one of the main objectives of this study is to investigate the beginning of PCM solidification, specifically the formation of a solidified thermal barrier layer around the heat transfer surface, as reported in the literature. The current work also aims to obtain analytical models for this phenomenon, which can provide a significant design parameter for heat exchangers in latent heat storage units, since the barrier layer constitutes an operating limit for maximum discharge efficiency. Therefore, with a better understanding of the initial stages of solidification, the heat transfer surface can be shaped so as to maximize the area over which the layer is formed while minimizing the excess volume of the PCM pool, where the latent heat storage is virtually inaccessible to the desired thermal process. Ultimately, this would lead to an optimization of the volume of latent heat storage units.

This study chose to work at medium to low temperatures, for safety reasons, and the chosen PCM was naphthalene, since it has attractive thermal characteristics among low temperature PCMs, such as high storage capacity, small volume changes during phase change processes, and stability (YANG *et al.*, 2015). Naphthalene was also selected because of its melting point, making a good combination with a closed two-phase thermosyphon. The PCM's melting point needed to be higher than the working fluid's boiling point, that is, $T_m(PCM) > T_{lv}(HTF)$, in order to act as a heat source for the thermosyphon during discharge. The melting point of naphthalene is $T_m = 80,3 \text{ }^\circ\text{C}$ (NSIT, 2021), higher than the boiling point of several refrigerant fluids, making them easy to work with.

3. EXPERIMENTAL STUDY

The experimental study conducted in this work investigated the formation of a critical thermal barrier layer during the solidification of a PCM. In order to assess this phenomenon, a device was constructed which consisted of a PCM container associated with a closed two-phase thermosyphon. Then, an experimental bench was assembled and a series of experimental procedures were devised to assess the thermal behavior of this device, which was measured as a function of controlled parameters such as temperature and heat transfer rate. The first of these procedures was a visualization experiment, to confirm the existence of a critical solidified layer of PCM. Then, a baseline experiment was conducted without PCM, to serve as a basis of comparison for the thermosyphon's thermal behavior. Finally, the main experiment of this study was performed to assess the effect of PCM volume and external heat transfer coefficient on the solidification phenomenon. The experimental setup and procedure are detailed in the following subsections.

3.1 EXPERIMENTAL SETUP

This work's experiments were designed and conducted in the Heat Pipe Laboratory of the Federal University of Santa Catarina, LABTUCAL. The experimental bench was composed of a (1) ultra-high temperature heating tape (Omega STH series) connected to a (2) power supply (MCE 1310) capable of providing up to 3000 W, a (3) data acquisition system (CR1000 Datalogger, Campbell Scientific), a (4) computer, (5) twenty type K thermocouples (Omega), a (6) wind tunnel controlled via a (7) frequency inverter, a (8) closed two-phase thermosyphon, a (9) Swagelok SS series valve, a (10) PCM container, and (11) layered glass wool for thermal insulation. Figure 3.1 shows a diagram of the experimental bench, while pictures of the actual setup can be seen in Figure 3.2 and Figure 3.3. The following sections present details of the design and selection of the wind tunnel, as well as the devices tested, namely the thermosyphon and the PCM containers.

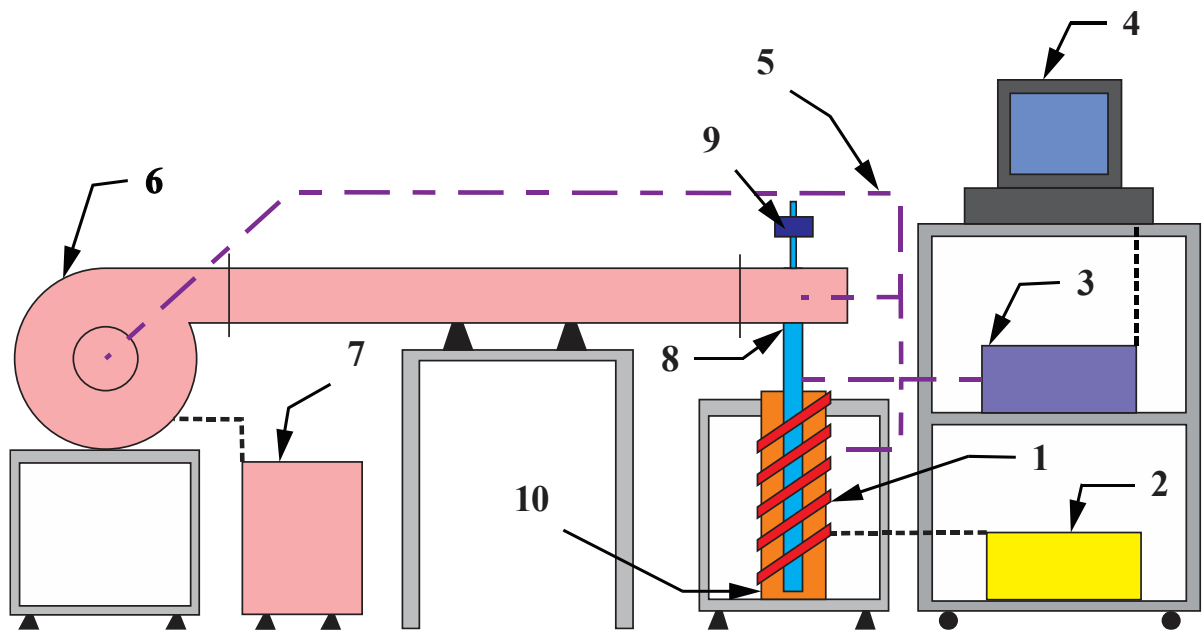


Figure 3.1. Diagram of the experimental setup: (1) ultra-high temperature heating tape Omega STH series;(2) power supply MCE 1310; (3) data acquisition system CR1000 Datalogger, Campbell Scientific; (4) computer; (5) twenty type K thermocouples Omega; (6) wind tunnel; (7) frequency inverter; (8) closed two-phase thermosyphon ; (9) Swagelok SS series valve; (10) PCM container.



Figure 3.2. Picture of the full experimental setup showing components as described in Figure 3.1.

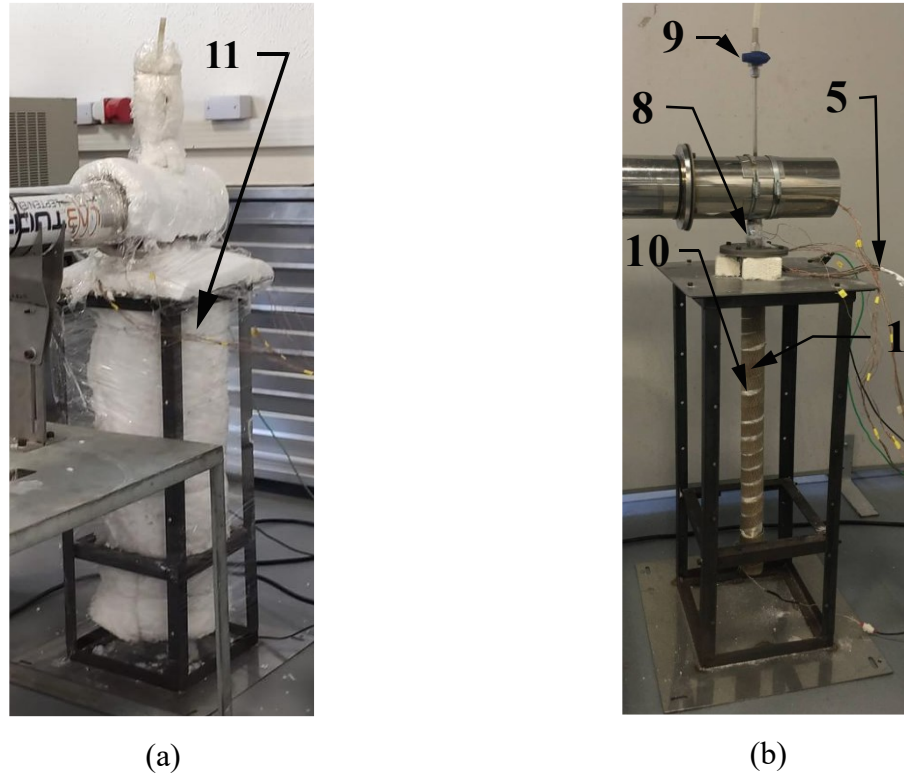


Figure 3.3. Test section: a) covered with insulating glass wool; b) bare.

3.1.1 THERMOSYPHON AND PCM CONTAINERS

The fluids chosen for this study were naphthalene, as PCM, and refrigerant R141-b as the working fluid of the thermosyphon. Both were selected due to their medium to low operating temperatures, as explained in Chapter 2, with both fluids working together. The choice for refrigerant R141-b for the thermosyphon was due to its well established thermophysical properties and good stability, its easy availability in the laboratory, as well as its low boiling point at atmospheric pressure, $T_{lv} = 32 \text{ }^\circ\text{C}$. The low boiling point allows the working fluid to operate with a positive pressure in the experiments, that is, saturation pressure above atmospheric pressure, $p_{sat} \geq p_{atm}$. This condition avoids the formation of a cold tip on the condenser, a phenomenon which lowers the efficiency of the thermosyphon. The cold tip is formed when there are non-condensable gases in the closed thermosyphon, and the vapor of the working fluid cannot reach the tip of the condenser, which is already occupied by lower temperature gases. Since the PCM must work alongside the thermosyphon's working fluid, it requires a melting point, T_m , higher than the boiling point of the chosen refrigerant, that is, $T_m(PCM) > T_{lv}(R141b)$, in order to act as a heat source for the thermosyphon during discharge. In this context, naphthalene was chosen due to its melting point of $T_m = 80,3 \text{ }^\circ\text{C}$

(NSIT, 2021), which is higher than the boiling point of several refrigerant fluids, making it easy to work with, as well as having the following desirable characteristics for a low temperature PCM: high storage capacity, small volume changes during phase change processes, and stability (YANG *et al.*, 2015).

The closed two-phase thermosyphon was made of a 1” stainless steel tube, and the dimensions can be seen in Table 3.1. The wind tunnel (6), shown in Figure 3.2, was used to remove heat from the thermosyphon’s condenser. Since this tunnel’s cross section had an inner diameter of 97 mm, the design of the condenser followed this existing dimension, with a condenser length $l_c = 97$ mm. A short adiabatic section of length $l_a = 43$ mm was included to allow for reliable measurements of vapor temperature. The evaporator length was selected as $l_e = 600$ mm, in order to have a large surface area for the formation of a solidified PCM layer, therefore increasing the duration of the critical solidification regime that is the focus of this study. Lastly, a flange was added to the tube, immediately above the evaporator, to be connected to a matching flange on the PCM container. The flange was designed and manufactured to fit the tube tightly, so as to remain in place without being welded, and had an outer diameter $D_f = 120$ mm and a thickness of 6 mm, for the flange attached to the thermosyphon, and of 3 mm for the flanges attached to the PCM containers.

Table 3.1– Dimensions of the thermosyphon, where d_o , d_i , l_e , l_a , l_c and l_t are, respectively, outer and inner diameter of the tube walls, evaporator length, adiabatic section length, condenser length, and total tube length.

d_o [mm]	d_i [mm]	l_e [mm]	l_a [mm]	l_c [mm]	l_t [mm]
25,4	21,4	600	43	97	750

The manufacturing of the thermosyphon was composed of the following seven steps:

- 1) Cutting the selected tube and end caps: a 1” stainless steel tube was selected and cut using a band saw, to the total length shown in Table 3.1. Two circular end caps were cut from a 3 mm stainless steel sheet using a water jet cutting machine. Both caps matched the tube, with the top cap having a circular hole of 1/4” diameter to fit the diameter of a stainless-steel umbilical tube, which was also cut using a band saw.
- 2) Cleaning the tube: the inside and the outside of the tube were washed with water and neutral detergent, then rinsed and air dried .

- 3) Welding end caps and attaching valve: the umbilical tube was welded onto the top and cap, which was then welded onto one extremity the tube. The bottom end cap was welded onto the tube's other extremity. Then, a Swagelok valve was connected to the umbilical tube, to ensure a reliable vacuum when the device was closed, while still allowing it to be opened whenever necessary.
- 4) Testing the device for leaks: the welded joints and the joints along the valve were tested using a helium leak detector (Pfeiffer Vacuum ASM 340), seen in Fig. 3.4
- 5) Evacuating the thermosyphon: the device was then connected to a liquid ring vacuum pump, seen in Fig. 3.5, to remove any residual water or vapor, as well as excess air. This pump can achieve a vacuum on the order of 10^{-4} Pa, which is enough to charge the thermosyphon with working fluid.
- 6) Charging with refrigerant R141b: a volume of $V_f = 159$ ml of the working fluid was measured and inserted into the thermosyphon, corresponding to a fill ratio $F = 60\%$, or 60% of the evaporator's internal volume. A picture taken during the charging procedure can be seen in Fig. 3.6.
- 7) Purging to ensure higher vacuum: to ensure the removal of air and other non-condensable gases from the device, the evaporator was heated until the temperature at the adiabatic section reached 60 °C, higher than the saturation temperature of R141b at atmospheric pressure, therefore ensuring the vapor pressure within the thermosyphon was higher than the outside pressure, since at 60 °C, p_{sat} of naphthalene was of 246 kPa. Then, the Swagelok valve was briefly opened and closed to remove the eventual pressurized non condensable gases. This procedure creates a higher quality vacuum in the thermosyphon than can be achieved using only the vacuum pump. In order to ensure that the fill ratio was maintained after purging, the outlet of the Swagelok valve was connected to a small graduated cylinder via a silicone tube, which was immersed in water for cooling. After the purge, the volume of R141b expelled to the container was measured and corresponded to less than 1 % of the volume V_f . Therefore, the filling ratio was considered to be maintained as $F = (60 \pm 1) \%$.



Figure 3.4. Helium leak detector, Pfeiffer Vacuum ASM 340.



Figure 3.5. Closed two-phase thermosyphon being evacuated by a liquid ring vacuum pump.

The PCM containers followed the set dimensions of the thermosyphon, matching the length of the evaporator, so that $l_{PCM} = l_e = 600$ mm. In total, three containers were designed and manufactured, as seen in Table 3.2, with varying diameters. All containers were completely filled with naphthalene in order to study the effects of PCM volume on the solidification phenomenon. The surface area in which heat transfer occurred was constant for all containers and tests, as it corresponded to the total external area of the evaporator. A flange was soldered onto the upper extremity of each container, matching the outer diameter of the flange on the thermosyphon.

Table 3.2 – Dimensions of the PCM containers.

	Container A	Container B	Container C
Outer diameter, D_o [mm]	50,80	38,10	31,75
Inner diameter, D_i [mm]	46,80	34,40	29,35
Container length, l_{PCM} [mm]	600	600	600
PCM volume, V_{PCM} [ml]	758	244	100
PCM mass, m_{PCM} [kg]	0,711	0,238	0,098

The manufacturing procedure for the PCM containers was simpler than that of the thermosyphon, since they did not require a vacuum in order to operate. Therefore, the steps were as follows:

- 1) Cutting the selected tubes and end caps: three stainless steel tubes were selected, with nominal diameters of 2" (container A), 1 1/2" (container B), and 1 1/4" (container C), as seen in Table 3.2. One circular end cap with matching diameter was cut for each one, from a 3 mm stainless steel sheet, using a water jet cutting machine. Flanges were also cut for the top opening of each container, with inner diameters matching the respective containers, and outer diameters $D_f = 120$ mm to match the flange on the thermosyphon.
- 2) Cleaning the inside of the tube: the inside and outside of the components were washed with water and neutral detergent, then rinsed and air dried.
- 3) Welding end caps and flanges: the end caps were welded onto the bottom extremity of each tube, while the flanges were welded around the top extremities.
- 4) Charging with naphthalene: the chosen PCM, naphthalene, was melted and measured in beakers before being introduced to each container in liquid form. Each container was completely filled, with the volumes described in Table 3.2. A picture of the melting and measuring of naphthalene can be seen in Figure 3.7.

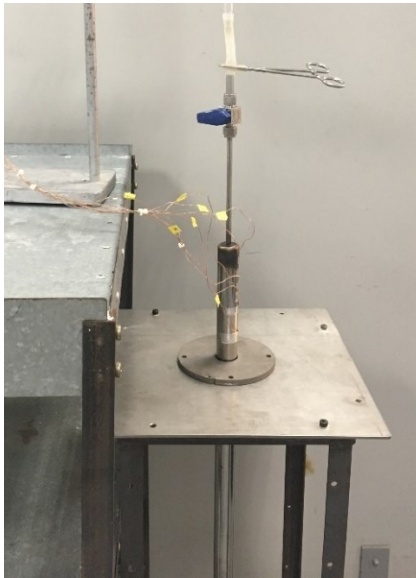


Figure 3.6. Charging of the thermosyphon with refrigerant R141b.



Figure 3.7. Melting and measuring of naphthalene.

3.1.2 THERMOCOUPLE PLACEMENT

A total of twenty K-type thermocouples were placed on the experimental setup, where nineteen were put on the closed two-phase thermosyphon and the PCM container, and one was put at the air inlet of the wind tunnel. The placement of the thermocouples along the device can be seen in Table 3.3, as well as the diagram of Figure 3.8, with the most thermocouples – twelve, in total – being located along the evaporator and the PCM container walls, since the object of this study is to study the heat transfer phenomena between them.

Table 3.3– Thermocouple positions on the thermosyphon, from the origin $x=0$ at the bottom of the evaporator.

Section:		Evaporator/ PCM Container						Adiabatic Section		Condenser				
Thermo- couples	PCM	1	2	3	4	5	6	-	-	-	-	-	-	
	Thermo- syphon	7	8	9	10	11	12	13	14	15	16	17	18	19
Position [mm]		50	150	250	350	450	550	635		669	685	701	717	733

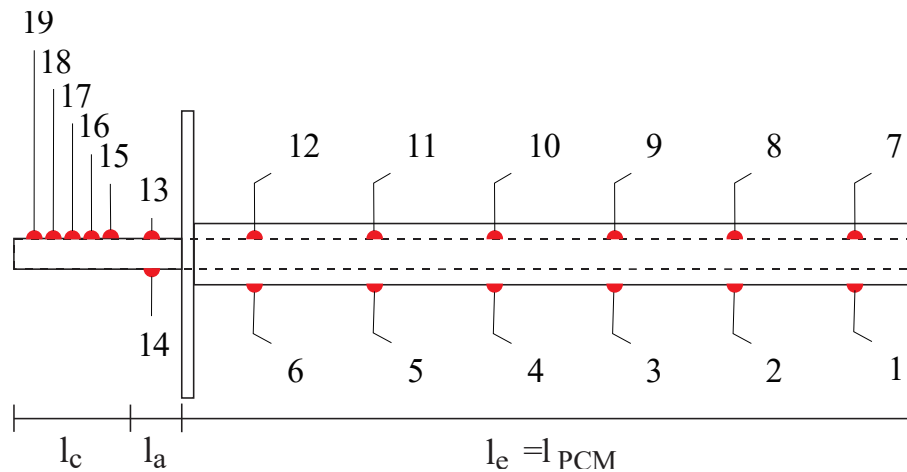


Figure 3.8. Diagram of the thermocouple placement on the thermosyphon and PCM container, according to Table 3.3.

3.1.3 SELECTION OF A WIND TUNNEL AS HEAT SINK FOR THE THERMOSYPHON CONDENSER

The knowledge of the heat transfer rate through the thermosyphon is an essential parameter for this study, since it is used to evaluate the PCM's energy delivery capacity during periods of power oscillation. For steady state operation, this parameter is easily obtained since the heat transfer rate throughout the system is equal to that supplied to the evaporator, \dot{q}_{in} , which is also equal to the electric power supplied to the heating tape, P_{el} , assuming that the system is well insulated. However, in order to study the PCM's energy discharge, the power supply must be temporarily cut off, causing the system to enter a transient regime of operation, where the heat rate input \dot{q}_{in} is unknown and provided by the PCM's discharging capacity. In order to obtain \dot{q}_{in} , the approach used was to calculate the heat rate output, \dot{q}_{out} , removed from the device's condenser, and then evaluate the overall energy balance.

Therefore, the condenser needed to be cooled using a method that allowed for both control and reliable calculation of \dot{q}_{out} . Those needs were met by a wind tunnel with air flow controlled by a frequency inverter, an equipment with several well-established correlations for heat transfer coefficient as a function of air velocity, air temperature and condenser geometry. The device was already available at the laboratory and the necessary parameters were obtained experimentally, using a K-type thermocouple to measure T_{∞} at the wind tunnel's inlet and a calibration curve for the mean cross section velocity as a function of the frequency set at the inverter.

3.2 EXPERIMENTAL PROCEDURE

Once the experimental setup was assembled, an experimental procedure and data reduction method were used to obtain the Nusselt number and the heat transfer coefficient for the wind tunnel, which allowed the heat transfer rate to be measured in transient state for subsequent experiments, as described in Section 3.2.1. After this method was consolidated, an experimental procedure was devised in order to study the solidification phenomenon.

First, a visualization experiment was performed to confirm the initial assumption that a critical solid layer of PCM would form in the beginning of the solidification, coinciding with the peak heat transfer rate for the latent heat transfer regime. This visualization procedure required rapid extraction of the thermosyphon from the PCM, which would not be possible with the thermosyphon attached to the wind tunnel. Therefore, the condenser was cooled using natural convection, and the transient heat transfer rate was not measured. This experiment corresponds to the tests listed as 1 through 6 on Table 3.4.

Then, once the initial assumption was validated, a baseline experiment was conducted without a PCM container attached to the closed thermosyphon, in order to provide a baseline for the transient behavior of the thermosyphon alone. The aim of this experiment was to separate the effects of thermal energy stored in the PCM from the inherent thermal inertia associated with the thermosyphon's heat capacity. The experiment consisted of tests 7 through 12 on Table 3.4, and was performed using the wind tunnel (forced convection) to cool the condenser of the thermosyphon.

Finally, the main experiment of this study was performed to assess the effect of PCM volume and external heat transfer coefficient on the solidification phenomenon. Once again the condenser of the thermosyphon was cooled using forced convection in the wind tunnel, and the thermosyphon was inserted into each of the three PCM containers (A, B and C) with different diameters, according to Table 3.4, where tests 13 to 16 correspond to PCM container A ($D_o = 2''$), tests 17 to 20 are those with PCM container B ($D_o = 1\frac{1}{2}''$), and tests 21 to 24 were made using PCM container C ($D_o = 1\frac{1}{4}''$). The varying sizes corresponded to varying quantities of naphthalene.

Table 3.4 – Tests performed with controlled power oscillations in the heat source.

Experiment	Test	D_e [m]	m_{PCM} [kg]	Cooling regime	v_∞ [m/s]	\dot{q}_{in} [W]
Visualization	01	0,05080	0,7315	Natural convection	-	25
	02	0,05080	0,7315	Natural convection	-	25
	03	0,03810	0,2350	Natural convection	-	25
	04	0,03810	0,2350	Natural convection	-	25
	05	0,03175	0,0962	Natural convection	-	25
	06	0,03175	0,0962	Natural convection	-	25
Baseline (no PCM)	07	-	0	Forced convection	4,45	40
	08	-	0	Forced convection	12,93	40
	09	-	0	Forced convection	4,45	60
	10	-	0	Forced convection	12,93	60
	11	-	0	Forced convection	4,45	80
	12	-	0	Forced convection	12,93	80
PCM Container A (2 ")	13	0,05080	0,7315	Forced convection	4,45	50
	14	0,05080	0,7315	Forced convection	6,83	60
	15	0,05080	0,7315	Forced convection	9,94	70
	16	0,05080	0,7315	Forced convection	12,93	80
PCMContainer B (1 1/2 ")	17	0,03810	0,2350	Forced convection	4,45	50
	18	0,03810	0,2350	Forced convection	6,83	60
	19	0,03810	0,2350	Forced convection	9,94	70
	20	0,03810	0,2350	Forced convection	12,93	80
PCMContainer C (1 1/4 ")	21	0,03175	0,0962	Forced convection	4,45	50
	22	0,03175	0,0962	Forced convection	6,83	60
	23	0,03175	0,0962	Forced convection	9,94	70
	24	0,03175	0,0962	Forced convection	12,93	80

3.2.1 EXPERIMENT AND DATA REDUCTION METHOD TO OBTAIN NUSSELT NUMBERS IN THE WIND TUNNEL

A data reduction method was used in order to calculate the Nusselt number, \overline{Nu}_d , related to the external heat transfer from the thermosyphon's condenser to the wind tunnel. This method consisted of comparing known correlations to experimental data and obtaining a semi-empirical model.

The first necessary step was to obtain a curve for air velocity on the wind tunnel, u_∞ , according to the frequency, f , set at the inverter. This was performed following the traverse method (ASHRAE, 2005), inserting a pitot-static tube in the tunnel's cross section and varying its position along the inner diameter to measure six points. This procedure was repeated for two perpendicular directions along the section and the total average of all measurements was assumed as the mean cross section velocity, u_∞ . During the procedure, the thermosyphon's condenser was inserted and maintained in the test section, to account for the effect of its geometry on the air flow.

Once the velocity versus frequency curve was known, a correlation was obtained for h_∞ , based on established literature correlations and on the results of experimental tests for this specific setup. These tests were performed on a simple thermosyphon, charged with refrigerant R141b at a fill ratio of F=60 %, and no PCM container attached. A total of nine tests were conducted to establish a correlation, for three set values of electric power input, P_{el} , and three inverter frequencies, f , as seen labeled from A to I in Table 3.5. The value of P_{el} was calculated simply as

$$\dot{q}_{ss} = P_{el} = iU \quad (3.1)$$

Where i is the current and U is the electrical potential. Since the system was considered to be well insulated, energy loss was assumed to be negligible and at steady state the heat transfer rate from the condenser was then equal to the power input, i. e., $\dot{q}_{ss} = P_{el}$.

The experimental value of \dot{q}_{ss} was then compared to the heat transfer rate predicted by Newton's Cooling Law, that is:

$$\dot{q} = h_\infty A_c (T_c - T_\infty) \quad (3.2)$$

where T_c is the average condenser temperature, measured using K-type thermocouples, A_c is the condenser external surface area, and h_∞ is the heat transfer coefficient of a cylinder under cross-flow forced convection, which can also be obtained from:

$$h_\infty = \frac{k_{air} \overline{Nu}_d}{d_o} \quad (3.3)$$

where k_{air} is air conductivity, d_e is the thermosyphon external diameter and \overline{Nu}_d is the Nusselt number for this configuration, for which there are several known correlations. This study used the correlations of Zukauskas (1972, apud INCROPERA *et al.*, 2008), Churchill and Bernstein, (1977 apud INCROPERA *et al.*, 2008), and Sparrow (2004), respectively:

$$\overline{Nu}_{d,z} = C_z Re_d^m Pr^n \left(\frac{Pr}{Pr_c} \right)^{1/4} \quad (3.4)$$

$$\overline{Nu}_{d,CB} = 0,3 + \frac{0,62 Re_d^{1/2} Pr^{1/3}}{[1 + (0,4/Pr)^{2/3}]^{1/4}} \left[1 + \left(\frac{Re_d}{282000} \right)^{5/8} \right]^{4/5} \quad (3.5)$$

$$\overline{Nu}_{d,S} = 0,25 + (0,4 Re_d^{1/2} + 0,06 Re_d^{2/3}) Pr^{0,37} \left(\frac{\mu}{\mu_c} \right)^{1/4} \quad (3.6)$$

for comparison with the correlation obtained in the present experimental setup. In these equations, Re_d refers to the Reynolds number obtained using diameter d_e , Pr and μ are the Prandtl number and the absolute viscosity of air, respectively, both obtained at T_∞ , while Pr_c and μ_c are obtained at T_c . The coefficients C_z and m assume different values according to Re_d , as seen in Table 3.6, whereas $n = 0,37$ for all values of $Pr < 10$.

After the tests were performed, experimental values were obtained for Nusselt number, $\overline{Nu}_{d,exp}$, by combining Eq. (3.2) and Eq. (3.3), resulting in:

$$\overline{Nu}_{d,exp} = \frac{d_e Pe_l}{k_{air} A_c (T_c - T_\infty)} \quad (3.7)$$

Then, these experimental values were compared with the Nusselt numbers predicted by the theoretical correlations for each test, according to their Reynolds numbers, which are presented in Section 5.1.1.

Lastly, a semi-empiric correlation is proposed, based on Zukauskas, Eq. (3.4) but with new coefficients, C_Z , m and n , obtained from the adjustment to the data from the wind tunnel used in this work. Thus, the correlation has the following format:

$$\overline{Nu}_{d,x} = C_Z Re_d^m Pr^n \left(\frac{Pr}{Pr_c} \right)^{1/4} \quad (3.8)$$

From this correlation, the heat transfer coefficient h_∞ is obtained using Eq. (3.3) and subsequently the heat transfer rate \dot{q} can be obtained using Eq. (3.2), which is valid for both steady state operation and the transient regime during power oscillations. The adjustment results of this correlation are also presented in Section 5.1.1. Tests J through Q of Table 3.5 were performed later to further validate the results of this correlation.

Table 3.5 – Tests performed to obtain a correlation for external heat transfer coefficient on the wind tunnel, h_∞ .

Test	Repetitions	D_e [m]	m_{PCM} [kg]	v_∞ [m/s]	P_{el} [W]
A	-	-	0	4,45	40
B	-	-	0	8,85	40
C	-	-	0	12,93	40
D	-	-	0	4,45	60
E	-	-	0	8,85	60
F	-	-	0	12,93	60
G	-	-	0	4,45	80
H	-	-	0	8,85	80
I	-	-	0	12,93	80
J	-	-	0	6,84	40
K	-	-	0	6,84	60
L	-	-	0	6,84	80
M	-	-	0	11,03	40
N	-	-	0	11,03	60
O	-	-	0	11,03	80
P	2	0,05080	0,7315	8,85	60

Q	3	0,05080	0,7315	11,03	80
---	---	---------	--------	-------	----

Table 3.6 – Coefficients used in Zukauskas' correlation, Eq. (3.4).

Re_d	C_z	m
1 – 40	0,75	0,4
40 – 1000	0,51	0,5
$10^3 – 2 \times 10^5$	0,26	0,6
$2 \times 10^5 – 10^6$	0,076	0,7

Source: INCROPERA *et al.* (2008).

3.2.2 VISUALIZATION EXPERIMENT

The visualization experiment corresponds to tests 1 through 6 in Table 3.4, where the thermosyphon was combined with each of the three PCM containers, in turn. Each combination was subjected to two tests; one where the liquid PCM was allowed to cool until fully solidified, and the other test where the cooling process was interrupted at the end of a critical solidification period in order to observe the state of the PCM and verify the existence of a critical solidified layer. Therefore, this experiment required the quick removal of the thermosyphon from the PCM container during operation, which was not possible if the condenser was attached to a wind tunnel. Therefore, instead of using a wind tunnel, natural convection was the cooling mechanism for the condenser, which was simply left exposed to ambient air. This meant that there was no reliable way to calculate heat transfer rate during transient regime in this experiment, making it a qualitative rather than quantitative analysis.

All six tests began by heating the PCM container until all the PCM was melted, and then supplying a constant heat transfer rate of $\dot{q}_{in} = 25$ W until the system reached steady-state, with the vapor temperature above melting point, which is $T_m = 80,3$ °C for naphthalene. Then, the heat supply was cut off, starting a cooling period on the entire system. For each PCM container, a full test was conducted, numbered 1, 3, and 5 in Table 3.4, corresponding to containers A (2”), B (1 1/2”) and C (1 1/4”), respectively. For these full tests, the system was allowed to cool until the highest temperature on the PCM thermocouples reached 70 °C, ten degrees lower than T_m , therefore ensuring that the PCM was fully solidified. Then, the power supply was turned on (25 W) again until the system achieved a steady-state condition. The results of these full tests, which are discussed in Section 5.1.2, were used to identify the critical

heat transfer rate during solidification and to define a parameter to monitor this critical period. This parameter was then used for the interrupted tests, numbered 2, 4, and 6 in Table 3.4, corresponding to containers A (2”), B (1 1/2”) and C (1 1/4”), respectively. For the interrupted tests, the evaporator was removed from the PCM container at the end of the critical solidification period, and the state of the PCM was recorded and analyzed.

During the cooling period, three separate regimes were expected: (A) liquid sensible cooling, in which the material is entirely in liquid phase and temperatures decrease until the PCM reaches its melting point; (B) latent cooling, in which the material undergoes liquid-solid phase change, releasing latent heat onto the thermosyphon; (C) solid sensible cooling, in which the PCM is solid and temperatures decrease once more, releasing sensible heat onto the thermosyphon.

3.2.3 BASELINE EXPERIMENT

Before beginning the main experiment properly, a series of baseline tests were performed without a PCM container attached to the closed thermosyphon, identified as tests 7 through 12 on Table 3.4. These tests aimed to provide a baseline for the transient behavior of the thermosyphon alone, in order to separate the effects of thermal energy stored in the PCM from the inherent thermal inertia associated with the thermosyphon’s heat capacity. For this experiment, the condenser was inserted in the wind tunnel for cooling (forced convection), in order to calculate the heat transfer rate during the transient cooling regime, which was later compared to the tests with PCM over the same period. The device was supplied with heat by the heating tape, which was attached to the outer wall of the thermosyphon evaporator.

All six tests began by heating the evaporator until the system reached steady-state, supplying a constant value of electrical power, P_{el} , which corresponds to a constant heat transfer rate, q_{in} . Table 3.4 shows that a total of three values of P_{el} were tested, each paired with two values of air velocity in the wind tunnel, v_{∞} , corresponding to the minimum and maximum limits used to obtain the correlation for external convection heat transfer coefficient (h_{∞}). Then, the heat supply was cut off, causing a cooling period on the entire system. After a period of $\Delta t = 10$ min, the supply was restored, and the system was allowed to return to steady state operation. This arbitrary time limit was set as a constant parameter, since there was no PCM phase change to impose an observable end criterion for the thermal oscillation. The cooling regime was expected to consist simply of sensible heat, as the temperature of all materials that

compose the system (thermosyphon walls and working fluid) decreased, releasing heat through the condenser.

3.2.4 MAIN EXPERIMENT

The main experiment was composed of tests 13 through 24 on Table 3.4. The thermosyphon's condenser was cooled by forced convection using the wind tunnel, for better control of the heat transfer rate during transient cooling, while the evaporator was inserted in each of the three PCM containers in turn. The heat rate at the system's inlet, \dot{q}_{in} , and the heat transfer coefficient at its outlet, h_{∞} , were easily set using the power source and the wind tunnel's velocity, v_{∞} , which was controlled using the frequency inverter and the curve obtained as described in Section 3.2.1. In order to observe the thermal behavior of the system when subjected to increasingly intense cooling conditions, a total of four values of v_{∞} were tested: 4,45 m/s, 6,83 m/s, 9,94 m/s and 12,93 m/s. The input value of \dot{q}_{in} was adjusted for each set of v_{∞} so as to provide similar initial state conditions for all tests, mainly ensuring that the vapor temperature in the thermosyphon was above T_m and the PCM was fully melted at steady state operation. Table 3.4 shows the tests separated according to the diameter of the associated PCM container, where tests 12 to 16 correspond to PCM container A ($D_o = 2''$), tests 17 to 20 are those with PCM container B ($D_o = 1\frac{1}{2}''$), and tests 21 to 24 were made using PCM container C ($D_o = 1\frac{1}{4}''$). The varying sizes corresponded to varying quantities of naphthalene, in order to study the effects of PCM mass and volume on the system's capacity to store and release heat during a thermal oscillation.

All tests began by heating the PCM container until the system reached steady-state, supplying a constant heat transfer rate, \dot{q}_{in} . Then, similarly to the visualization experiment, the heat supply was cut off, causing a cooling period on the entire system until the highest temperature on the PCM thermocouples decreased to 70 °C, which is ten degrees lower than T_m , therefore ensuring that the PCM was fully solidified. Then, the power supply was restored until the system achieved steady-state operation once again. The cooling regime was expected to be composed of the same three stages described in section 3.2.2: (A) liquid sensible cooling; (B) latent cooling; and (C) solid sensible cooling.

4. ANALYTICAL MODELS

This chapter proposes analytical models for the studied device, beginning with the initial steady state operation and then focusing on the cooling period, specifically for the first two cooling regimes described in Section 3.2.2, meaning (A) liquid sensible cooling, in which the material is entirely in liquid phase and temperatures decrease until the PCM reaches its melting point; and (B) latent cooling, in which the material undergoes liquid-solid phase change, releasing latent heat onto the thermosyphon.

4.1 MODELS FOR STEADY STATE OPERATION

The initial steady state operation model serves as a foundation for the later analytical models, since it provides a stable condition, with known and controlled parameters. The analytical modeling of a thermosyphon is made using thermal resistances, making use of an analogy between thermal and electrical circuits, in which the total temperature difference between heat source and heat sink acts in a similar manner to an electric potential difference, and each section of the closed thermosyphon is represented by an individual thermal resistance. The combination of all individual resistances gives a total equivalent thermosyphon resistance, R_{CTPT} , as defined by:

$$R_{CTPT} = \frac{T_{evap} - T_{cond}}{\dot{q}} = \frac{\Delta T_{CTPT}}{\dot{q}} \quad (4.1)$$

where T_{evap} and T_{cond} are the temperatures of the evaporator and condenser, respectively, and \dot{q} is the heat transfer rate through the thermosyphon. This model makes it possible to estimate the medium operating temperature, T_v , which can be considered the same as the vapor temperature at the adiabatic section, T_a (OCHTERBECK, 2003).

The PCM container's thermal behavior was determined from the energy balances seen in Figure 4.1, combined with the knowledge of the geometry and thermodynamic properties of the liquid in its enclosure. Afterwards, the PCM container's heat transfer capacity was expressed in the form of a thermal resistance, R_{PCM} , and added to the system's thermal circuit. This analysis is represented in the diagram in Figure 4.2, which shows the energy balance over control volumes, C.V., signaled by dashed lines surrounding (a) the PCM container, which

receives a heat rate $\dot{q}_{in,PCM}$ from the power source, and releases the same heat rate to the evaporator of the thermosyphon, as $\dot{q}_{out,PCM}$; (b) the thermosyphon, which receives $\dot{q}_{out,PCM}$ from the PCM container, and loses a heat rate \dot{q}_{out} to the heat sink (wind tunnel). This information is complemented by the thermal circuit shown in Figure 4.2, where the external resistance between the condenser and the wind tunnel is represented by R_9 . The following sections discuss each of these energy balances and the resulting thermal resistances for the system.

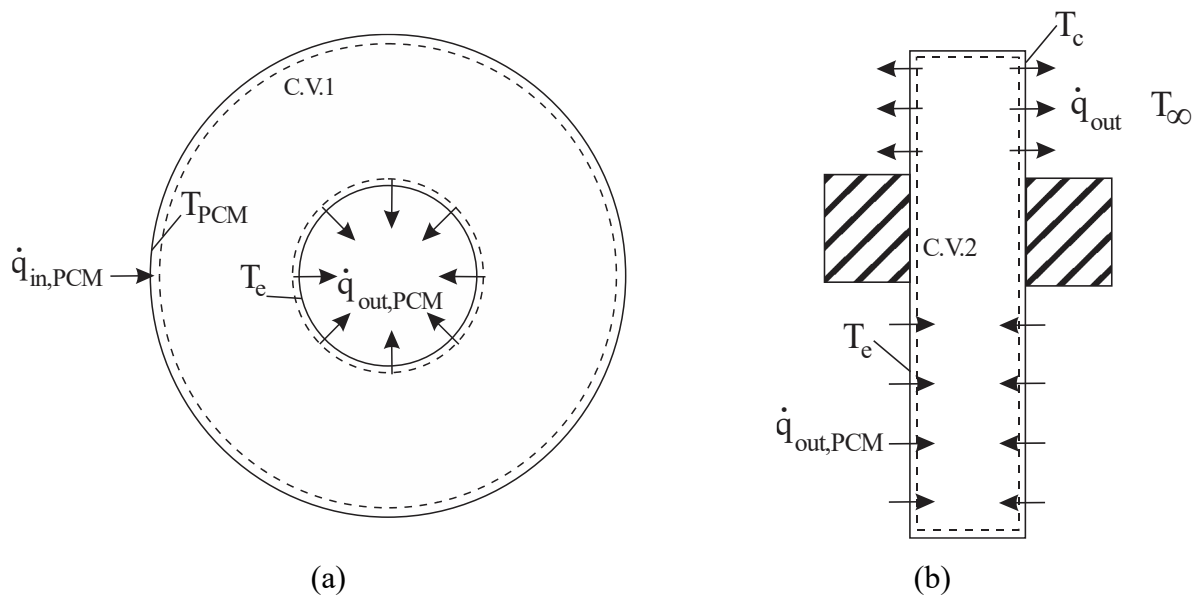


Figure 4.1. Energy balances considered for the steady state analysis, over control volumes, C.V., signaled by dashed lines surrounding: (a) the PCM container; (b) the thermosyphon.

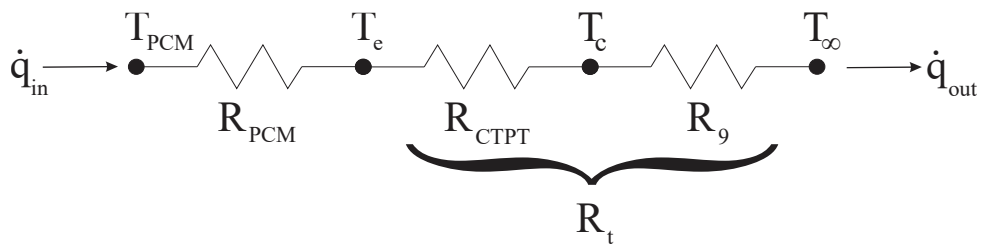


Figure 4.2. Simplified thermal resistance circuit for the complete system, combining both energy balances in Figure 4.1.

4.1.1 THE THERMOSYPHON THERMAL RESISTANCE

Schematics of the thermal circuit, adopted as the model in the present work can be seen in Figure 4.3, where T_1 and T_2 are the heat source and heat sink temperatures, respectively. The thermal resistances are defined as follows:

- R_1 : external thermal resistance between the evaporator and the heat source;
- R_2 : radial conduction resistance on the evaporator wall;
- R_3 : evaporation heat transfer resistance;
- R_4 : thermal resistance on the liquid – vapor interface in the evaporator;
- R_5 : thermal resistance due to the vapor flow along the thermosyphon;
- R_6 : thermal resistance on the liquid – vapor interface in the condenser;
- R_7 : condensation heat transfer resistance;
- R_8 : radial conduction resistance on the condenser wall;
- R_9 : external thermal resistance between the condenser and the heat sink;
- R_{10} : axial conduction resistance on the thermosyphon wall.

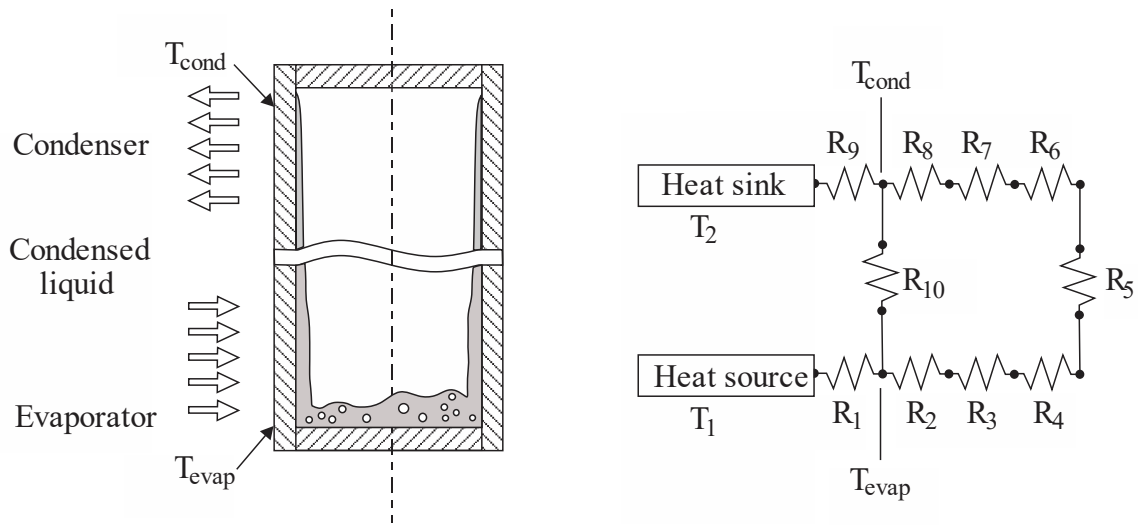


Figure 4.3. Thermal resistance circuit of a closed two-phase thermosyphon. Adapted from Mantelli (2021).

The external resistances R_1 and R_9 are calculated according to the heat transfer mechanism, which must be evaluated case by case. Resistances R_4 , R_5 and R_6 can generally be considered negligible (MANTELLI, 2021), so the total equivalent resistance R_{eq} is calculated as:

$$R_{eq} = R_1 + [(R_2 + R_3 + R_7 + R_8)^{-1} + R_{10}^{-1}]^{-1} + R_9 \quad (4.2)$$

Typically, R_{10} has a considerably greater order of magnitude than the other resistances, with which it is connected in parallel, as seen in Figure 4.3. This means that the heat flow avoids the path of axial conduction, and the contribution of R_{10} becomes negligible (MANTELLI, 2012).

In cylindrical tubes, both radial conduction resistances are given by:

$$R_2 = R_8 = \frac{\ln(r_o/r_i)}{2\pi lk_p} \quad (4.3)$$

where r_o is the outer diameter of the thermosyphon tube wall, r_i is its inner diameter, and l is either the evaporator length, l_e , for R_2 , or the condenser length, l_c , for R_8 .

The evaporation resistance, R_3 , describes heat transfer associated with liquid–vapor phase change, which is a more complex phenomenon than simple heat conduction. Several models have been developed for each, with the present study focusing on those of Groll and Rosler (1992), $R_{3,GR}$, Farsi *et al.* (2003), $R_{3,F}$, and Kiyomura *et al.* (2017), $R_{3,K}$. The first model divides the overall evaporation resistance into two components – one related to the liquid pool accumulated at the bottom of the evaporator, and the other related to the liquid film coating the evaporator walls. Therefore, $R_{3,GR}$ is composed of one film evaporation resistance, R_{3f} and one pool boiling resistance, R_{3p} , related to a fill ratio F , or the ratio of fluid volume to total evaporator volume, as follows (GROLL; ROSLER, 1992):

$$R_{3,GR} = FR_{3p} + (1 - F)R_{3f} \quad (4.4)$$

The pool boiling resistance, R_{3p} , is given by:

$$R_{3p} = (g^{0,2} \phi_1 \dot{q}_{in}^{0,4} (2\pi r_i l_e)^{0,6})^{-1}; \quad (4.5)$$

where g is gravity, \dot{q}_{in} is the heat transfer input, and ϕ_1 is defined by:

$$\phi_1 = \frac{c_{p,l}^{0,7} k_l^{0,3} \rho_l^{0,65}}{\rho_v^{0,25} h_{lv}^{0,4} \mu_l^{0,1}} \left(\frac{p_v}{p_{atm}} \right)^{0,23} \quad (4.6)$$

where ρ_l , k_l and $c_{p,l}$ are the specific mass, thermal conductivity and specific heat, respectively, for the working fluid in liquid phase; ρ_v and p_v are the specific mass and pressure of the fluid in vapor phase; and p_{atm} is atmospheric pressure.

Groll and Rosler propose the same correlation for film evaporation, R_{3f} , and film condensation, $R_{7,GR}$, based on the Nusselt condensation model and given by:

$$R_{3f} = R_{7,GR} = \frac{0,345\dot{q}_{in}^{1/3}}{d_i^{4/3}g^{1/3}l\phi_2^{4/3}} \quad (4.7)$$

where l must be replaced by l_e when calculating R_{3f} or by l_c when calculating R_7 , and ϕ_2 is defined as:

$$\phi_2 = \left(\frac{h_{lv}k_l^3\rho_l^2}{\mu_l} \right)^{\frac{1}{4}} \quad (4.8)$$

Farsi's correlation for evaporation resistance, $R_{3,F}$, was developed based on experimental results for a low temperature working fluid, n-pentane, and considers pool boiling to be responsible for most of the evaporation heat transfer. It is similar to Eq. (4.5), with the addition of a constant $C_e = 0,263$ to compensate for film boiling effects, and is given by:

$$R_{3,F} = (C_e\phi_1g^{0,2}\phi_1\dot{q}_{in}^{0,4}(2\pi r_i l_e)^{0,6})^{-1} \quad (4.9)$$

Another evaporation correlation centered on pool boiling, $R_{3,K}$, is given by Kiyomura as:

$$R_{3,K} = \frac{\left(\frac{c_{p,l}\mu_l}{k_l}\right)^{0,34} \left(\frac{s}{L_m}\right)^{-0,5}}{154 \left(\frac{k_l}{L_m}\right) \left[\frac{c_{p,l}(T_v+273,15)}{h_{lv}}\right]^{1,72} \left(\frac{D_b\dot{q}_{in}}{\mu_l h_{lv}}\right)^{0,62} (2\pi r_i l_e)^{0,38}} \quad (4.10)$$

where s is the gap size between the heated surface and the confining element, given as $s = 0,013$ m under unconfined conditions, σ is the fluid's surface tension in the liquid-vapor interface, α_l is the liquid thermal diffusivity, L_m is the capillary length, given by:

$$L_m = \sqrt{\frac{\sigma}{g(\rho_l - \rho_v)}} \quad (4.11)$$

where D_b is the bubble departure diameter, which for low temperature fluids is given by (GORENFLO, 1986):

$$D_b = 16 \left(\frac{Ja^4 \alpha_l^{0,5}}{g} \right)^{1/3} \left[1 + \left(1 + \frac{2\pi}{3Ja} \right)^{0,5} \right]^{4/3} \quad (4.12)$$

and Ja is the Jakob number, defined as:

$$Ja = \rho_l c_{p,l} \left(\frac{\dot{q}_{in} R_{3,K}}{\rho_v h_{lv}} \right) \quad (4.13)$$

The presence of $R_{3,K}$ in Eq. (4.13) signifies that this correlation requires an iterative approach, with an initial estimation of R_3 .

The condensation thermal resistance, R_7 , also refers to phase change heat transfer and has been modeled by several different authors. In this study, three main correlations are taken note of – that of Groll and Rosler (GROLL; ROSLER, 1992), $R_{7,GR}$, already given by Eq. (4.7) and based on the Nusselt film condensation model; then the modified Nusselt correlation, $R_{7,N}$ (GROSS, 1992) and given by:

$$R_{7,N} = \frac{\delta_v}{0,925 Re_l^{1/3} k_l \pi d_i l_c} \quad (4.14)$$

and the Kaminaga correlation (*apud* BELLANI, 2017), $R_{7,K}$, given by:

$$R_{7,K} = \frac{1}{25 Re_l^{1/4} Pr_l^{2/5} k_l \pi l_c} \quad (4.15)$$

The first two correlations consider the condensation film to have a laminar flow, and assume the effect of shear stress on the liquid-vapor interface to be negligible, whereas the Kaminaga

correlation considers the convection effects of the vapor flow and is recommended when the liquid flow regime is turbulent and cannot be recognized. The liquid flow Reynolds number, Re_l , is defined as:

$$Re_l = \frac{4\dot{q}_{in}}{\pi d_i h_{lv} \mu_l} \quad (4.16)$$

and the characteristic length, δ_v , is given by:

$$\delta_v = \left[\frac{\mu_l^2}{g \rho_l (\rho_l - \rho_v)} \right]^{1/3} \quad (4.17)$$

The choice of the appropriate correlations for R_3 and R_7 must be evaluated for each case, preferably backed by experimental data. Once the choice is made, the overall evaporator resistance, R_{evap} , can be obtained as a sum of the evaporation and conduction resistances, as seen in:

$$R_{evap} = R_2 + R_3 \quad (4.18)$$

Similarly, the overall condenser resistance, R_{cond} , is given by:

$$R_{cond} = R_7 + R_8 \quad (4.19)$$

Considering that R_{10} is negligible, as mentioned, this means that the overall internal resistance of the closed two-phase thermosyphon, R_{CTPT} , is given by:

$$R_{CTPT} = R_{evap} + R_{cond} \quad (4.20)$$

which can be combined with Eq. (4.2) for the total equivalent resistance R_{eq} as in:

$$R_{eq} = R_1 + R_{CTPT} + R_9 \quad (4.21)$$

4.1.2 THE PCM CONTAINER THERMAL RESISTANCE

In this study, the external evaporator resistance, R_1 , is the PCM resistance, R_{PCM} , since the PCM container is placed between the system's heat source and the thermosyphon's evaporator. Therefore, the total equivalent resistance, R_{eq} , of this device is given by:

$$R_{eq} = R_{PCM} + R_{CTPT} + R_9 \quad (4.22)$$

In order to obtain R_{PCM} , it was necessary to assess which heat transfer mechanism was predominant in the liquid PCM pool, whether that was conduction or convection. This assessment was made using scale analysis, according to Bejan (2013), by approximating the cylindrical, annular cavity of the PCM container to a two-dimensional rectangular enclosure, for simplification. The dismissal of volumetric effects was justified by the fact that the container is maintained vertically upright, thermally insulated on the top and bottom ends, and heated evenly from the side, so that the heat transfer can be considered to occur only in the radial direction. The approximated rectangular enclosure is seen in Figure 4.4, where the x-axis represents the radial direction, starting from the outer wall of the container, the length, L , is obtained according to:

$$L = \frac{D_i - d_o}{2} \quad (4.23)$$

and vertical height, H , is equal to the evaporator length, as seen in:

$$H = l_e \quad (4.24)$$

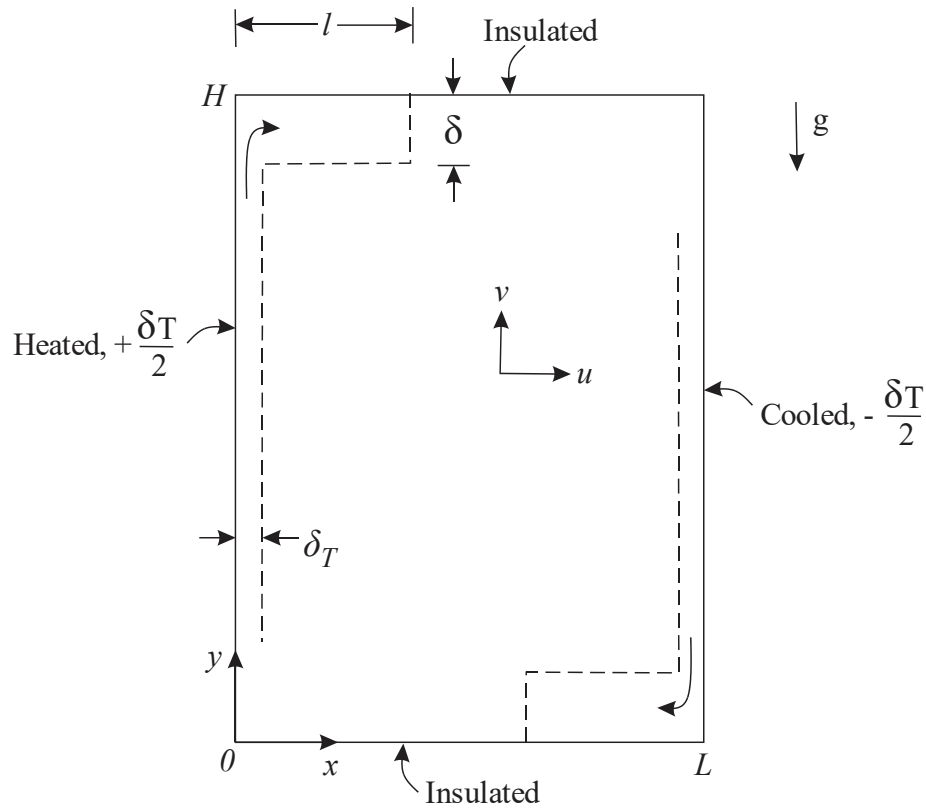


Figure 4.4. Two-dimensional rectangular enclosure with isothermal side walls. Adapted from Bejan (2013).

According to Bejan (2013), an analysis of the system's aspect ratio, H/L , and its Rayleigh number, Ra_H , can determine whether or not distinct thermal boundary layers are formed along each vertical wall, with a relatively stagnant core in the center of the liquid pool. If this is the case, then natural convection has a more significant role than conduction in the system's heat transfer. Otherwise, conduction prevails and natural convection can be dismissed from the analysis. The definition of Ra_H is seen in:

$$Ra_H = \frac{g\beta\Delta TH^3}{\nu\alpha} \quad (4.25)$$

whereas the criteria for considering natural convection relevant is given by:

$$Ra_H^{-1/4} < H/L < Ra_H^{1/4} \quad (4.26)$$

in which g is gravity, β , ν , α , are respectively the PCM's thermal expansion coefficient, kinematic viscosity, and thermal diffusivity, and ΔT is the temperature difference between the outer and inner wall of the enclosure.

The experimental results seen in Section 5.2.2 show that for all cases of the main experiment, the condition of Eq. (4.26) is met, meaning that the effects of natural convection are significant within the PCM container. However, this form of heat transfer is more complex than pure conduction, and even if an analytical model was obtained for the heat transfer coefficient under steady state, it would not directly apply to the transient cooling regime, since models for convection heat transfer coefficient are dependent on boundary conditions and form of heating. This means that even a thorough analytical model would be reduced to an approximation once the system was subjected to transient cooling, which is the state this study is most concerned with. Therefore, a simpler approach was chosen for modeling heat transfer in the PCM by treating all cases as pure thermal conduction problems, by approximating the total heat transfer coefficient to an effective thermal conductivity, k_{eff} , which accounts for both the conduction and convective heat transfer that actually occur, as proposed by Beckman (*apud* RAITHBY; HOLLANDS, 1975) for another case of free convection within an annular cylinder, and is given by:

$$k_{eff} = \frac{\ln(D_i/d_o) \dot{q}}{2\pi l_e \Delta T} \quad (4.27)$$

For the case of a horizontal annular cylinder, RAITHBY & HOLLANDS (1975) go on to propose a semi-empirical correlation in the form of:

$$\frac{k_{eff}}{k_l} = C_1 (Ra_{LC})^{C_2} \quad (4.28)$$

where k_l is the liquid thermal conductivity of the PCM, C_1 and C_2 are constants adjusted to the experimental data considered in the original study, and Ra_{LC} is a modified Rayleigh number for concentric cylinders.

The exact equation obtained by Raithby and Hollands (1975) could not be applied to the case of this study, which consists of a vertical annular cylinder. However, its overall form was used as a basis to obtain a semi-empirical correlation with different coefficients C_1 and C_2 , based on the data from the main experiment of this study. The definition of Ra_{LC} is similar to that of Ra_H in Eq. (4.25), but replacing H with the characteristic length L_c , given by:

$$L_c = \sqrt{D_i^2 - d_o^2} \quad (4.29)$$

This solution was still insufficient, since knowledge of the experimental parameter ΔT is required in order to obtain the variable Ra_{Lc} , rendering Eq. (4.28) incapable of predicting the value of k_{eff} from project parameters alone. Therefore, the problem was reformulated to eliminate this dependence. The first step was to combine Eq. (4.27) to the definition of Ra_{Lc} , as seen in to yield:

$$Ra_{Lc} = \frac{g\beta L_c^3}{\nu\alpha} \times \frac{\ln(D_i/d_o) \dot{q}}{2\pi l_e k_{eff}} \quad (4.30)$$

Next, Eq. (4.30) was rewritten as:

$$Ra_{Lc} = \frac{g\beta L_c^3}{\nu\alpha} \times \frac{\ln(D_i/d_e)}{\underbrace{2\pi l_e k_l}_{R_{kl}}} \times \dot{q} \times \frac{k_l}{\underbrace{k_{eff}}_{1/k_x}} \quad (4.31)$$

Eq. (4.31), which was then transformed into:

$$Ra_{Lc} = \frac{g\beta L_c^3}{\nu\alpha} \times \frac{(R_{kl} \dot{q})}{\Delta T_{kl}} \times \frac{1}{k_x} \quad (4.32)$$

where R_{kl} is the conduction thermal resistance, associated with the PCM's liquid thermal conductivity, k_l , and k_x is the ratio of effective to liquid thermal conductivity.

Then, an equivalent temperature difference, ΔT_{kl} , was defined as the theoretical ΔT that would take place in case the problem was defined by pure conduction in the liquid PCM. With this equivalent temperature difference, a corresponding equivalent Rayleigh number, Ra_{Lc}^* , is seen in:

$$Ra_{Lc} = \frac{g\beta L_c^3 \Delta T_{kl}}{\underbrace{\nu\alpha}_{Ra_{Lc}^*}} \times \frac{1}{k_x} \quad (4.33)$$

which was rewritten, lastly, as:

$$Ra_{Lc} = \frac{Ra_{Lc}^*}{k_x} \quad (4.34)$$

Combining Eq. (4.34) with Eq. (4.28) results in:

$$\frac{k_x}{k_{eff}/k_l} = C_1 \left(\frac{Ra_{Lc}^*}{k_x} \right)^{C_2} \quad (4.35)$$

which is rewritten as:

$$\frac{k_{eff}}{k_l} = C_3 (Ra_{Lc}^*)^{C_4} \quad (4.36)$$

incorporating new coefficients C_3 and C_4 , which must then be obtained and adjusted from experimental data. Since Ra_{Lc}^* can be calculated from the PCM's thermophysical properties and the project parameters, the semi-empirical correlation given by Eq. (4.36) can be used to predict effective thermal conductivity.

In order to determine the coefficients C_3 and C_4 , a semi-empirical correlation fits the experimental values of k_{eff} , which can be calculated using the following equation:

$$k_{eff} = \frac{\dot{q}}{(T_{PCM} - T_e)} \frac{\ln(D_i/d_e)}{2\pi l_e} \quad (4.37)$$

where T_{PCM} is the average temperature along the wall of the PCM container.

Once the heat transfer coefficients in the liquid PCM pool have been expressed as an effective conductivity, the thermal resistance R_{PCM} can be treated as pure conduction resistance, given by:

$$R_{PCM} = \frac{\ln(D_i/d_e)}{2\pi k_{eff} l_e} \quad (4.38)$$

4.2 MODELS FOR TRANSIENT STATE: LIQUID SENSIBLE COOLING

In this section, an analytical model is proposed for the behavior of the studied device during the first phase of the cooling transient, immediately after the power supply at the heat source had been cut off. During this period, the liquid PCM pool becomes the system's heat source, as it provides sensible heat to the thermosyphon, which transfers heat to the wind tunnel, the system's heat sink. This stage is therefore called the sensible liquid cooling, labeled (A) in Section 3.2.2, and was modeled using energy balances on the PCM container and the closed two-phase thermosyphon.

As discussed in Section 4.1, the predominant form of heat transfer in the PCM pool was natural convection, which is especially difficult to model for transient systems. The solution used in the previous section, for steady state, will also be applied here. It consists of treating the heat transfer phenomena inside the liquid naphthalene pool as pure conduction with an effective conductivity, k_{eff} . Steady state operation was assumed as the initial condition for this analysis. Then, the PCM container was suddenly subjected to a convective cooling coefficient, h_{eq} , at the interface with the evaporator surface, while the outer PCM surface was thermally insulated.

The first energy balance of this analysis is performed on a control volume, $C.V. 1$, surrounding the naphthalene pool as seen in Figure 4.5 (a), which shows a diagram of the PCM container's cross section. This energy balance results in:

$$-\left(\frac{dE}{dt}\right)_{C.V.1} = \dot{q}_{PCM} \quad (4.39)$$

associating the overall heat transfer rate leaving the control volume, \dot{q}_{PCM} , to the rate it's the internal energy declines, $\left(\frac{dE}{dt}\right)_{C.V.1}$. Then, another energy balance is performed around a second control volume, $C.V. 2$, surrounding the closed two-phase thermosyphon, as seen in Figure 4.5

(b). The heat transfer rate leaving *C.V. 1*, enters *C.V. 2.*, and finally leaves the system, \dot{q}_{out} , as represented by the thermal circuit in Figure 4.6. This second energy balance results in:

$$\dot{q}_{PCM} = h_{eq} A_e (T_e(t) - T_\infty) \quad (4.40)$$

after assuming that $\dot{q}_{out} = \dot{q}_{PCM}$, where \dot{q}_{out} is all the heat that leaves the thermosyphon, and the equivalent convective coefficient, h_{eq} , is given by:

$$h_{eq} = \frac{1}{R_t A_e} \quad (4.41)$$

as a function of the total thermal resistance, R_t . This total resistance is obtained from:

$$R_t = R_{CTPT} + R_9 \quad (4.42)$$

in which R_{CTPT} and R_9 are assumed as the same from steady state operation.

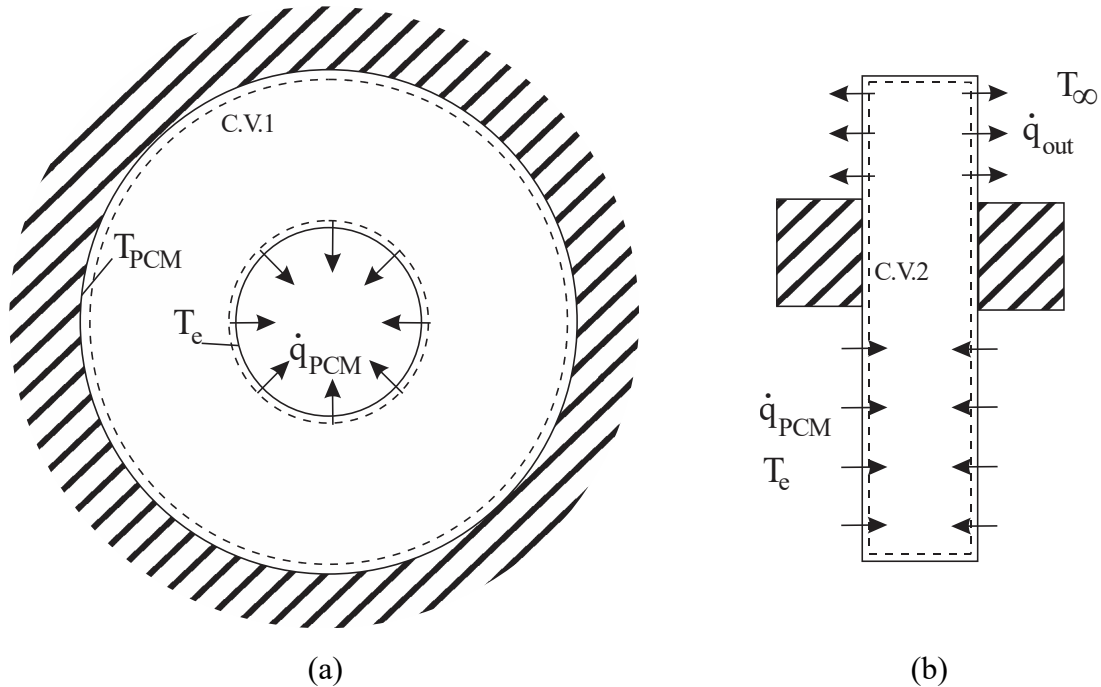


Figure 4.5. Energy balances on the control volumes, C.V., defined by dashed lines: (a) PCM container, where \dot{q}_{PCM} is the heat rate leaving the PCM; (b) thermosyphon, which receives \dot{q}_{PCM} from the PCM container, and releases \dot{q}_{out} to the heat sink (wind tunnel).

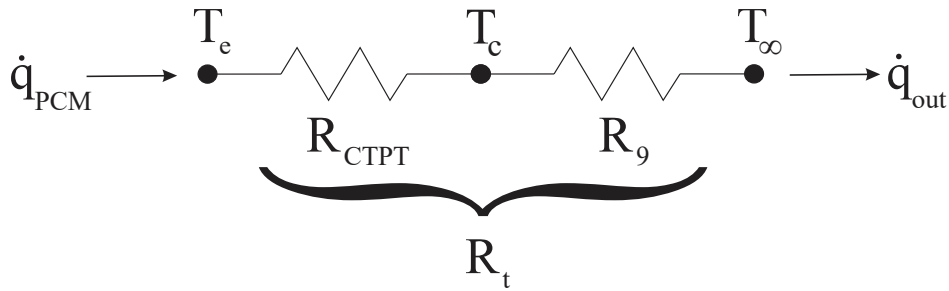


Figure 4.6. Simplified thermal resistance circuit for the energy balance of Figure 4.5 (b).

4.2.1 LUMPED HEAT CAPACITANCE

The simplest approach to modeling a thermal system in transient state is the lumped capacitance model, which treat the system as a solid object of homogenous temperature, T_0 , that varies uniformly over time. However, this assumption is not valid for transient analyses, and the applicability of the lumped capacitance model needs to be assessed before it can be implemented. A criterion for its validity is defined by INCROPERA (2008), based on the system's Biot number, Bi_L , a dimensionless parameter comparing the system's internal conduction resistance to its external convection resistance. If $Bi_L < 0,1$, then the assumption of a uniform internal temperature is reasonable. The definition of Bi_L for the studied device is given by:

$$Bi_L = \frac{h_{eq}L}{k_{eff}} \quad (4.43)$$

where L is the characteristic length given by:

$$L = \frac{V}{A_s} \quad (4.44)$$

where V is the PCM container's internal volume and A_s is the surface area subjected to convection heat transfer, which in this case is the evaporator external area, A_e . Therefore, Eq. (4.44) can be rewritten as:

$$L = \frac{L_c^2}{4d_o} \quad (4.45)$$

The resulting values of Bi_L for the main experiment are given in Section 5.2.2, with the highest value being $Bi_L = 0,32$ for test 16 (Table 3.4) and the lowest being $Bi_L = 0,19$ for test 21 (Table 3.4). These values did not satisfy the criterion $Bi_L < 0,1$, indicating that the temperature gradient and heat transfer phenomena within the PCM are not negligible, and must be taken into consideration when modeling the transient sensible cooling regime.

4.2.2 1D TRANSIENT HEAT CONDUCTION

Considering that the lumped capacitance model could not be applied to the present problem, a more comprehensive solution was needed in order to account for temperature distribution inside the PCM. With the approximation that heat transfer is by conduction, the problem becomes transient heat conduction over the geometry of an annular cylinder. An analysis of the energy balance in Figure 4.5 (a) shows that heat flows only in the radial direction, making it a one-dimensional problem, assuming that the device is well insulated. The problem can be described by Fourier's law as:

$$\frac{\partial T}{\partial t} = \frac{\alpha_{eff}}{r} \frac{\partial}{\partial r} \left(\frac{\partial T}{\partial r} \right) \quad (4.46)$$

This partial differential equation requires an initial condition and two boundary conditions. The first boundary condition is given on the outer radius, $r_2 = D_o/2$, where *C.V. 1* is thermally insulated, that is:

$$r = r_2, \quad \frac{\partial T}{\partial r} = 0 \quad (4.47)$$

The second boundary condition is at the inner radius diameter of the control volume, $r_1 = d_e/2$, where it is subjected to convection heat transfer with a constant equivalent heat transfer coefficient, h_{eq} , defined in Eq. (4.41). The second boundary condition is therefore given by:

$$r = r_1, \quad -k_{eff} \frac{\partial T}{\partial r} = h_{eq}(T_\infty - T) \quad (4.48)$$

The initial condition is the steady state operation. Considering the initial constant heat transfer rate input, $\dot{q}_{in,SS}$, as:

$$t = 0, \quad \dot{q}_{in,SS} = k_{eff} A_e \frac{dT}{dr} \quad (4.49)$$

an ordinary differential equation was solved into:

$$t = 0, \quad T(r) - T_{1,SS} = \frac{\dot{q}_{in,SS}}{2\pi l_e k_{eff}} \ln(r/r_1) \quad (4.50)$$

where $T_{1,SS}$ is the steady state evaporator temperature, T_e , and $T = T(r, t)$ is the PCM temperature as a function of position and time. Thus, Eq. (4.50) gives the PCM temperature gradient at steady state, and can be more directly used as the initial condition for the transient state. Therefore, the liquid sensible cooling regime is entirely defined as a one dimensional (1D) transient heat conduction problem with equations (4.46), (4.47), (4.48) and (4.50).

In order to solve the 1D transient conduction problem, it was first expressed in dimensionless terms, as defined in Eqs. (4.51) to (4.58), in Table 4.1. The characteristic length L_c , is the same as given by Eq. (4.29), and $(\rho c_p)_{PCM}$ represents the overall heat capacity of the PCM container, including the liquid naphthalene pool and the vessel walls.

Table 4.1 – Dimensionless variables for the 1D transient heat conduction analyses.

$\theta = \frac{T - T_\infty}{\theta_1}$ (4.51)	$\theta_1 = T_{1,SS} - T_\infty$ (4.52)
$\xi = r/L_c$ (4.53)	$Bi = \frac{h_{eq} L_c}{k_{eff}}$ (4.54)
$L_c = \sqrt{D_i^2 - d_e^2}$ (4.55)	$R_x = (2\pi l_e k_{eff} R_t)^{-1}$ (4.56)
$FO = \frac{\alpha_{eff} t}{L_c^2}$ (4.57)	$\alpha_{eff} = \frac{k_{eff}}{(\rho c_p)_{PCM}}$ (4.58)

In dimensionless form, the problem is described by:

$$\frac{\partial \theta}{\partial Fo} = \frac{\partial^2 \theta}{\partial \xi^2} + \frac{1}{\xi} \frac{\partial \theta}{\partial \xi} \quad (4.59)$$

with boundary condition at the outer PCM wall, *B. C. 1*, defined as:

$$B.C. 1: \quad \xi = \xi_2, \quad \frac{\partial \theta}{\partial \xi} = 0 \quad (4.60)$$

and at the inner wall, *B. C. 2*, given by:

$$B.C. 2: \quad \xi = \xi_1, \quad \frac{\partial \theta}{\partial \xi} = \theta \cdot Bi \quad (4.61)$$

and initial condition, *I. C.*, as defined in:

$$I.C.: \quad Fo = 0, \quad \theta = R_x \ln\left(\frac{\xi}{\xi_1}\right) + 1 \quad (4.62)$$

This constitutes a homogenous partial differential equation, with homogenous boundary conditions, which can be solved by separation of variables. Kreyszig (2010) presents the separation of variables method in details.

The separation of variables method proposes a solution $\theta(\xi, Fo)$ divided into two distinct functions of space and time, $F(\xi)$ and $G(Fo)$, respectively, as seen in:

$$\theta(\xi, Fo) = F(\xi) \cdot G(Fo) \quad (4.63)$$

Differentiation of this solution allows one to rewrite Eq. (4.59) as:

$$\frac{G'}{G} = \frac{F''}{F} + \frac{1}{\xi} \cdot \frac{F'}{F} \quad (4.64)$$

One should note that the left-hand side of this equation is a function only of Fo , while the right side is only a function of ξ . The only way for them to be equal to each other, is if both are equal to a constant, defined as $-\lambda^2$. The left-hand side of Eq. (4.64) can be rewritten as:

$$G' + \lambda^2 G = 0 \quad (4.65)$$

while the right-hand side becomes:

$$F'' + \frac{1}{\varepsilon} F' + \lambda^2 F = 0 \quad (4.66)$$

Both Eq. (4.65) and Eq. (4.66) are ordinary differential equations. Integration of Eq. (4.65) gives a straightforward solution to the transient function $G(Fo)$ as:

$$G(Fo) = \exp(-\lambda^2 Fo) \quad (4.67)$$

where the value of λ is yet unknown. As for Eq. (4.66), related to the function of space $F(\xi)$, it is recognized as a Bessel differential equation, with a known solution (SPIEGEL *et al.*, 2009) given by:

$$F(\xi) = B_1 J_0(\lambda \xi) + B_2 Y_0(\lambda \xi) \quad (4.68)$$

where B_1 and B_2 are constants and J_0 and Y_0 are Bessel functions of the first and second kind, respectively, both order zero.

By differentiating Eq. (4.68) and applying the boundary condition *B. C. 1*, one obtains:

$$B_2 = -B_1 \frac{J_1(\lambda \xi_2)}{Y_1(\lambda \xi_2)} \quad (4.69)$$

which defines B_2 as a function of B_1 . By defining a new constant, B_3 , as in:

$$B_3 = \frac{B_1}{Y_1(\lambda \xi_2)} \quad (4.70)$$

the solution can be rewritten as:

$$F(\xi) = B_3 \frac{[Y_1(\lambda \xi_2) J_0(\lambda \xi) - J_1(\lambda \xi_2) Y_0(\lambda \xi)]}{\phi_0(\lambda \xi)} \quad (4.71)$$

where the expression in brackets can be expressed as a combined Bessel function of order zero, $\phi_0(\lambda\xi)$.

The differentiation of Eq. (4.71) and application of *B. C. 2* leads to:

$$\begin{aligned} -B_3\lambda \underbrace{[Y_1(\lambda\xi_2)J_1(\lambda\xi_1) - J_1(\lambda\xi_2)Y_1(\lambda\xi_1)]}_{\phi_1(\lambda\xi_1)} &= \\ &= Bi \cdot B_3 \underbrace{[Y_1(\lambda\xi_2)J_0(\lambda\xi_1) - J_1(\lambda\xi_2)Y_0(\lambda\xi_1)]}_{\phi_0(\lambda\xi_1)} \end{aligned} \quad (4.72)$$

where the differentiation of $\phi_0(\lambda\xi)$ resulted in the expression in brackets on the left-hand side of the equation, which was expressed as a combined Bessel function of order one, $\phi_1(\lambda\xi)$. Rewriting Eq.(4.72) as:

$$\phi_1(\lambda_n\xi_1) = \frac{Bi}{\lambda_n} \phi_0(\lambda_n\xi_1) \quad (4.73)$$

the only unknown variable that remains is λ , so that it can be obtained as any value that satisfies this equation. Due to the nature of Bessel functions, the solution for λ is a series of n values, λ_n , called eigenvalues. Therefore, the solution for $F(\xi)$ is also a series, as seen in:

$$F(\varepsilon) = \sum_{n=1}^{\infty} B_n \phi_0(\lambda_n\xi) \quad (4.74)$$

where the constant B_3 also becomes a series of constants B_n , which are still unknown. Therefore, all that remains to be defined is the series of constants, B_n , using the initial condition, I.C.. The solution is given by:

$$\sum_{n=1}^{\infty} B_n \phi_0(\lambda_n\xi) = R_x \ln\left(\frac{\xi}{\xi_1}\right) + 1 \quad (4.75)$$

So that the definition of B_n is then given by:

$$B_n = \frac{2[R_x \phi_0(\lambda_n \xi_2) + (\xi_1 Bi - R_x) \phi_0(\lambda_n \xi)]}{[\lambda_n \xi_2 \phi_0(\lambda_n \xi_2)]^2 - [\xi_1 \phi_0(\lambda_n \xi_1)]^2 (\lambda_n^2 + Bi^2)} \quad (4.76)$$

Finally, all relevant terms are defined for the dimensionless solution to the 1D transient heat conduction problem: the transient solution from Eq. (4.67), the spatial solution from Eq. (4.74) and the definition for the constant B_n in Eq. (4.76). Therefore, the overall solution to the 1D problem is given as:

$$\theta(\xi, Fo) = \sum_{n=1}^{\infty} B_n \phi_0(\lambda_n \xi) \exp(-\lambda_n^2 Fo) \quad (4.77)$$

4.3 MODELS FOR TRANSIENT STATE: CRITICAL LATENT HEAT OF SOLIDIFICATION

In this section, an analytical model is proposed for transient cooling, specifically in the latent cooling regime (B), as defined in Section 3.2.2. The model is based on the assumption that the critical solidified layer of PCM, which was experimentally observed (Section 5.1.2), corresponds to the peak of heat transfer efficiency from the PCM's latent heat to the thermal process. The assumption considers that the latent heat released by the solidifying PCM must flow through this layer in order to reach the evaporator of the thermosyphon, and therefore has to overcome a conduction thermal resistance, which increases as the solidified layer grows, until it becomes a big hindrance for the heat transfer to the thermosyphon, and operation cannot be maintained as desired.

4.3.1 CRITERION FOR THE CRITICAL SOLIDIFICATION REGIME

The first step of this analysis is to define a criterion for the beginning and the end of this critical latent period, so that its duration could be calculated. The expected thermal behavior in transient cooling is the temperatures of the PCM, T_{PCM} , and of the evaporator, T_e , to drop continuously until the PCM's solidification point is reached at the evaporator wall, that is, $T_e = T_m$. Then, a period of constant T_e is expected, while the PCM immediately adjacent to the evaporator continues to solidify. After this moment, both temperatures should drop once again

for as long as the power supply is off. In this case, the beginning criterion for the critical latent period would be the moment when $T_e = T_{PCM}$, and the end criterion would be the moment when T_e drops once again. However, this expected behavior did not occur in the experimental results, and a different criterion was chosen.

The actual experimental results, that will be seen and discussed in detail in Section 5.2.3, showed a different behavior for transient cooling. First, T_{PCM} and T_e drop continuously, as expected. However, this drop continues until T_e reached a certain value $T_{e,0}$, which was different for every test and ranged from $73 < T_{e,0} < 78$ °C. Then, after the moment when $T_{e,0}$ is reached, there is a sudden rise in T_e , until it reaches a peak ($T_{e,peak}$), followed by a similar rise and peak for all temperature readings along the thermosyphon. After this peak, all temperature readings suffered a slow, gradual decrease, which accelerated as phase change reached its end.

Therefore, the initial assumption for the beginning criterion of critical latent cooling was the moment when $T_e = T_{e,0}$. However, since this value varied considerably from test to test, it was considered unreliable as both the beginning and the endpoint criteria, and a more reliable pattern is needed. Since the analytical models thus far have been based on thermal resistances, this analysis began by studying the transient behavior of the evaporator and the PCM experimental resistances, obtained respectively as:

$$R_e = \frac{T_e - T_a}{\dot{q}} \quad (4.78)$$

$$R_{PCM} = \frac{T_{PCM} - T_e}{\dot{q}} \quad (4.79)$$

$$\dot{q} = h_\infty A_c (T_c - T_\infty) \quad (4.80)$$

Before the beginning of solidification, the PCM resistance is significantly larger than the evaporator resistance, that is, $R_{PCM} \gg R_e$, due to the difference in heat transfer mechanisms inside each component. The PCM transfers heat mainly through natural convection, which is much less effective than the evaporator's heat transfer via latent heat, associated with phase change. However, once the PCM begins to solidify, its predominant form of heat transfer becomes phase change as well, so that R_{PCM} reduces abruptly and reaches the same order of

magnitude as R_e . Indeed, the experimental results in Section 5.2.3 show that immediately after the beginning of solidification, R_{PCM} is slightly lower than R_e . Then, as the solid PCM layer forms and grows over the evaporator surface, the predominant form of heat transfer from PCM to evaporator becomes conduction through the solid layer, and R_{PCM} increases until $R_{PCM} \gg R_e$ once again. Therefore, this pattern suggests there must be a critical value for the ratio between the PCM and the evaporator resistances that signals the beginning and end of the peak heat transfer efficiency from the PCM, or the critical solidification period. This ratio, η , is defined as:

$$\eta = \frac{R_{PCM}}{R_e} \quad (4.81)$$

Indeed, a detailed analysis of the experimental values for parameter η , presented in Section 5.2.3 a), revealed the existence of a critical value, η_{cr} , which intersects the early stage of solidification for all tests. This critical value was assumed as the beginning and end criterion for the critical solidification regime.

4.3.2 SEMI-EMPIRICAL CORRELATION FOR THE DURATION OF CRITICAL LATENT HEAT TRANSFER

Once the criterion was defined for the duration of the critical solidification period, Δt_{cr} , the experimental data for Δt_{cr} was compiled and expressed in dimensionless form as Fo_{cr} , defined by:

$$Fo_{cr} = \frac{\Delta t_{cr} \alpha_s}{L_c^2} \quad (4.82)$$

This definition is based on the same L_c as the Fourier number used in Section 4.2.2 (Eq. (4.57)), since the relevant geometry was the same, but with the solid diffusivity of naphthalene, α_s , used instead of α_{eff} , since the present analysis refers to heat transfer through a solid layer, whereas the effective diffusivity of the previous section was relative to the convection heat transfer in the liquid pool. Similarly, a Biot number was defined for this analysis, Bi_s , as:

$$Bi_s = \frac{h_{eq}L_c}{k_s} \quad (4.83)$$

which differs from the definition given in the previous section (Eq. (4.54)) only by the replacement of effective conductivity k_{eff} for k_s , the conductivity of solid naphthalene.

In order to predict the duration of the critical latent period based on known experimental parameters, a dimensionless analysis of Bi_s vs. Fo_{cr} was performed and presented in Section 5.2.3. A relationship was observed between Bi_s and Fo_{cr} , which is given by:

$$Fo_{cr} = \frac{C_0}{Bi_s} \quad (4.84)$$

where the adjustment of the expressions to the experimental data resulted in the constant $C_0 = 0,2545$.

Additionally, a correlation to estimate the thickness of the PCM's critical solidified layer, δ_{cr} , was desired. By considering the initial assumption of this analysis, that this critical layer is formed on the surface of the evaporator, a new critical diameter variable was defined, D_{cr} , as presented by:

$$D_{cr} = d_o + \delta_c \quad (4.85)$$

which associates the critical thickness to the evaporator diameter. Then, a critical characteristic length, L_{cc} , was defined as:

$$L_{cc} = \sqrt{D_{cr}^2 - d_e^2} \quad (4.86)$$

It is therefore associated with the volume of solidified PCM during the critical period, V_{cr} , rather than the total volume of the PCM container. Once V_{cr} is obtained from:

$$V_{cr} = \frac{\pi l_e L_{cc}^2}{4} \quad (4.87)$$

then the critical mass, m_{cr} , is obtained as in:

$$m_{cr} = \rho_s V_{cr} \quad (4.88)$$

Next, the average heat transfer rate provided to the system over the critical latent period, $\dot{q}_{l,cr}$, is defined by:

$$\dot{q}_{l,cr} = \frac{m_{cr} h_{sl}}{\Delta t_{cr}} \quad (4.89)$$

Another form of obtaining the average heat transfer rate, $\dot{q}_{l,c}$, is to assume the average evaporator temperature during this period to be equal to the solidification point of the PCM, that is $T_{e,cr} = T_m$, and use the heat transfer coefficient already presented in previous sections, as it can be seen in:

$$\dot{q}_{l,cr} = h_{eq} A_e (T_m - T_\infty) \quad (4.90)$$

Combining Eq. (4.90) with Eqs. (4.87) – (4.89) results in:

$$L_{cc}^2 = \frac{\Delta t_{cr} 4d_e h_{eq} (T_m - T_\infty)}{h_{sl} \rho_s} \quad (4.91)$$

where Δt_{cr} can be obtained from the semi-empirical correlation of Eq. (4.84) combined with the definition given by Eq. (4.82), so that all variables are known and the critical characteristic length L_{cc} can be obtained.

4.3.3 LATENT HEAT EFFECTIVENESS

The desired outcome of latent heat storage is to provide a stable heat transfer rate to the thermal process, at a near constant temperature, during the liquid-solid phase change of the PCM. However, as observed throughout the study, this goal is only achieved during the critical latent heat period, which is shorter than the time required for complete solidification. This means that not all of the latent heat stored in the PCM is available to the thermal process as desired. In this section, a comparison between total and critical latent heat is made, and a correlation for the PCM's latent heat effectiveness is proposed.

The first step was to obtain the latent heat energy provided by the PCM during the critical period, $E_{l,cr}$, defined as:

$$E_{l,c} = m_{cr}h_{sl} \quad (4.92)$$

where m_c is given by combining Eq. (4.87) and Eq. (4.88), resulting in:

$$m_{cr} = \frac{\rho_s \pi l_e L_{cc}^2}{4} \quad (4.93)$$

Then, the latent heat present in the total volume of PCM, $E_{l,total}$, is given by:

$$E_{l,total} = m_{total}h_{sl} \quad (4.94)$$

where m_{total} is given by:

$$m_{total} = \frac{\rho_s \pi l_e L_c^2}{4} \quad (4.95)$$

with L_c given by Eq. (4.55). The ratio between these two values represents the effectiveness of the PCM's latent heat storage, since it expresses the fraction of energy stored that is actually available to the thermal process. This effectiveness is named ψ_{PCM} , and is defined as:

$$\psi = \frac{E_{l,cr}}{E_{l,total}} = \left(\frac{L_{cc}}{L_c}\right)^2 \quad (4.96)$$

which also shows that ψ_{PCM} is a function of both the critical characteristic length, L_{cc} , and the total PCM characteristic length, L_c .

A dimensionless correlation for effectiveness can be obtained by rewriting the definition of L_{cc} , Eq. (4.91), as a function of the dimensionless duration of the critical period, Fo_{cr} , defined in Eq. (4.82), as shown by:

$$L_{cc}^2 = \underbrace{\left(\frac{Fo_{cr} L_c^2}{\alpha_s} \right)}_{\Delta t_{cr}} \frac{4d_o h_{eq} (T_m - T_\infty)}{h_{sl} \rho_s} \quad (4.97)$$

This expression was then rewritten as:

$$\underbrace{\left(\frac{L_{cc}}{L_c} \right)^2}_{\psi_{PCM}} = Fo_{cr} \underbrace{\left(\frac{\rho_s c_{p,s}}{k_s} \right)}_{\alpha_s^{-1}} \frac{4d_o h_{eq} (T_m - T_\infty)}{h_{sl} \rho_s} \quad (4.98)$$

where the term for effectiveness emerges on the left-hand side of the equation, while the definition of solid PCM diffusivity α_s is included in the right-hand side. The resulting expression is further rewritten as:

$$\psi_{PCM} = Fo_{cr} \underbrace{\left(\frac{4d_o h_{eq}}{k_s} \right)}_{Bi_d} \underbrace{\frac{c_{p,s} (T_m - T_\infty)}{h_{sl}}}_{\phi} \quad (4.99)$$

where two new dimensionless parameters are defined: Bi_d , a Biot number with the evaporator diameter d_o as the characteristic length; and ϕ , which correlates the PCM's heat capacity and latent heat with the system's overall temperature difference. Given that a semi-empiric correlation was obtained in the previous section for the parameter Fo_{cr} , Eq. (4.84), the effectiveness ψ_{PCM} can then be obtained from:

$$\psi_{PCM} = \frac{C_0 Bi_d \phi}{Bi_s} \quad (4.100)$$

Next, an experimental reference for the effectiveness, $\psi_{PCM,exp}$, was needed for comparison with the analytical model. This reference was defined based on the timespan of the critical latent period, as a ratio of the measured duration, $\Delta t_{cr,exp}$, versus the maximum estimated duration of the latent period, $\Delta t_{cr,max}$, as given by:

$$\psi_{PCM,exp} = \frac{\Delta t_{cr,exp}}{\Delta t_{cr,max}} \quad (4.101)$$

In this analysis, $\Delta t_{cr,exp}$ was obtained in the previous section using the resistance ratio criterion, η_{cr} , and $\Delta t_{cr,max}$ is estimated using the expression:

$$\Delta t_{cr,max} = \frac{E_{l,total}}{\dot{q}_{l,cr}} \quad (4.102)$$

as the ratio between the total latent energy $E_{l,total}$ and the average latent heat rate, $\dot{q}_{l,cr}$, obtained from Eq. (4.90). This effectively means that $\Delta t_{cr,max}$ represents the ideal desired outcome of latent heat storage, with all the stored energy being provided to the thermal process at a constant heat transfer rate, and at the constant phase change temperature T_m .

5. RESULTS AND DISCUSSIONS

This chapter presents and discusses the results obtained in this study, beginning with Section 5.1, with the results of the experimental study presented in Chapter 3; then Section 5.2 discusses the results of the analytical models presented in Chapter 4.

5.1 EXPERIMENTAL RESULTS

The following subsections show the results from each experiment described in Chapter 3, discussing and analyzing each case.

5.1.1 NUSSELT NUMBERS

As mentioned previously in Section 3.2.1, the aim of this set of experiments was to obtain a correlation for the heat transfer coefficient, h_{∞} , due to forced convection over the thermosyphon's condenser in the wind tunnel. With this coefficient, Eq. (3.2) could be used to obtain the heat transfer rate provided by the PCM during transient cooling.

The Nusselt numbers obtained experimentally were compared with those predicted by some of the established literature's correlations, such as Zukauskas (1972, apud INCROPERA *et al.*, 2008), seen in Eq. (3.4); Churchill and Bernstein (1977, apud INCROPERA *et al.*, 2008), seen in Eq. (3.5); and Sparrow (2004), seen in Eq. (3.6). The values obtained for Nusselt are plotted against Reynolds in Figure 5.1, which shows that the experimental data considerably diverges from the theoretical values predicted by the correlations from the established literature, with mean errors of $\varepsilon_{mean} = \pm 55\%$ for both the Zukauskas and the Sparrow correlations, and of $\varepsilon_{mean} = \pm 62\%$ for the Churchill and Bernstein correlation. This discrepancy can be attributed to the confined condition of the thermosyphon's condenser within the wind tunnel, which differs from the ideal condition of a cylinder under free cross flow that is assumed for those correlations. This confinement can be seen in Figure 5.2, which shows a close-up photograph of the condenser inside the wind tunnel, where small gaps can be seen between the top of the condenser and the inner diameter of the tunnel, and between the lower portion of the condenser and the tunnel walls. The confinement and the gaps both affect the air flow, which can account for the aforementioned discrepancy.

Therefore, the correlation seen in Eq. (3.8) was adjusted to the experimental data from tests A to I (Table 3.5) by applying the least squares method to an equation in the form of Zukauskas', Eq. (3.4). The relevant coefficients presented the values of $C_Z = 0,63$, $m = 0,59$ and $n = 0,37$, that is:

$$\overline{Nu}_{d,x} = 0,63 Re_d^{0,59} Pr^{0,37} \left(\frac{Pr}{Pr_c} \right)^{1/4} \quad (5.1)$$

The values of Nusselt obtained using Eq. (5.1) are also included in Figure 5.1, where it is seen that this experimental correlation closely agrees with the data. This agreement becomes clearer when observing Figure 5.3, which shows a scatter plot of the experimental data vs. the theoretical predictions for Nusselt number, where the solid line corresponds to a perfect match between experimental data and model predictions. The regions between dashed lines represents the error margins of $\varepsilon_{max} = \pm 5\%$.

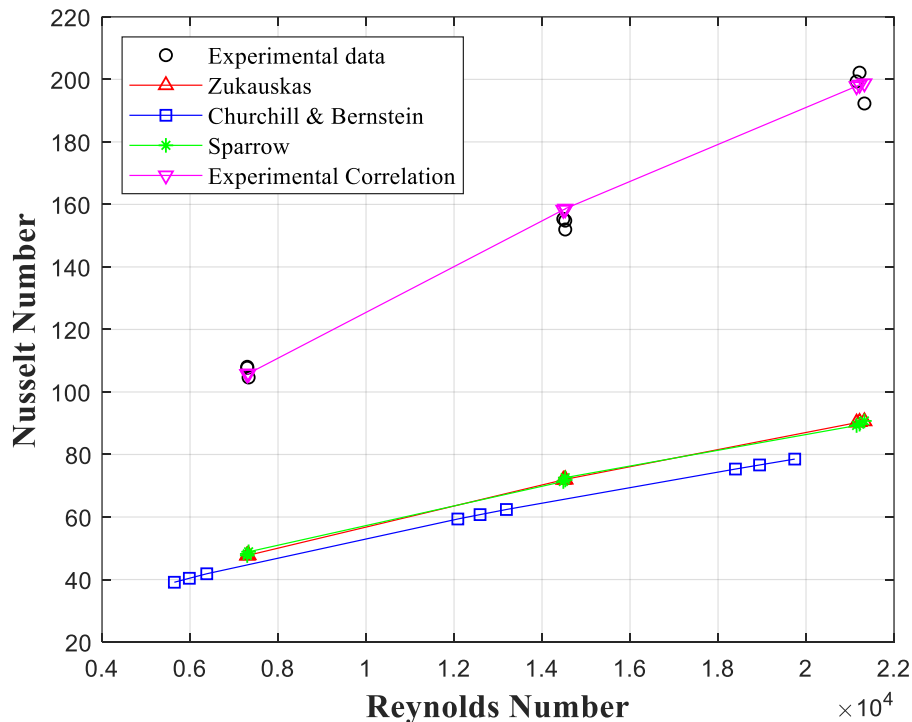


Figure 5.1. Nusselt versus Reynolds for tests A to I (Table 3.5), and comparison with three correlations from the literature, and one semi-empiric correlation proposed in this study.

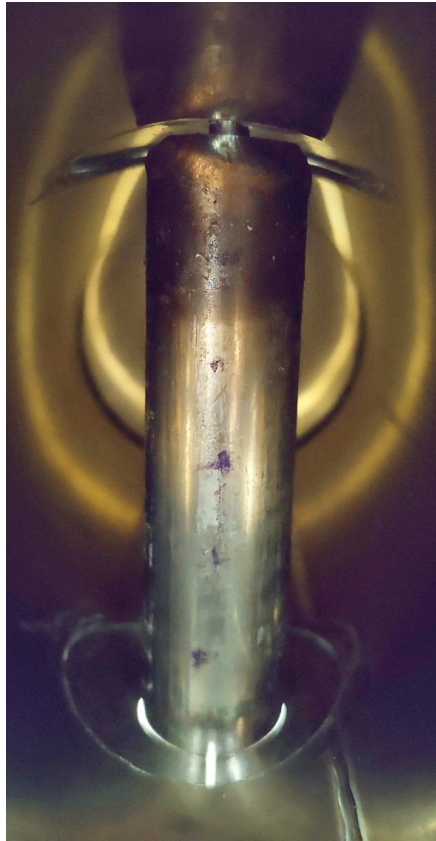


Figure 5.2. Close-up photo of the thermosyphon condenser confined inside the wind tunnel.

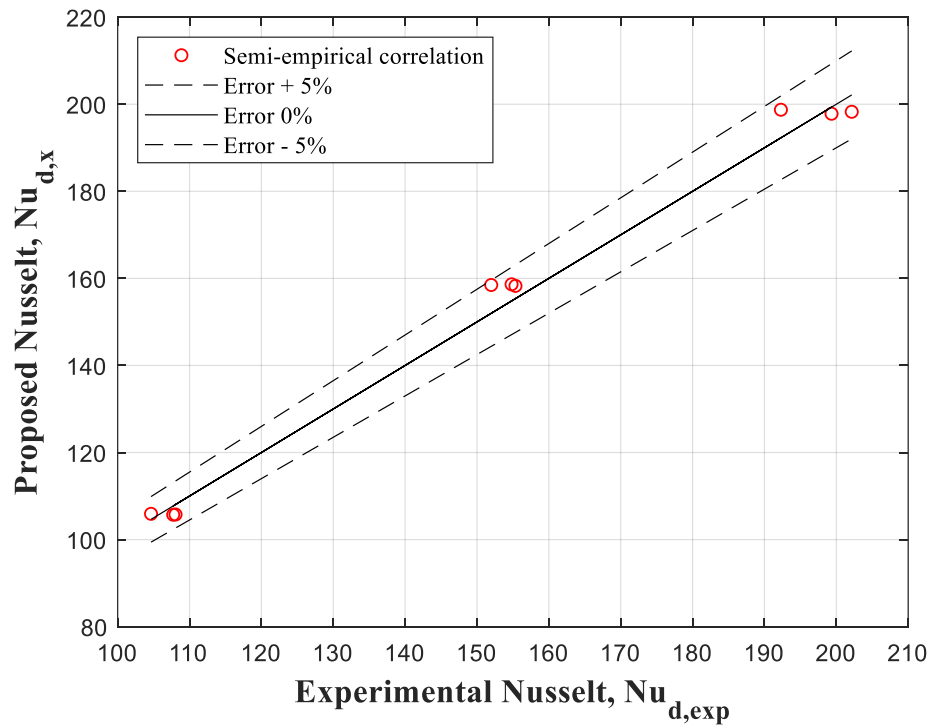


Figure 5.3. Scatter plot of the predicted versus experimental values of Nusselt number for tests A to I (Table 3.5), using the semi-empiric correlation.

In order to further validate the correlation proposed in Eq. (5.1), six new tests were devised and executed (J to O in Table 3.5), using different values of Re_d . Then, two previous tests (P and Q in Table 3.5) were incorporated into the study, where the thermosyphon had been inserted in a PCM reservoir for preliminary observations of PCM behavior. The results of all eight tests corroborate the previous assessment by also agreeing with the proposed model within a maximum error of $\varepsilon_{max} = \pm 5\%$, as seen in Figure 5.4.

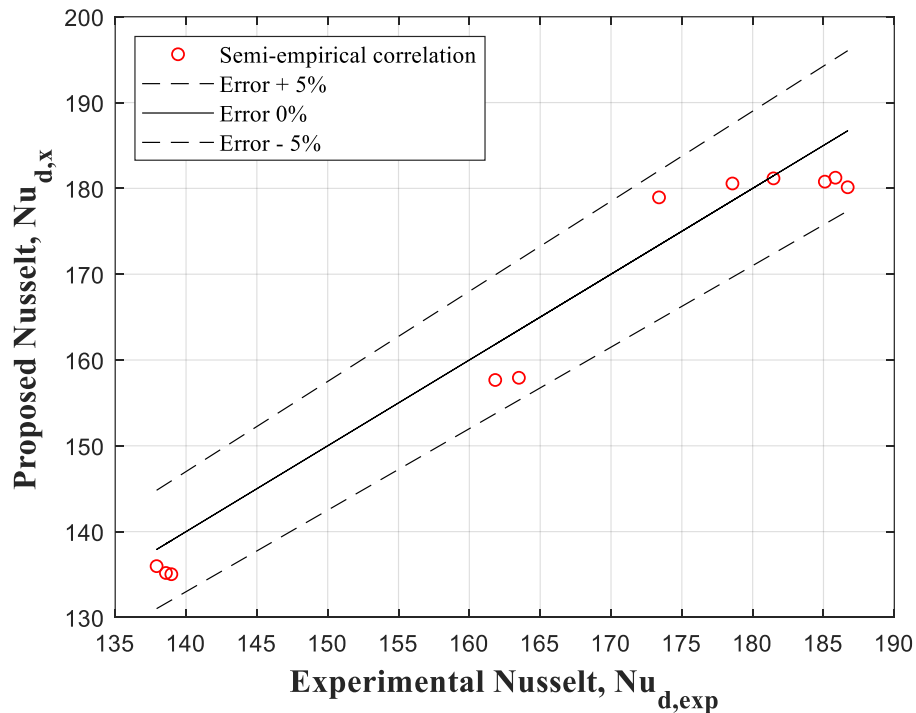


Figure 5.4. Scatter plot of the proposed versus experimental Nusselt numbers for tests J to Q (Table 3.5).

Therefore, it is concluded that the proposed semi-empirical correlation, Eq. (5.1), accurately predicts the experimental Nusselt number, and can be used to obtain the heat transfer correlation, h_{∞} , for future tests using Eq. (3.3), and the heat transfer rate \dot{q} using Eq. (3.2), valid for both steady state operation and transient regime during power oscillations in the experiments.

5.1.2 VISUALIZATION EXPERIMENT

The visualization experiment, described in Section 3.2.2, aimed to verify the initial assumption of this paper – that a critical solid layer of PCM was formed in the beginning of the solidification, coinciding with the peak heat transfer rate for the latent heat regime. This experiment corresponds to the tests listed as 1 to 6 on Table 3.4, which were all subjected to a steady state heat transfer rate input of $\dot{q}_{in} = 25$ W and cooled by natural convection. The results are shown and discussed in this section.

Starting with the largest container, PCM container A ($D_o = 2''$), Figure 5.5 shows the most relevant portion of test 1 (Table 3.4), in terms of average temperatures over time for all sections of the device, that is: the PCM container, T_{PCM} ; the evaporator, T_e ; the adiabatic section, T_a ; and the condenser, T_c . The system begins at steady state operation (1), with constant heat input $\dot{q}_{in} = 25$ W, and the temperatures for all sections constant and above the PCM's melting point ($T_m = 80.3$ °C) to ensure that it was fully melted. Then, the power supply is cut off, ($\dot{q}_{in} = 0$), and all temperatures drop abruptly (2), marking the start of the transient cooling regime. Once the evaporator temperature T_e reaches a certain point $T_{e,0}$ (3), it rises suddenly and spontaneously, that is, without any added external input. This moment is considered to mark the start of the PCM's solidification, since this phenomenon releases latent heat suddenly to the evaporator. Then, the temperatures of the other sections follow suit and begin to rise as well, until they reach a peak, $T_{e,peak}$, (4) and begin to drop once again. As the temperatures drop, T_e returns to $T_{e,0}$ (5) and continues to decrease. The power supply is only restored after the highest thermocouple on the PCM container wall reaches 70 °C (6), marking the end of the transient cooling regime. This temperature was chosen because it is 10 °C lower than $T_m = 80.3$ °C, ensuring that all the PCM had solidified, and the system could be studied while operating under a pure solid sensible cooling regime. The start-up before (1) and after (6) was not relevant to the goal of this study, and was therefore removed from the figure.

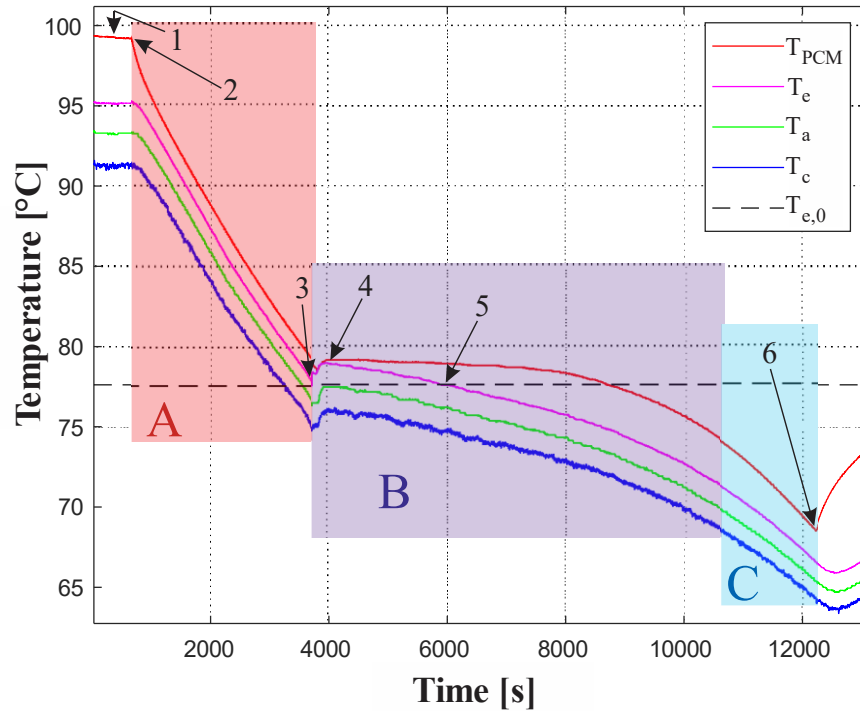


Figure 5.5. Temperature variation with time for Test 1 (Table 3.4), using PCM container A: (1) steady state; (2) power supply shut down; (3) beginning of the critical solidification period, at $T_e = T_{e,0}$; (4) peak latent heat rate; (5) end of critical solidification period, at $T_e = T_{e,0}$; (6) power supply restored. Interval (A), in red, marks the liquid sensible cooling regime; interval (B) in purple stands for latent cooling; and interval (C) in blue represents the solid sensible cooling regime.

The critical solidification period is defined experimentally, beginning at point (3), where evaporator temperature $T_e = T_{e,0}$, and extending until T_e drops below $T_{e,0}$ once again (5). As discussed in Section 3.1.3, the heat transfer rate to the heat sink, \dot{q}_{out} , is largely dependent on the condenser wall temperature, T_c , which follows T_e . Therefore, the critical solidification period corresponds to a critical heat transfer rate \dot{q}_{out} .

It is worth noting that the peak temperature value remained approximately constant, with $T_{e,peak} = (78.6 \pm 0.3)^\circ\text{C}$ for all four tests. This value is close to the known solidification point of naphthalene, $T_m = 80.3^\circ\text{C}$, so it was considered that the PCM immediately adjacent to the evaporator wall at that moment was likely at $T = T_m$. In contrast, the evaporator temperature at the beginning of solidification, $T_{e,0}$, suffered larger variations from $74 < T_{e,0} < 78^\circ\text{C}$. This is unexpected, since those values are significantly lower than $T_m = 80.3^\circ\text{C}$. This means that the evaporator wall reaches significantly lower values than the solidification point before any phase change can be noticed in the system, which suggests that the naphthalene immediately adjacent to the evaporator remained liquid below its freezing point. This phenomenon is consistent with observations from the literature, and is called supercooling (MACHIDA *et al.*, 2021). In this state the system is considered to be metastable, since freezing

can begin suddenly as soon as solid crystals begin to form and spread in the liquid pool, around nucleation sites (PRUPPACHER; KLETT, 2010). These nucleation sites can be imperfections on the heat transfer surface, or impurities in the liquid pool, for instance, which are unpredictable and difficult to control.

As discussed in Section 3.2.2, three separate regimes were expected during the transient cooling period: (A) liquid sensible cooling, where the material is entirely in liquid phase and temperatures decrease until the PCM reaches its melting point; (B) latent cooling, where the material undergoes liquid-solid phase change, releasing latent heat onto the thermosyphon; and (C) solid sensible cooling, where the PCM is solid and temperatures decrease once more, releasing sensible heat onto the thermosyphon. These regimes were indeed observed in the experimental results, as shown in Figure 5.5, marked as differently colored regions. The liquid sensible cooling (A) is shown in red, spanning from point (2) to point (3). Then, the latent cooling (B) is shown in purple, extending from point (3) to an unspecified point beyond (5). Lastly the solid sensible cooling (C) is shown in blue, extending from the end of (B) to point (6). The exact limit between regimes (B) and (C) is difficult to pinpoint, as they are each represented by a different inclination of the system's temperature curves, and the shift in inclination happens gradually after point (5). This is consistent with the assumption that the solid layer of PCM surrounding the evaporator wall creates a thermal barrier, which reduces the overall heat rate and slows down the cooling process, so that the solidification of the outer regions of the PCM occurs simultaneously to the sensible cooling of the already solidified inner regions. For this test, the total timespan between point (2) and point (6), which represents the total duration of the transient cooling regime, was of $\Delta t_{total} = 11520$ s, as seen in Table 5.1.

Figure 5.6 shows the relevant portion of Test 2 (Table 3.4), in terms of average temperatures over time. The parameters for this test were similar to those of Test 1, with the thermosyphon also inserted into the 2" PCM container. However, Test 2 was interrupted due to the extraction of the thermosyphon in order to observe the formation of a critical solidified layer of PCM. Once again, the test is shown starting with the steady state (1), followed by a temperature drop due to shutting down the power supply (2), then the critical solidification period, spanning from the sudden temperature rise at $T_{e,0}$ (3), peak (4) until the return to $T_{e,0}$ (5) as expected from the results of Test 1. The duration of each phase was similar to the results of Test 1, as expected from two tests with the same device and under similar ambient conditions. However, at approximately the same time as point (5) was reached, the test was interrupted as the thermosyphon was quickly removed from the PCM container, in order to verify the

formation of a solid PCM layer during the critical period, as suggested in the literature (LUU *et al.*, 2020) and investigated in this study. Once this solid layer was observed, its thickness was also measured.

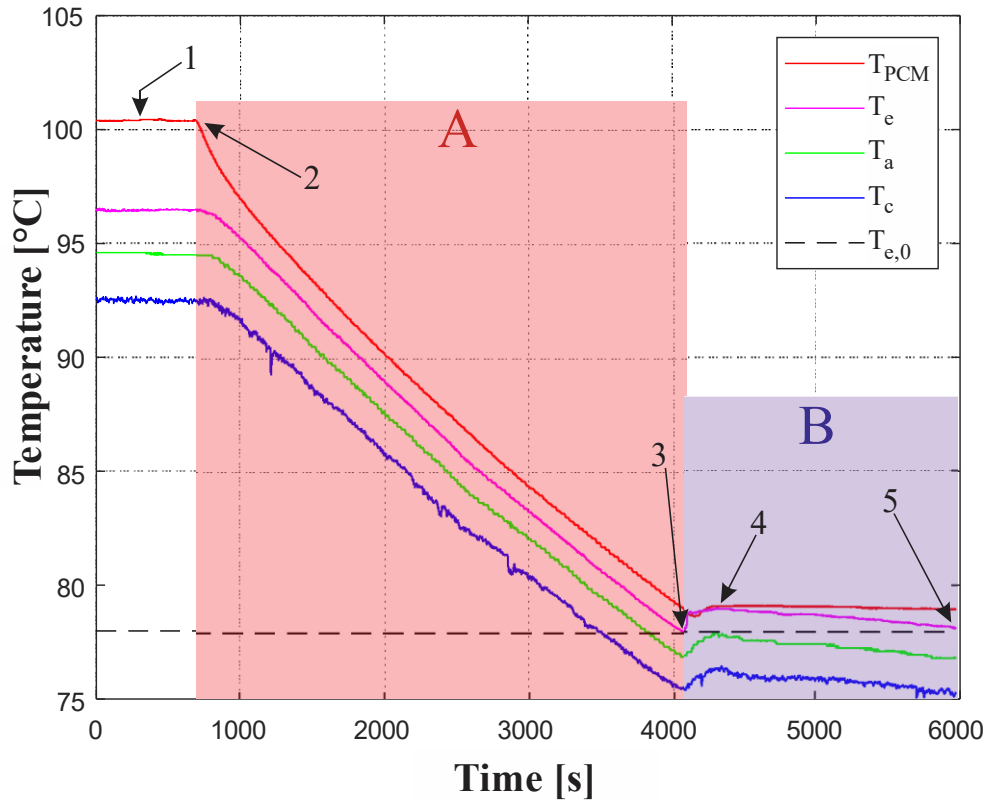


Figure 5.6. Temperature variation with time for Test 2 (Table 3.4), using PCM container A and interrupted by removing the evaporator from the PCM. Interval (A), in red, marks the liquid sensible cooling regime; and interval (B) in purple stands for latent cooling. The solid sensible cooling regime is not present here, due to the extraction from the PCM.

Table 5.1 – Total duration of the transient cooling regime, Δt_c , for each PCM container used on the complete visualization tests (1, 3 and 5 on Table 3.4).

Test number	1	3	5
PCM container	A($D_o = 2''$)	B($D_o = 1\frac{1}{2}''$)	C($D_o = 1\frac{1}{4}''$)
Total duration of transient cooling regime, Δt_c [s]	11520	5002	3142

Figure 5.7 shows pictures of the thermosyphon's evaporator after being extracted from the PCM container A, demonstrating the formation of a solidified layer of naphthalene along the entire length of the evaporator, where it was immersed in the pool of PCM during the initial

moments of the latent period. The layer is somewhat uneven, with a thicker section near the 530 mm height, shown in Figure 5.7 as point (1), and tapering out towards the bottom end of the evaporator. A digital caliper was used to measure the external diameter of the solid layer along the evaporator length, for six points separated at 100 mm intervals, and making three measurements for each, to a total of eighteen measured points. Then, the average of these and the resulting PCM layer thickness (subtracting the evaporator diameter) were registered as $D_s = 30,8$ mm and $\delta_s = 2,7$ mm, respectively, as seen in Table 5.2. As expected, at the moment of extraction, there was still a considerable volume of liquid PCM in the container, suggesting that the critical solidification period observed in Figure 5.6 corresponded to a fraction of the total available latent heat in the PCM. This assessment can also be verified by calculating the PCM mass corresponding to this critical solid layer as:

$$m^* = \rho_s l_e \pi \frac{(D_s^2 - d_o^2)}{4} \quad (5.2)$$

where ρ_s is the solid density of naphthalene. The result of Eq. (5.2) for Test 2 was of $m^* = 0,164$ kg, which corresponded to a fraction of 23 % of the total PCM mass in container A, $m_{PCM,A} = 0,711$ kg, as given by Table 3.2. This information is also summarized in Table 5.2. This result agrees with the initial assumption of this study that there is indeed a critical heat rate at the beginning of the solidification, which ends once a solid PCM layer is formed around the evaporator wall and insulates it from the remaining thermal energy storage.

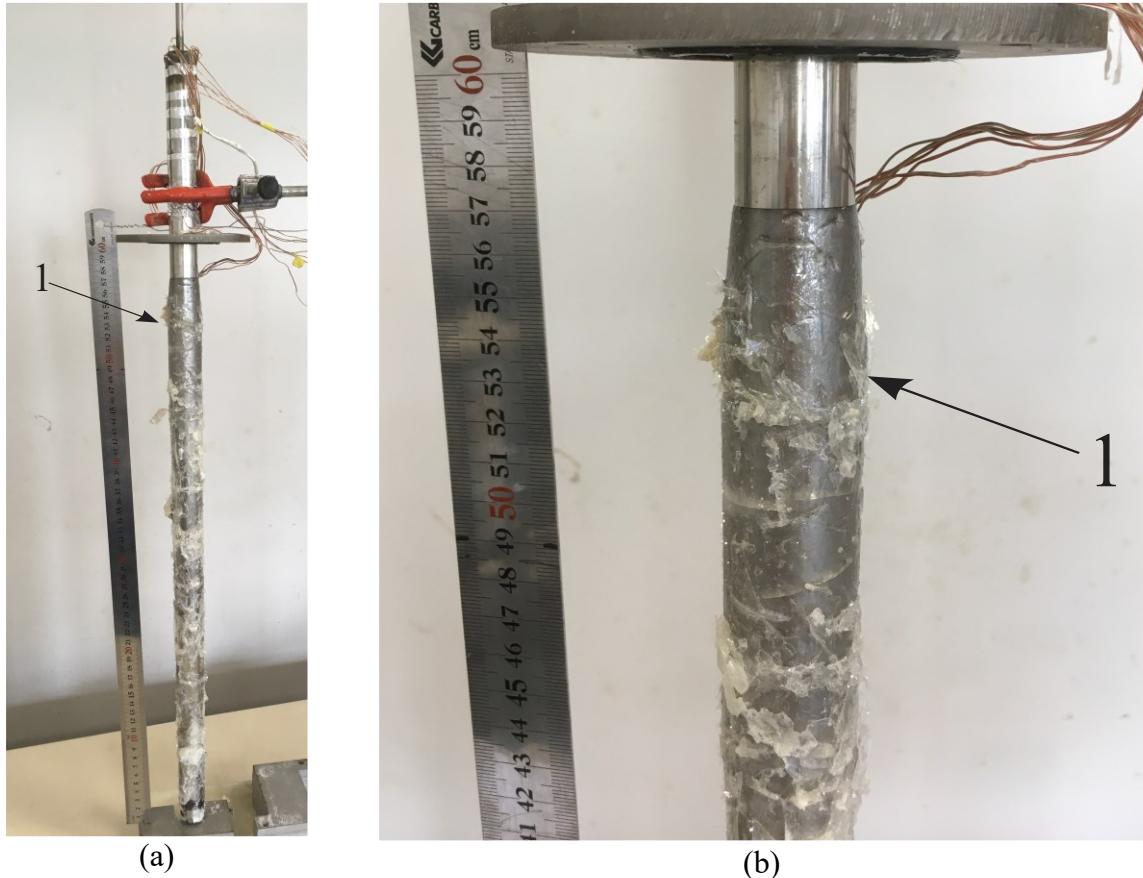


Figure 5.7. Pictures of the evaporator after removal from PCM container A ($D_o = 2''$), from Test 2 (Table 3.4): a) next to a steel ruler, for scale; b) close up near the top of the evaporator.

Table 5.2 – Average solid layer thickness, critical layer PCM mass and total PCM mass data for each interrupted test (2, 4 and 6 on Table 3.4).

PCM container	A ($D_o = 2''$)	B ($D_o = 1\ 1/2''$)	C ($D_o = 1\ 1/4''$)
Average solidified diameter, D_s [mm]:	30,8	28,6	29,3 ($D_s = D_i$)
Average solid layer thickness, δ_s [mm]:	2,7	1,6	1,9
PCM mass of the critical solidified layer, m^* [kg]	0,164	0,093	0,098
Total PCM mass, m_{PCM} [kg]	0,711	0,238	0,098
Mass fraction of the critical layer, m^*/m_{PCM}	23 %	39 %	100 %

The results of the visualization tests for the PCM container B ($D_e = 1\frac{1}{2}$ "") are shown in Figure 5.8 to Figure 5.10, corresponding to tests 3 and 4 (Table 3.4). Test 3 is similar to Test 1, showing the relevant sections of the full visualization test, while Test 4 is similar to Test 2, showing an interruption of the transient cooling period due to the thermosyphon's extraction from the PCM container, with the difference that tests 1 and 2 used the larger PCM container A ($D_o = 2$ ""). The same relevant points are labeled from (1) to (6), with the distinction that the duration of each cooling regime was shorter than those observed for the 2" PCM container, implying that as the PCM volume decreases, so does the total thermal energy stored and therefore the cooling period is shortened. For this test, the total timespan between point (2) and point (6), which represents the total duration of the transient cooling regime, was of $\Delta t_{total} = 5002$ s, less than half the value of Δt_{total} for Test 1, as seen in Table 5.1.

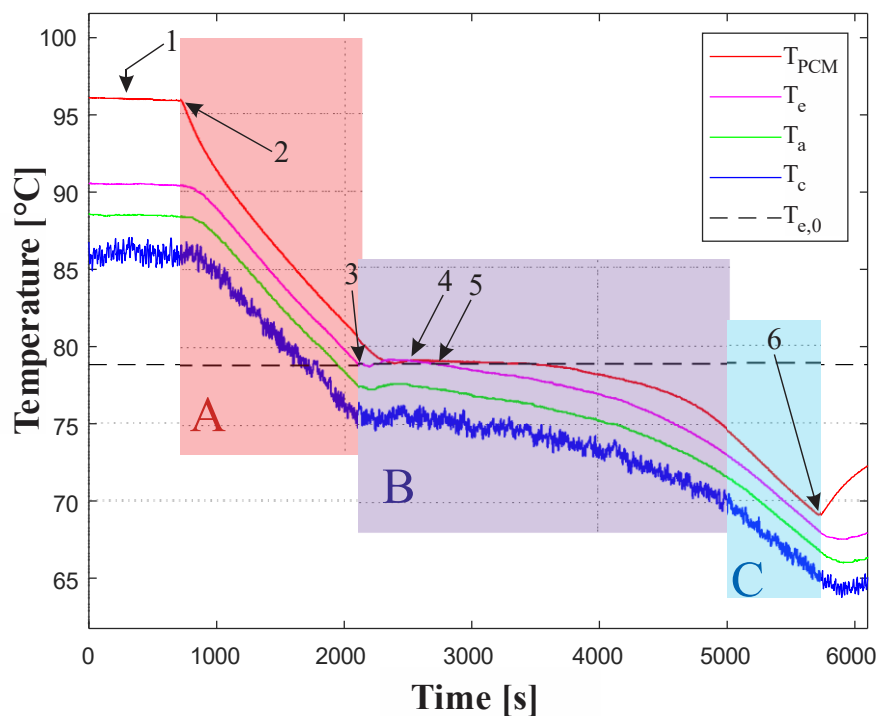


Figure 5.8. Temperature variations with time for Test 3 (Table 3.4), using PCM container B. Interval (A), in red, marks the liquid sensible cooling regime; interval (B) in purple stands for latent cooling; and interval (C) in blue represents the solid sensible cooling regime.

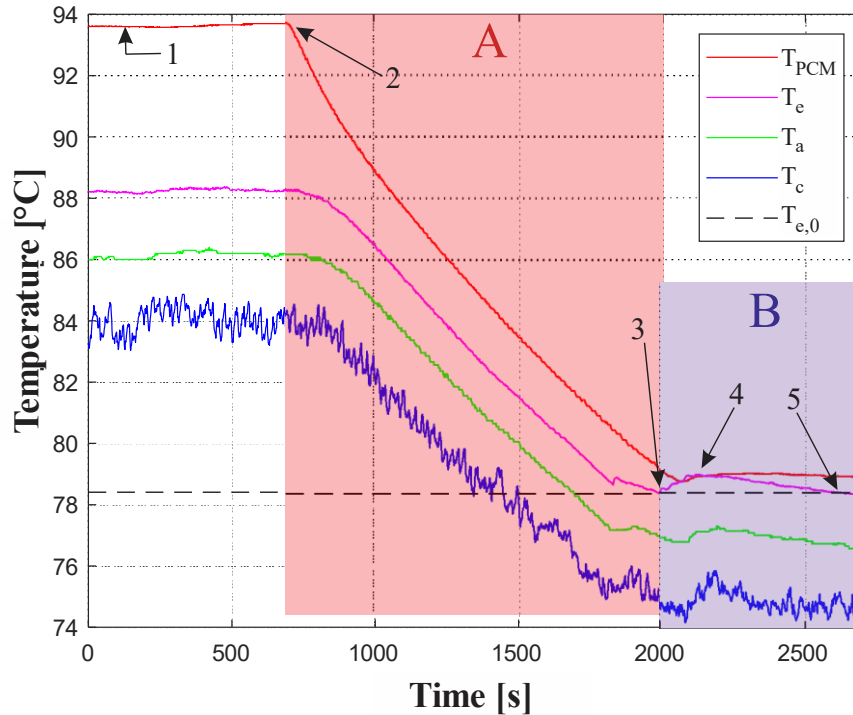


Figure 5.9. Temperature variations with time for Test 4 (Table 3.4), using PCM container B and interrupted by removing the evaporator from the PCM. Period (A), in red, marks the liquid sensible cooling regime; and interval (B) in purple stands for latent cooling. The solid sensible cooling regime is not present, due to the extraction.

Similarly to the previous case, the pictures of Figure 5.10 show the formation of a solidified layer of naphthalene along the entire length of the evaporator, immersed in the pool of PCM. The layer of this test was also somewhat uneven, with a thicker section near the 500 mm height, shown in Figure 5.10 as point (1), and tapering out towards the bottom end. Again, a digital caliper was used to measure the outer diameter of the solid layer along the evaporator length, with a total of eighteen measured points, with an average presented also on Table 5.2 as $D_s = 28.6$ mm, and the corresponding solid layer thickness calculated as $\delta_s = 1.6$ mm. As in the previous test with extraction, there was still a considerable volume of liquid PCM in the container, suggesting that the critical solidification period observed in Figure 5.9 corresponded to a fraction of the total available latent heat in the PCM, equivalent to the latent heat of the observed solid layer adhered to the evaporator. This assessment can also be verified by calculating the PCM mass of the critical solid layer, m^* from Eq. (5.2), which resulted in $m^* = 0,093$ kg, or 39 % of the total PCM mass in container B, $m_{PCM,B} = 0,238$ kg as given by Table 3.2. This information is also summarized in Table 5.2.

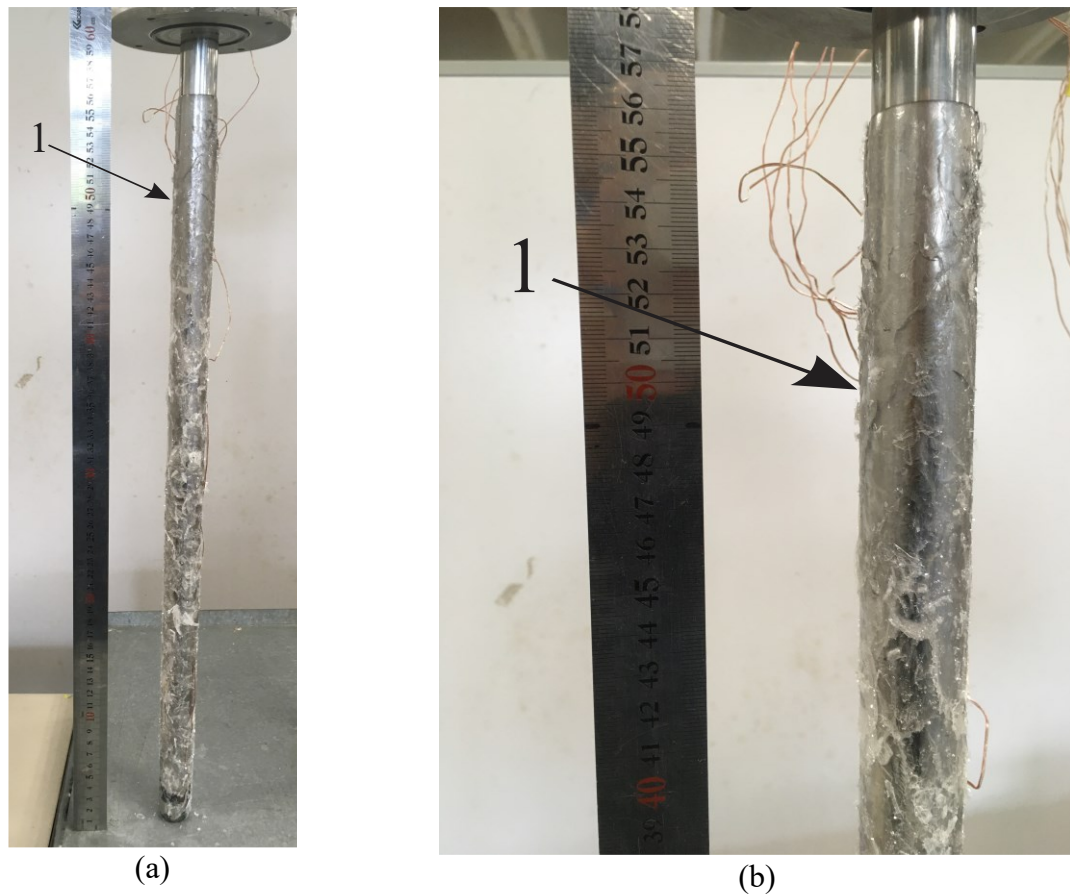


Figure 5.10. Pictures from the evaporator after removal from PCM container B ($D_o = 1\frac{1}{2}$ "), from Test 4 (Table 3.4): a) next to a steel ruler, for scale; b) close up near the top of the evaporator.

The results of the visualization tests for the smallest container, PCM container C ($D_o = 1\frac{1}{4}$ ") are shown in Figure 5.11 to Figure 5.13, corresponding to tests 5 and 6 from Table 3.4, which were similar to tests 1 and 2, respectively. The same relevant points are labeled from (1) to (6), with the duration of each cooling regime even shorter than those observed for the medium PCM container, confirming that as the PCM volume decreases, so does the total thermal energy stored and therefore the cooling period is shortened. For this test, the total timespan between point (2) and point (6), which represents the total duration of the transient cooling regime, was of $\Delta t_{total} = 3142$ s, just a little over a fourth of the value of Δt_{total} for Test 1, as seen in Table 5.1. Another distinction in these tests is that the peak (4) is less prominent, and the beginning of the solidification (3) less clear, with an observable oscillation of T_e before this point. This lack of clarity, combined with the shorter critical period for this PCM container impaired the accuracy of the evaporator removal on Test 6, seen in Figure 5.12.

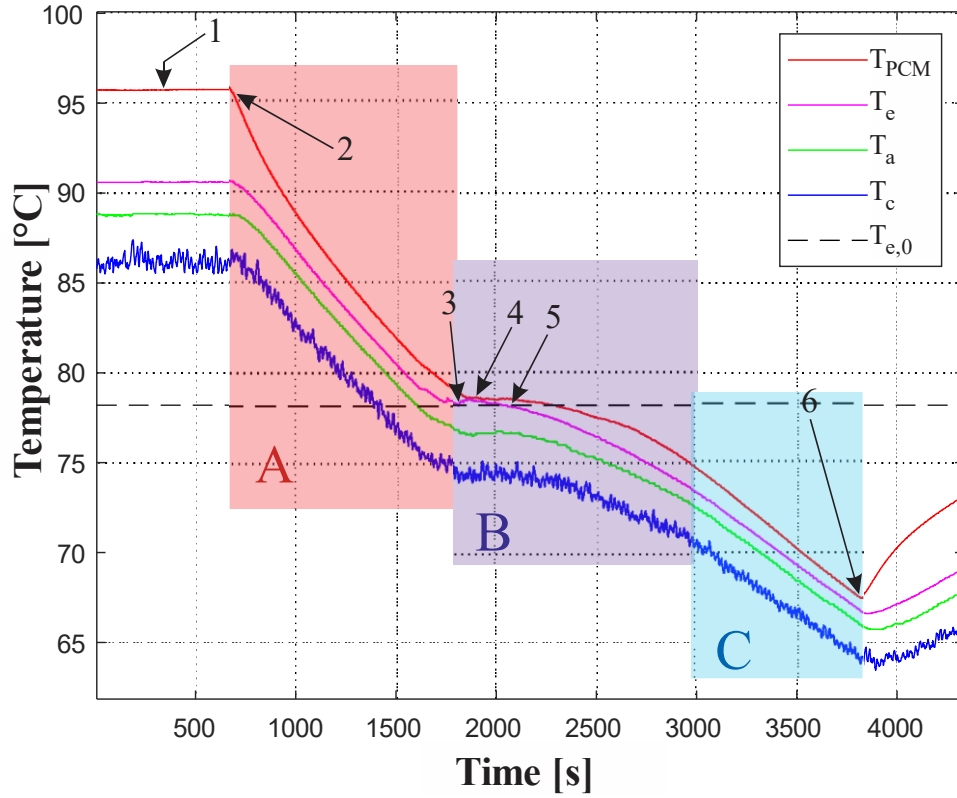


Figure 5.11. Temperature variations with time for Test 5 (Table 3.4).

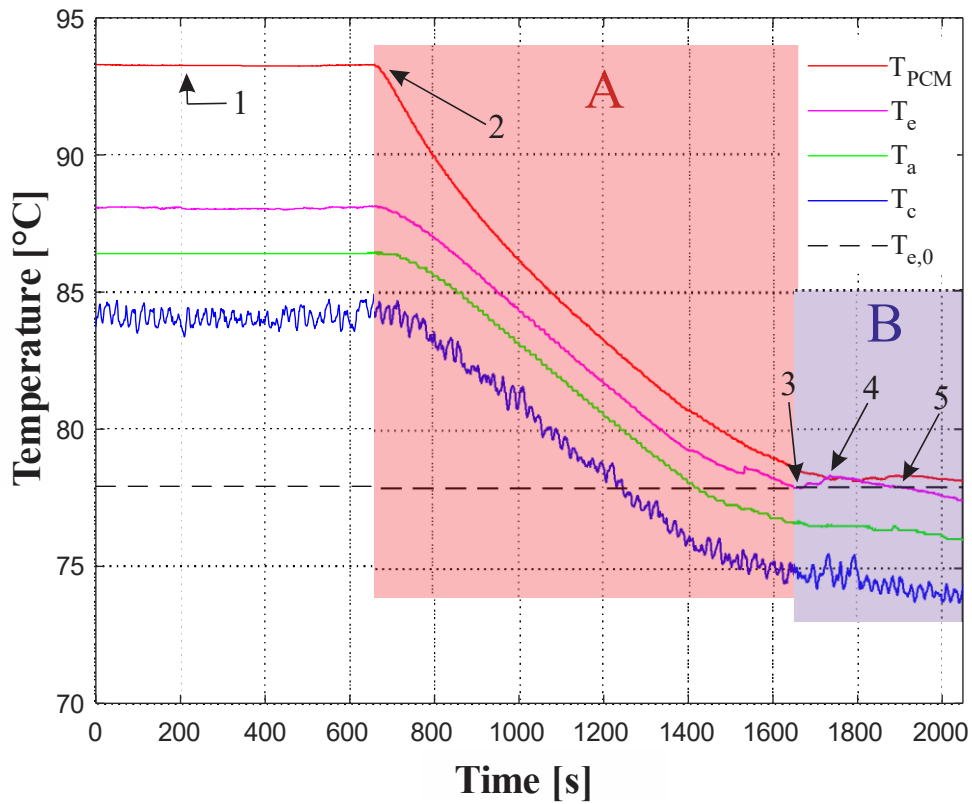


Figure 5.12. Temperature variations with time for Test 6 (Table 3.4), interrupted by removing the evaporator from the PCM.

At the time of removal of the evaporator from PCM container C, the material appeared to be entirely solidified. No liquid PCM pool was observed in the container, and the solidified layer over the evaporator was not intact, with several broken portions along its length, likely due to the forced removal. The picture of Figure 5.13 shows the measurement of one of the intact portions of solid naphthalene using a digital caliper. The measurement of $D_s = 28.9$ mm approaches the average inner diameter of the PCM container, $D_i = 29.4$ mm. Because the solid layer was broken, it was not possible to make more measurements as it was done in previous tests, so the average solid layer in Table 5.2 for this test was assumed equal to the inner diameter of the container, and the solidified layer was assumed to be the entire PCM volume.



Figure 5.13. Picture from the evaporator after removal from $1\frac{1}{4}$ " PCM container, from Test 6 (Table 3.4), with a digital caliper measuring the solidified layer thickness at one of the points where it was intact.

Therefore, the results of the visualization experiment confirmed the existence of a critical solidified layer, which forms over the heat transfer surface (in this case, the thermosyphon's evaporator) during a critical heat transfer period, after which it acts as a thermal barrier between the PCM's latent heat and the desired thermal process, as proposed by LUU *et al.* (2020). The confirmation of this hypothesis serves as the basis for the current investigation.

5.1.3 BASELINE EXPERIMENT

The results of the baseline experiment were used to observe the typical temperature oscillation expected from a thermosyphon subjected to interruptions from the heat source, and were used to evaluate the thermal resistance models used for the closed thermosyphon. This experiment was composed of tests 7 to 12 (Table 3.4). For the sake of brevity, only the first and last tests are shown in the current section – that is, Test 7 in Figure 5.14, which represents the lowest heat transfer rate input, $\dot{q}_{in} = 40$ W, and the lowest Nusselt number in the wind tunnel, with air velocity $v_{\infty} = 4.45$ m/s; and Test 12 in Figure 5.15, which represents the highest heat transfer $\dot{q}_{in} = 80$ W and $v_{\infty} = 12.93$ m/s. The remaining results are presented in APPENDIX B. In the next section, these results are compared to the main experiment in order to study the effect of the PCM container in the cooling regime.

The temperature variations with time presented in Figure 5.14 and Figure 5.15 show an initial steady-state operation (1), followed by a sudden drop (2) once the power supply is shut down. This temperature drop occurs at a constant rate, which is equal for all three sections of the thermosyphon, as evidenced by the parallel lines of T_e (evaporator), T_a (adiabatic section), and T_c (condenser). Then, after a time interval of $\Delta t = 600$ s, or ten minutes, the power supply was restored (3) and all temperatures began to rise until steady-state was reached once again (4). The temperature drop observed from (2) to (3) is consistent with the sensible cooling regime, as expected in Section 3.2.3. The total temperature drop was largest for Test 12 (Figure 5.15), with a condenser temperature difference of $\Delta T_c = 20$ °C. Test 7 (Figure 5.14) showed approximately $\Delta T_c = 15$ °C over the same time span. Since both tests used the same thermosyphon, with the same fill ratio, $F = 60$ %, this overall difference can be attributed to their distinct cooling conditions, due to the wind tunnel air velocities v_{∞} .

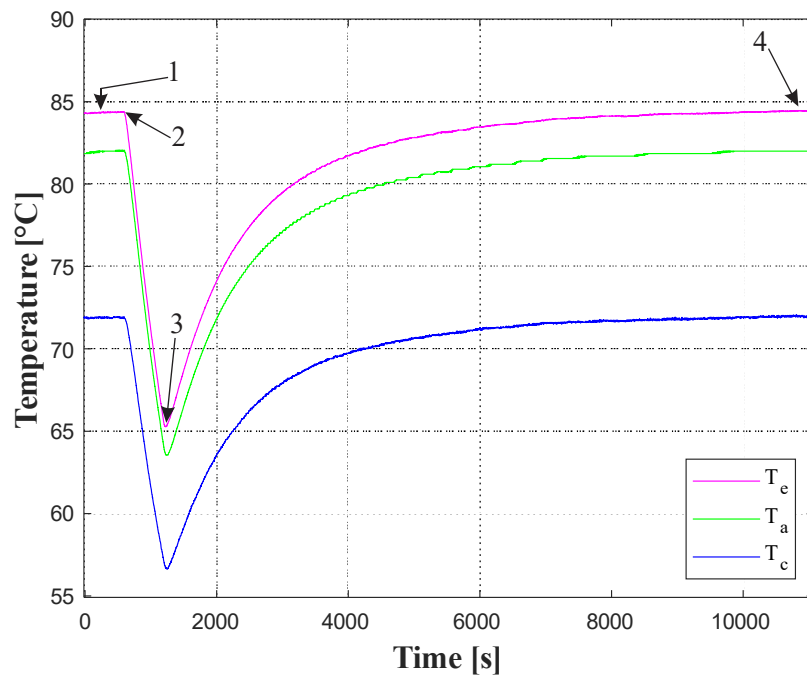


Figure 5.14. Temperature variations with time for Test 7 (Table 3.4), with heat inputs of $\dot{q}_{in} = 40$ W and $v_{\infty} = 4,45$ m/s.

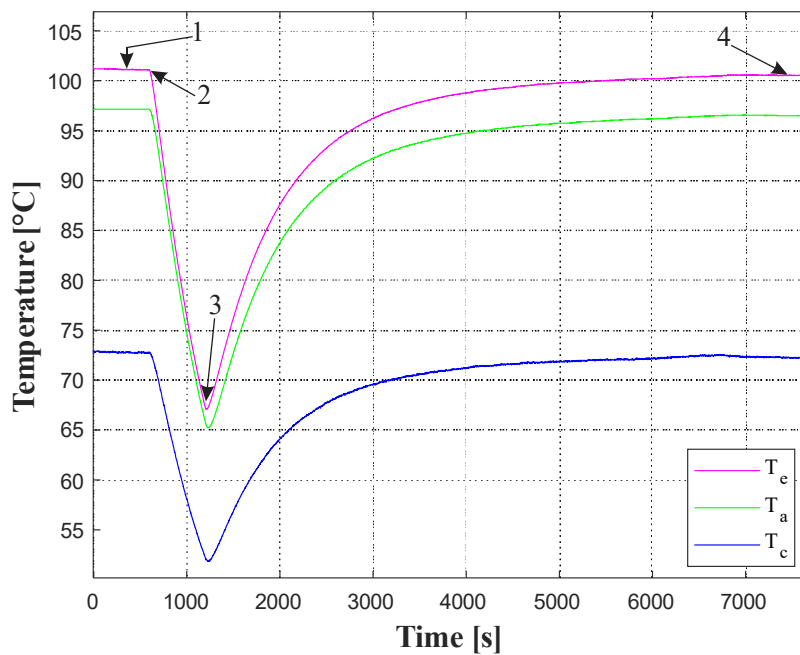


Figure 5.15. Temperature variations with time for Test 12 (Table 3.4), with heat inputs of $\dot{q}_{in} = 80$ W and $v_{\infty} = 12,93$ m/s

5.1.4 MAIN EXPERIMENT

The current section shows and discusses the results of the main experiment, described in Section 3.2.4. The results are shown as graphs of average temperature variation with time for every section of the system, that is, the evaporator (T_e), adiabatic section (T_a), and condenser

(T_c) of the thermosyphon, and the PCM container (T_{PCM}). The averages were calculated from the thermocouples placed according to Figure 3.8. Only the relevant time interval for each test is shown, as described by the six points of interest seen in Section 5.1.2. That is, the tests begin with the steady state (1). Then, there follows a temperature drop due to shutting down the power supply (2). After this, there is a sudden temperature rise at $T_{e,0}$ (3) due to the beginning of solidification on the PCM. This rise continues until a peak is reached (4) and then there is a temperature drop until T_e returns to $T_{e,0}$ (5). After, there is a continuous temperature decrease until all thermocouple readings on the PCM container wall reached 70°C , that is, all the PCM is considered to be in solid sensible cooling regime. At this point the power supply is restored (6) and temperatures begin to rise once again.

The main experiment was composed of tests 13 to 24 (Table 3.4), all cooled by forced convection in the wind tunnel. The thermosyphon was attached to PCM container A ($D_o = 2''$) for Tests 13 to 16, to PCM container B ($D_o = 1\frac{1}{2}''$) for tests 17 to 20, and to PCM container C ($D_o = 1\frac{1}{4}''$) for tests 21 to 24, in order to assess the effects of different PCM volumes and masses on the thermal behavior of the device. Every combination of thermosyphon and PCM container was also subjected to four wind tunnel velocities, v_∞ : 4,45 m/s, 6,83 m/s, 9,94 m/s, and 12,93 m/s. Every velocity was tested with a heat transfer rate input \dot{q}_{in} of: 50 W, 60 W, 70 W, and 80 W, respectively, as presented in Table 3.4.

The first and last tests (13 and 16 in Table 3.4) performed with PCM container A ($D_e = 2''$), are shown in Figure 5.16 and Figure 5.17, respectively. Similarly, the first and last tests (17 and 20 in Table 3.4) using PCM container B ($D_o = 1\frac{1}{2}''$), are shown in Figure 5.18 and Figure 5.19, respectively; and finally the first and last tests (21 and 24 in Table 3.4) using PCM container C ($D_o = 1\frac{1}{4}''$), are shown in Figure 5.20 and Figure 5.21, respectively. The first test of each pair corresponds to the lowest heat rate, $\dot{q}_{in} = 50$ W for that device, while the last test corresponds to the highest heat rate, $\dot{q}_{in} = 80$ W.

All tests showed similar behaviors of temperature variations with time, and the remaining tests (14, 15, 18, 19, 22, and 23 from Table 3.4.) can be seen in APPENDIX B.

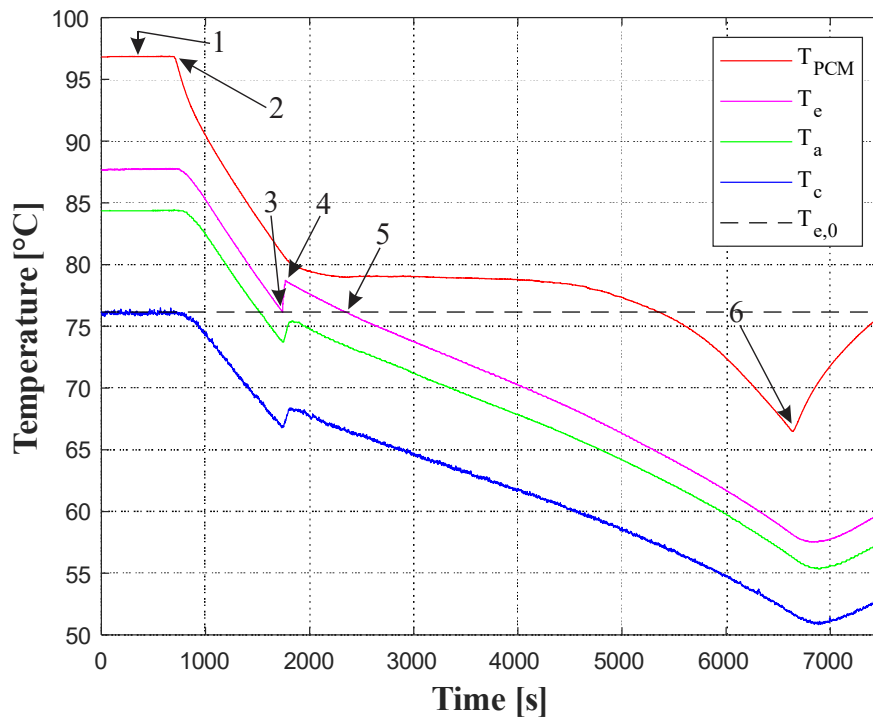


Figure 5.16. Temperature variations with time for Test 13 (Table 3.4), with $\dot{q}_{in} = 50$ W and $v_{\infty} = 4,45$ m/s.

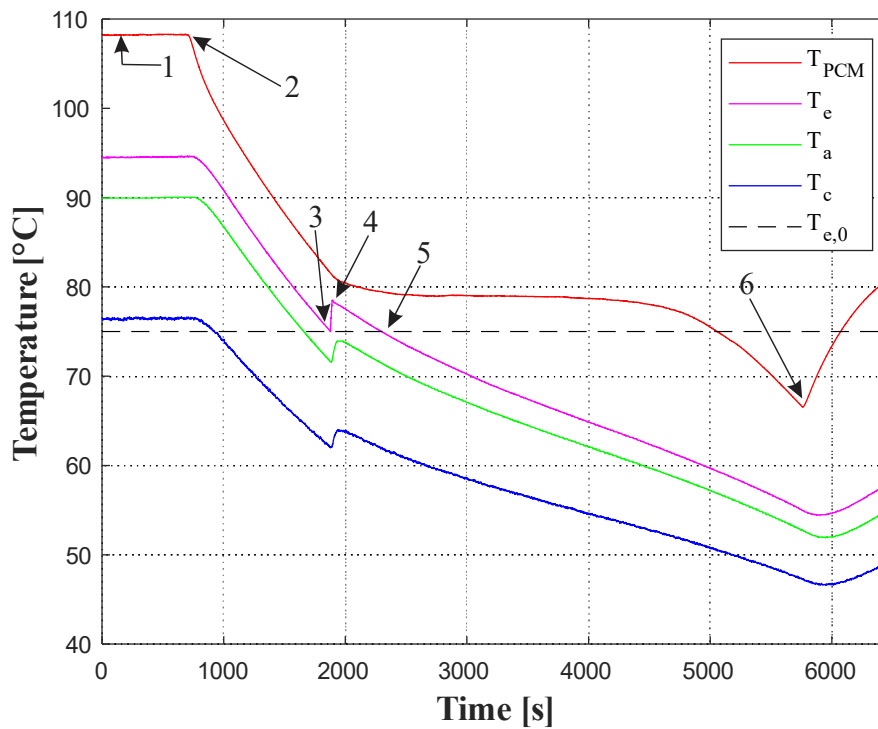


Figure 5.17. Temperature variations with time for Test 16 (Table 3.4), with $\dot{q}_{in} = 80$ W and $v_{\infty} = 12,93$ m/s.

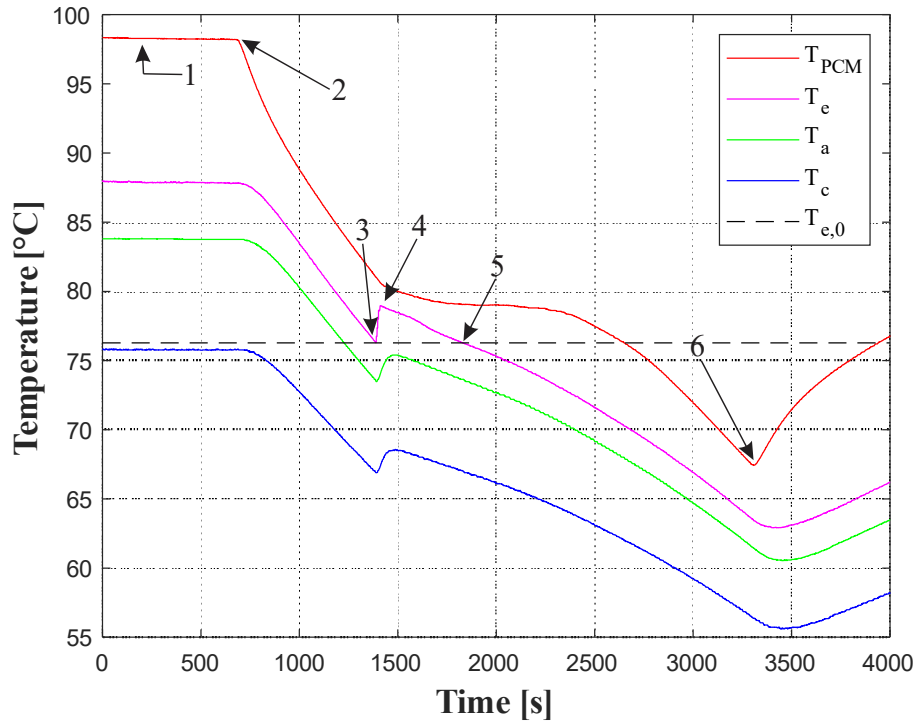


Figure 5.18. Temperature variations with time for Test 17 (Table 3.4), with $\dot{q}_{in} = 50$ W and $v_{\infty} = 4,45$ m/s.

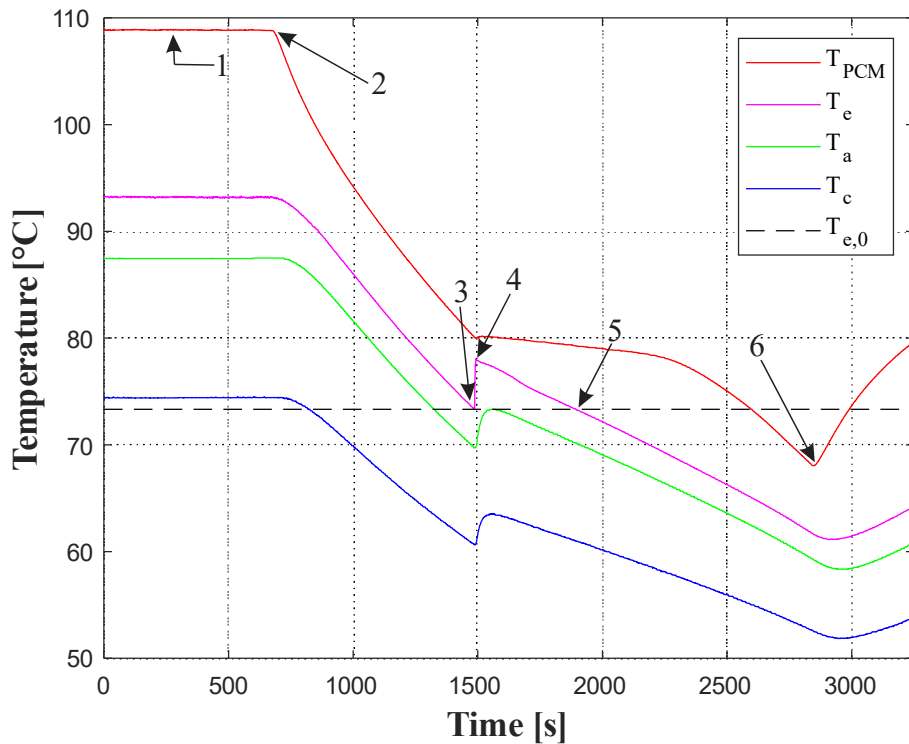


Figure 5.19. Temperature variations with time for Test 20 (Table 3.4), with $\dot{q}_{in} = 80$ W and $v_{\infty} = 12,93$ m/s.

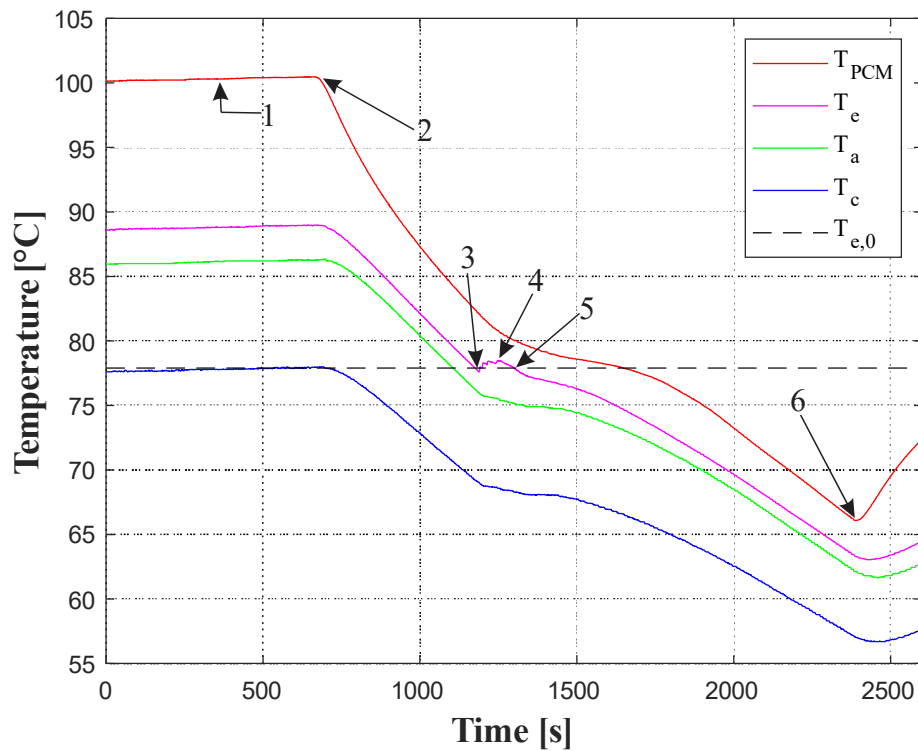


Figure 5.20. Temperature variations with time for Test 21 (Table 3.4), with $\dot{q}_{in} = 50$ W and $v_{\infty} = 4,45$ m/s.

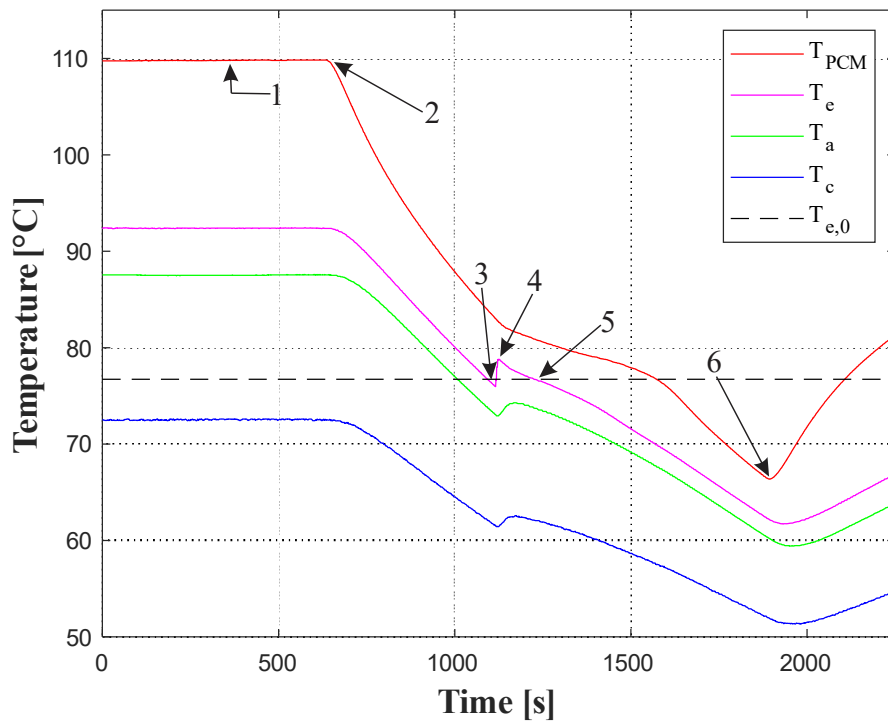


Figure 5.21. Temperature variations with time for Test 24 (Table 3.4), with $\dot{q}_{in} = 80$ W and $v_{\infty} = 12,93$ m/s.

The pattern of the thermal behavior present in all tests of the main experiment becomes clear when observing Figure 5.22, which shows an overview of the total cooling time, Δt_c ,

versus Nusselt number of the cooling mass flow, $Nu_{d,x}$, for all tests of the main experiment. The time span Δt_c was defined as the interval between points (2) and (6), while the values of $Nu_{d,x}$ were calculated using Eq. (5.1), and were proportional to the wind velocity v_∞ for each test. This overview shows that the increase of $Nu_{d,x}$ for any given PCM container resulted in the decrease of Δt_c . This is understandable since a higher Nusselt number corresponds to a higher heat transfer coefficient from the system to the heat sink (wind tunnel). Simultaneously, maintaining $Nu_{d,x}$ constant while decreasing the PCM mass, i.e. from container A to container B, also causes the total cooling time to decrease. This is attributed to the fact that a reduction in PCM mass means a reduction in thermal storage capacity, in terms of both sensible and latent heat.

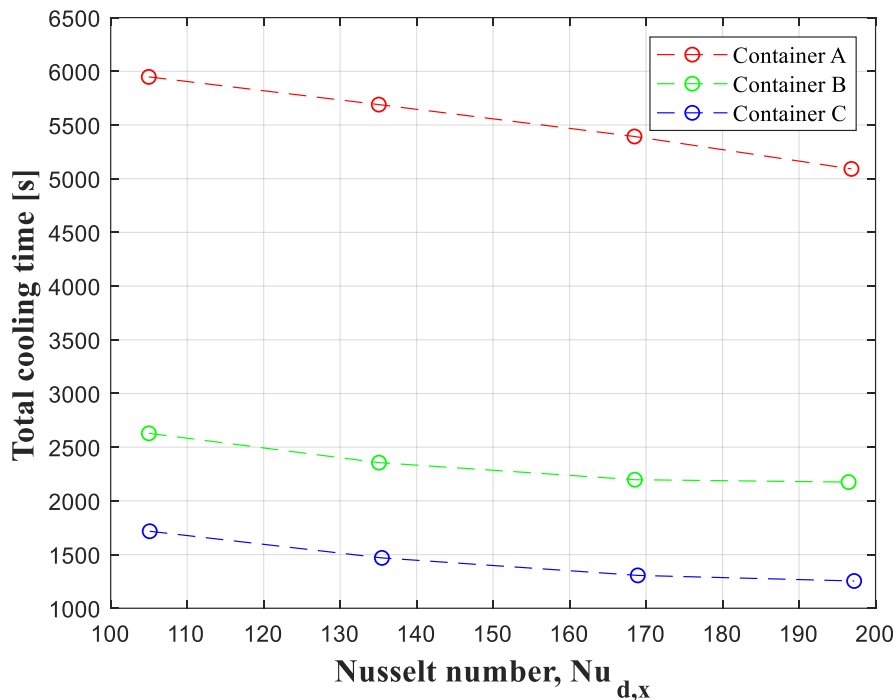


Figure 5.22. Nusselt number, $Nu_{d,x}$, versus total cooling time, Δt_c , for all tests from the main experiment (Table 3.4).

Finally, the cooling times of the baseline experiment are compared with those of the main experiment in Figure 5.23 and in Figure 5.24 in order to visualize the effect of the PCM container on the system's cooling regime. For this analysis, the drop in the adiabatic section temperature from steady state to a given moment of the transient cooling regime, ΔT_a , was set as a comparison criterion.

In Figure 5.23, baseline test 12 was compared to main experiment test 16 (container A), test 20 (container B) and test 24 (container C), seen in Table 3.4. All four tests were subjected to the same steady state input heat transfer rate, $\dot{q}_{in} = 80 \text{ W}$, and the same wind tunnel velocity, $v_{\infty} = 12.93 \text{ m/s}$. The criterion of $\Delta T_a = 10 \text{ }^{\circ}\text{C}$ was chosen to evaluate the liquid sensible cooling regime for the main experiment, since this value occurred before point (3) in Figures 5.16 to 5.21, which marked the beginning of solidification in all three tests considered with PCM. The timespan corresponding to this temperature drop was termed Δt_s , and was compared to the time required for the baseline Test 12, without PCM, to suffer the same drop of $\Delta T_a = 10 \text{ }^{\circ}\text{C}$. Then, another criterion was defined as a temperature drop $\Delta T_a = 20 \text{ }^{\circ}\text{C}$ to include the latent cooling and part of the solid sensible cooling regimes for the main experiment, since this temperature drop occurred after point (5) and before point (6), in Figures 5.16 to 5.21, for all three tests considered. This combined cooling time was termed Δt_c , and was compared to the time required for baseline Test 12, without PCM, to suffer the same temperature drop of $\Delta T_a = 20 \text{ }^{\circ}\text{C}$.

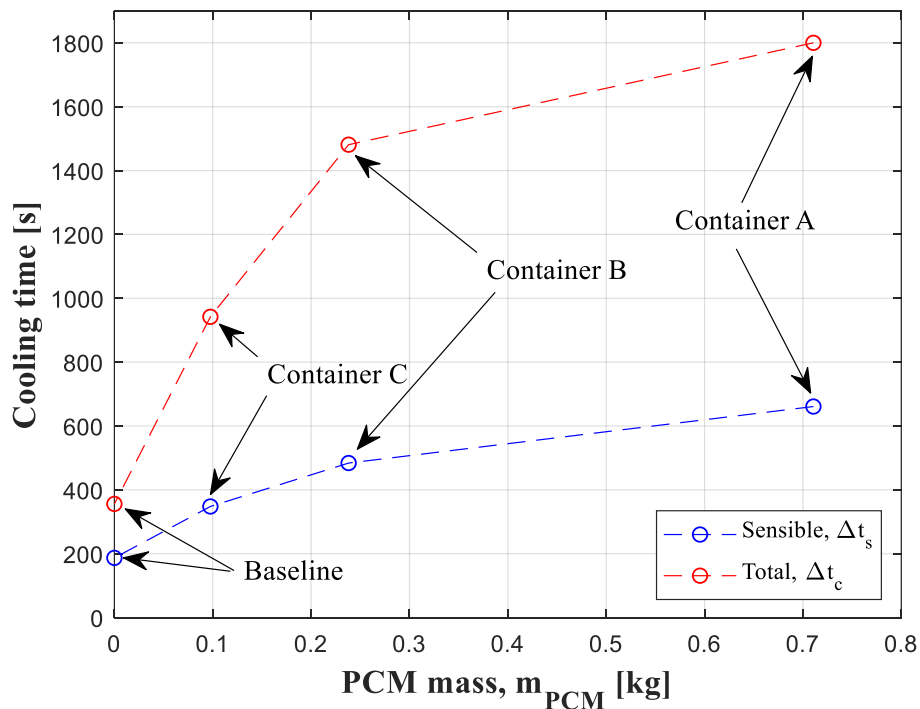


Figure 5.23. Cooling time versus PCM mass comparison between baseline test 12 and main experiment tests 16 (container A), 20 (container B) and 24 (container C) (Table 3.4), all subjected to $v_\infty = 12.93$ m/s. Δt_s was measured for a temperature drop of $\Delta T_a = 10$ °C, while Δt_c was obtained for a temperature drop of $\Delta T_a = 20$ °C.

Similarly to the previous analysis, in Figure 5.24, baseline test 7 was compared to main experiment tests 13, 17 and 21 (Table 3.4), as they were all subjected to similar steady state input heat transfer rates, $\dot{q}_{in} = 40$ W in the case of test 7, and $\dot{q}_{in} = 50$ W for the others, and the same wind tunnel velocity, $v_\infty = 4.45$ m/s. The liquid sensible cooling regime was once again evaluated using the time span, Δt_s , required for a temperature drop of $\Delta T_a = 10$ °C, which occurred before point (3) for all three tests considered from the main experiment. However, a different criterion of a temperature drop $\Delta T_a = 15$ °C was defined to include the latent cooling and part of the solid sensible cooling regimes for the main experiment, limited by the maximum temperature drop achieved by baseline Test 7, without PCM, which was used as the basis for comparison. As in the previous analysis, this temperature drop occurred after point (5) and before point (6) for all three tests of the main experiment, and the time required for it was once again termed Δt_c .

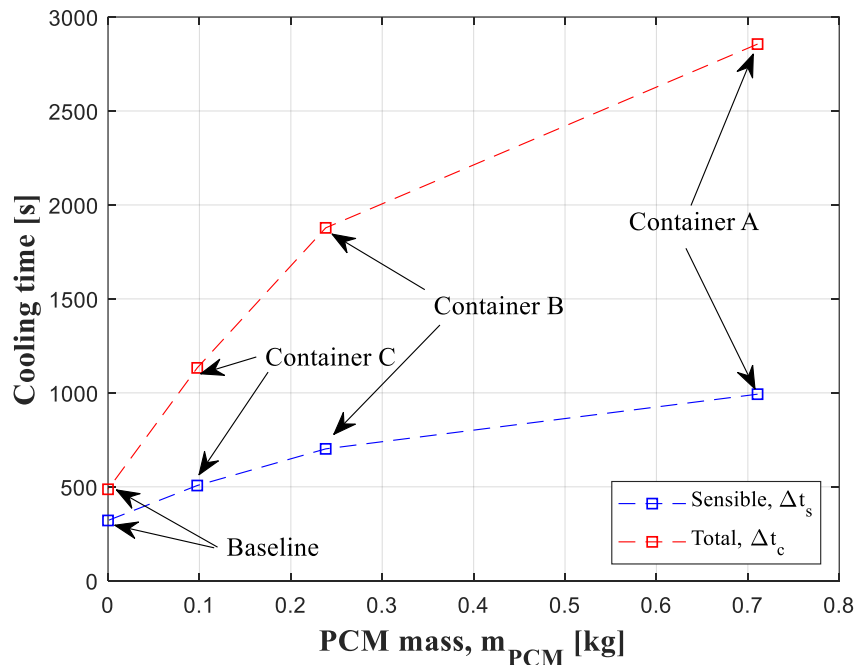


Figure 5.24. Cooling time versus PCM mass comparison between baseline test 7 and main experiment tests 13 (container A), 17 (container B) and 21 (container C) (Table 3.4), all subjected to $v_\infty = 4.45$ m/s. Δt_s was measured for a temperature drop of $\Delta T_a = 10$ °C, while Δt_c was obtained for a temperature drop of $\Delta T_a = 15$ °C.

The results of both Figure 5.23 and Figure 5.24 show a gradual increase in sensible cooling time, Δt_s , as the PCM mass increases, and a more substantial increase in cooling time once the latent heat stage is included in the analysis (Δt_c). These results are in agreement with those of Figure 5.22, which also shows the positive influence of PCM mass over the total transient cooling time. The overall results presented for the main experiment followed the same patterns of behavior previously seen in the visualization experiment (Section 5.1.2), with the added benefit of measurable Nusselt numbers on the heat sink, which allowed for more control over the heat transfer conditions of the experiment and allowed for a quantitative analysis of the transient cooling phenomena.

5.2 ANALYTICAL MODELS RESULTS

This section presents and discusses the results from the analytical models presented in Chapter 4, and a comparison with the experimental data.

5.2.1 MODELS FOR STEADY-STATE OPERATION

The results from the analytical models used to describe the thermal behavior of the thermosyphon and the PCM container during steady-state operation are shown in this section, which served as a basis for the transient state models.

a) THERMOSYPHON MODELS

As mentioned in Section 4.1, a closed two-phase thermosyphon can be modeled using an analogy with electric circuits. In order to choose the most appropriate literature correlations for the resistance associated with evaporation heat transfer, R_3 , and the resistance associated with condensation, R_7 the current chapter presents a comparison between experimental data from the baseline experiment, and correlations from the literature, which were presented in Section 0. In the current analysis, the evaporator resistance R_{evap} includes R_3 as well as the conduction resistance R_2 through the evaporator wall, while the condenser resistance R_{cond} combines R_7 with the conduction resistance R_8 through the condenser wall.

Figure 5.25 shows the analytical and experimental values of R_{evap} , plotted as a function of the experimental heat transfer rate. The correlations analyzed for R_3 are those of Groll and Rosler (GROLL; ROSLER, 1992), $R_{3,GR}$, given by Eq. (4.4); Farsi (FARSI *et al.*, 2003), $R_{3,F}$, given by Eq. (4.7); and Kiyomura correlation (KIYOMURA *et al.*, 2017), $R_{3,K}$, given by Eq. (4.9). It is observed that all correlations underestimated the experimental values of thermal resistance, with Farsi's correlation showing the closest approximation. The data shows a descending trend for R_{evap} as the heat transfer rate increased, which was also observed with both Farsi and Kiyomura models, while Groll and Rosler deviated from that trend. This difference in behavior is most likely related to the fact that Groll and Rosler consider both pool boiling and film evaporation in their analysis, while the models of Farsi and Kiyomura assume pool boiling as the main form of evaporation heat transfer. Large differences of up to 150 %

are observed between the three correlations, and the smallest error when compared to the experimental data was of the order of 30 %, for the Farsi correlation.

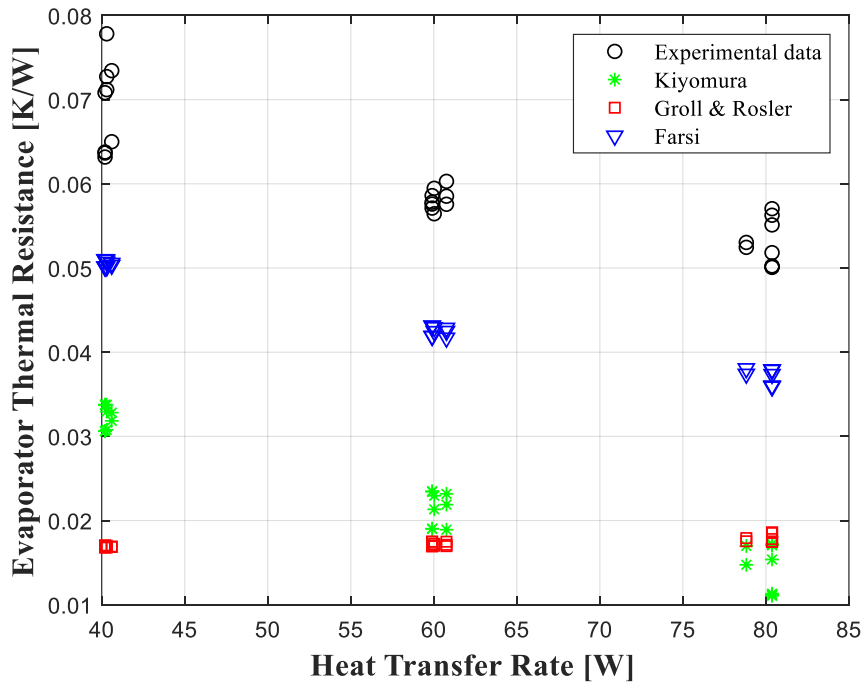


Figure 5.25. Experimental evaporator thermal resistance versus heat transfer rate and analytical models for R_{evap} with correlations from Kiyomura, Groll & Rosler, and Farsi.

The models and data relative to the condenser are seen in Figure 5.26. The correlations for R_7 were those of Groll and Rosler (GROLL; ROSLER, 1992), $R_{7,GR}$, given by Eq. (4.7); Nusselt modified, $R_{7,N}$ (GROSS, 1992), given by Eq. (4.14); and Kaminaga (*apud* BELLANI, 2017), $R_{7,K}$, given by Eq. (4.15). The results show that both the correlations of Groll and Rosler and the modified Nusselt underestimated the experimental data, with the best agreement shown by the modified Nusselt. This is expected since both correlations are based on the Nusselt model for film condensation over a flat plate, which disregards the effects of shear stress on the liquid-vapor interface due to the vapor flow, as mentioned in Section 0, that cause the condensation layer to become thicker and the thermal resistance to increase. On the other hand, the Kaminaga correlation overestimates the experimental values. This model heavily depends on the effects of shear stress, and typically works better when applied to turbulent flows. Similarly to the case of R_{evap} , the data for R_{cond} showed an ascending trend with the heat transfer rate, which is also observed with Groll & Rosler and the modified Nusselt, while Kaminaga decreases as the heat transfer rate increases. This indicates that the experimental data had a transition flow regime, dominated by laminar film condensation but with significant vapor shear stress.

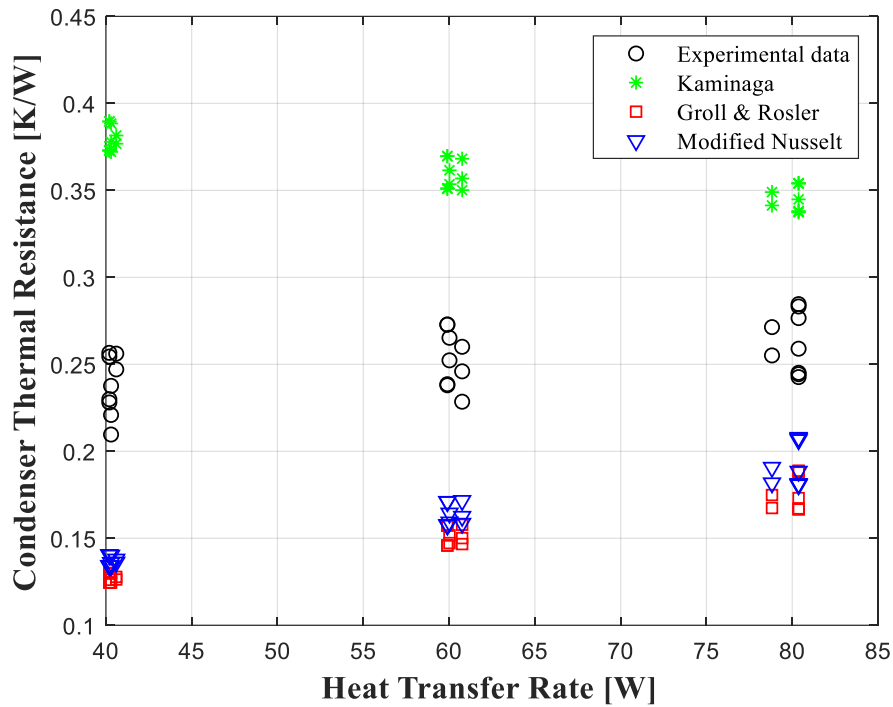


Figure 5.26. Experimental condenser thermal resistance versus heat transfer rate and analytical models for R_{cond} with correlations from Kaminaga, Groll & Rosler, and modified Nusselt.

The overall thermal resistance of the closed thermosyphon, R_{CTPT} , can be obtained by the summation of R_{evap} and R_{cond} , as given by Eq. (4.20). Three different correlations for the evaporation resistance R_3 are analyzed here, which means three different possibilities for R_{evap} . The same goes for the condensation resistance R_7 , that is, three different correlations were considered for R_{cond} . Therefore, by combining these possibilities one obtains nine overall models for R_{CTPT} , which were labeled from 1 – 9 and can be seen on Table 5.3. From these, the two that showed the closest approximation to the experimental data are those represented by combination 3, named $R_{CTPT,3}$, and combination 5, named as $R_{CTPT,5}$. The comparison with the experimental values is seen in Figure 5.27., which shows that $R_{CTPT,3}$ overestimated the experimental results with a maximum error of $\varepsilon_{max} = +45\%$, while $R_{CTPT,5}$ underestimated the results with a maximum error of $\varepsilon_{max} = -45\%$.

Table 5.3 – Matrix of combinations among condenser and evaporator models.

Condenser: Evaporator:	Groll & Rosler	Modified Nusselt	Kaminaga
Groll & Rosler	1	2	3

Farsi	4	5	6
Kiyomura	7	8	9

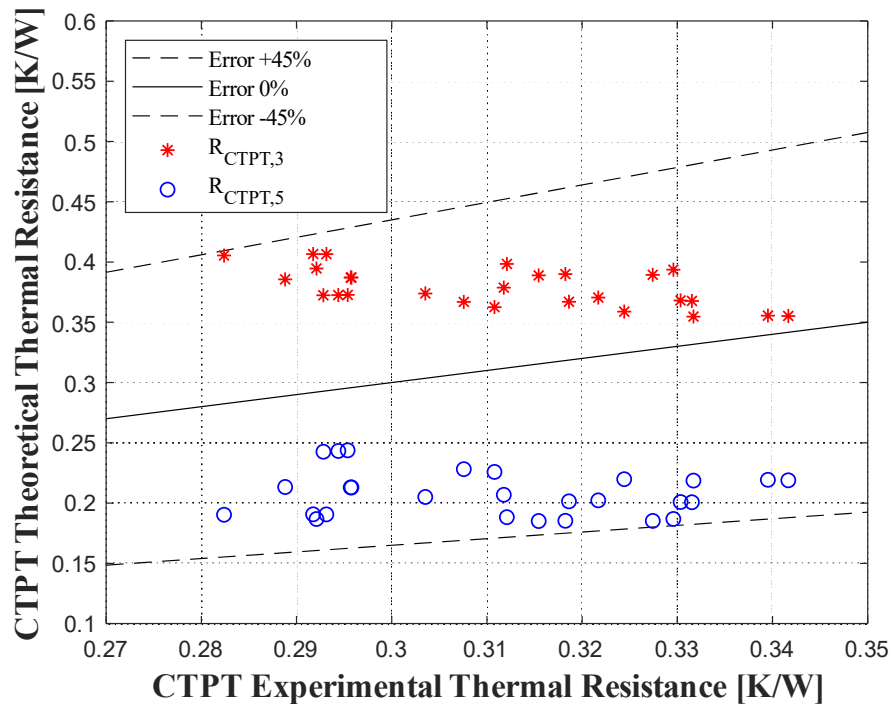


Figure 5.27. Comparison between experimental and theoretical values of R_{CTPT} with the two best combinations of R_{evap} and R_{cond} from Table 5.3.

The reason for the large differences among different literature correlations for the evaporation and the condensation resistances can be analyzed with Figure 5.28, which shows, in red, the condenser and the evaporator models used in $R_{CTPT,3}$. Both presented differences larger than $\pm 50\%$ when compared with the experimental data. On the other hand, the condenser and evaporator models used in $R_{CTPT,5}$, seen in blue, both showed differences smaller than $\pm 50\%$ relative to the experimental data. Therefore, $R_{CTPT,5}$ was chosen here to represent the closed thermosyphon overall resistance, R_{CTPT} .

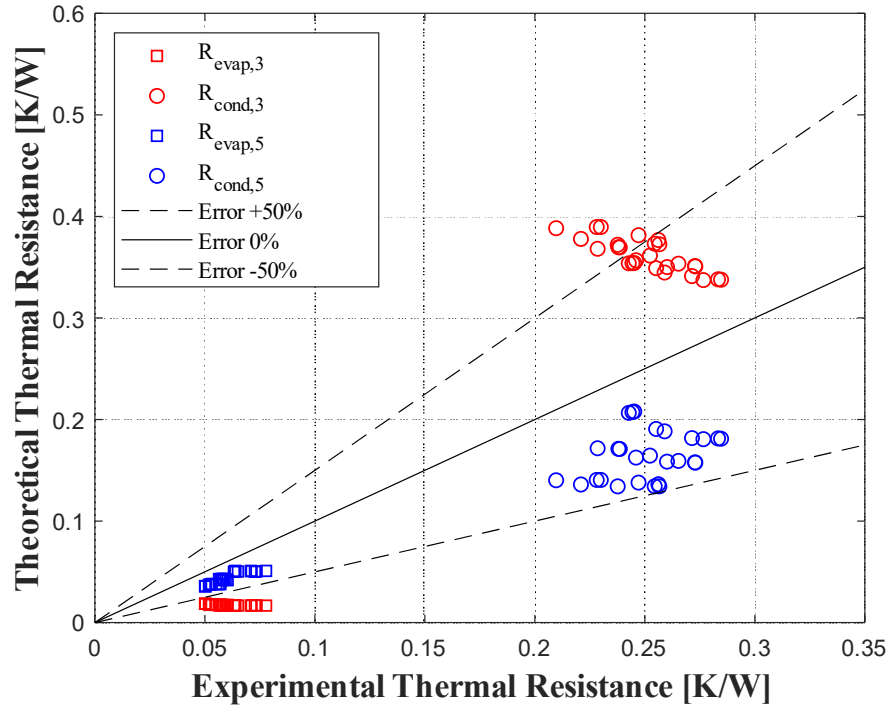


Figure 5.28. Theoretical and experimental values of R_{CTPT} for R_{evap} and R_{cond} from Table 5.3, $R_{CTPT,3}$ and $R_{CTPT,5}$.

According to Figure 4.2, the total resistance, R_t , was defined as the summation of the total thermosyphon resistance, R_{CTPT} , and the external condenser resistance, R_9 . Heat transfer between the condenser and the heat sink was already modeled in Section 3.2.1 and evaluated according to Section 5.1.1, where a semi-empirical correlation was proposed for the convection heat transfer coefficient, h_∞ , and is given by Eq.(5.1). Therefore, R_9 can be calculated from Eq. (5.3), where A_c is the external area of the condenser.

$$R_9 = \frac{1}{h_\infty A_c} \quad (5.3)$$

Figure 5.29 shows the experimental values of R_9 and R_{CTPT} versus the heat transfer rate, where it can be seen that $R_9 \gg R_{CTPT}$ for all tests, showing that the external resistance accounts for the largest part of the total resistance R_t . Since the correlation obtained for h_∞ showed a close agreement with the experimental data, with errors within $\varepsilon_{max} = \pm 15\%$, it is expected that R_t should also closely agree with the data, despite the larger errors of the models for R_{CTPT} . The comparison between experimental and analytical values of R_t is shown in Figure

5.30, where this is indeed observed, and the error of the analytical models for R_t shows errors within $\pm 15\%$.

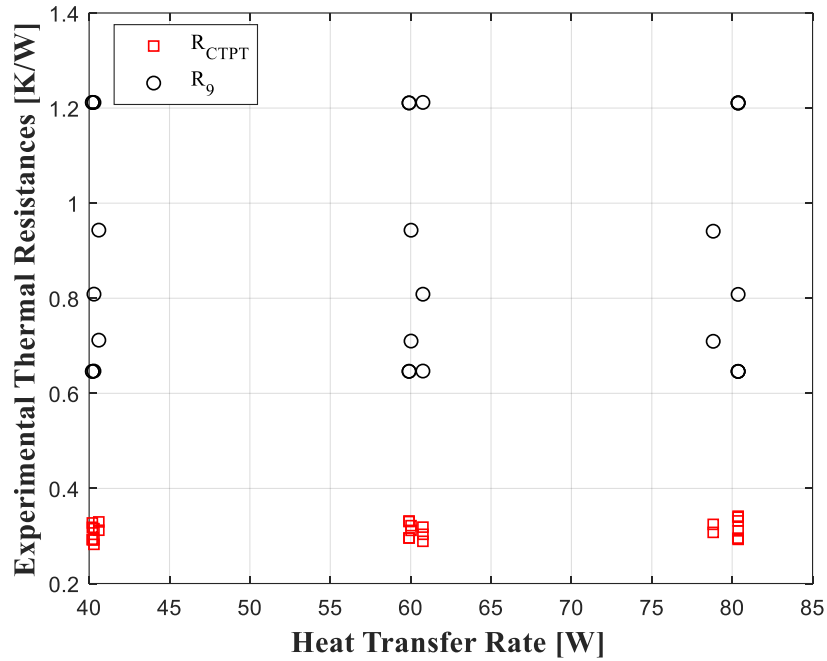


Figure 5.29. Experimental values of thermal resistance versus heat transfer rate.

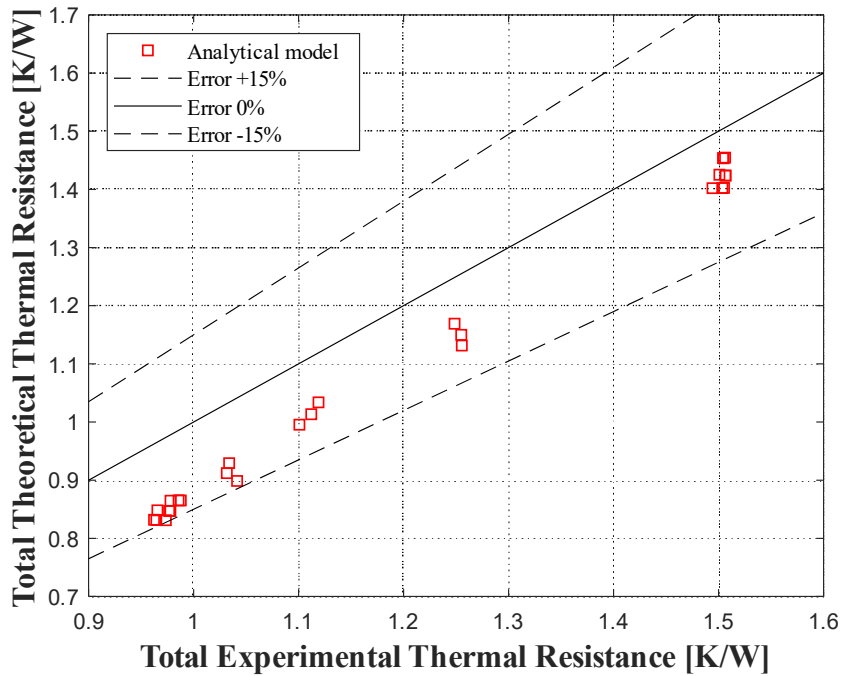


Figure 5.30. Comparison between experimental and theoretical total resistance.

Figure 5.31 shows the experimental temperature data versus the predicted values using the semi-empirical Nusselt number correlation for R_9 , Farsi’s evaporation model for R_3 , and

the modified Nusselt model for R_7 , along with the established models for conduction resistances R_2 and R_8 . The temperatures are predicted by the analytical models and agree with the experimental data within $\pm 15\%$, confirming the results shown in Figure 5.30.

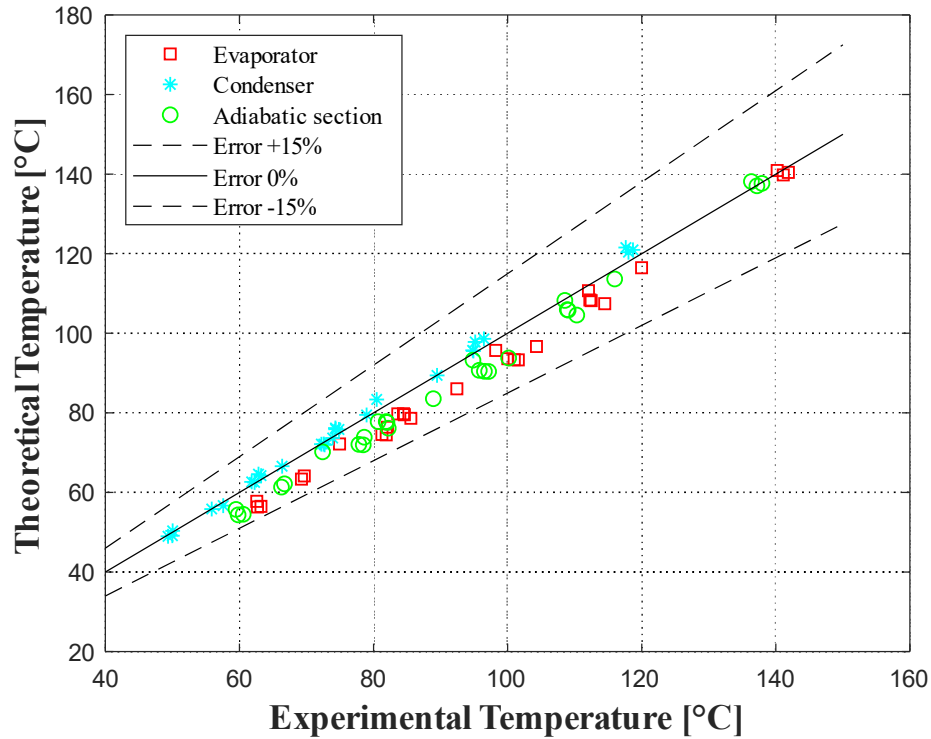


Figure 5.31. Theoretical and experimental temperatures at the different thermosyphon sections.

The errors between the analytical model and the experimental data, of the order of $\pm 15\%$, were considered small. Therefore, it is concluded that the chosen correlation for R_t accurately predicts the combined thermal resistance of the closed thermosyphon and the heat sink, and is considered valid for modeling both steady state operation and transient cooling regime in the experiments.

b) PCM CONTAINER THERMAL RESISTANCE

As discussed in Section 4.1.2, the external evaporator resistance for the thermosyphon, R_1 , is actually the same as the PCM resistance, R_{PCM} . In order to obtain a model for R_{PCM} , it was first necessary to find which heat transfer mechanism was predominant in the liquid PCM pool, whether that was conduction or convection. For this purpose, a scale analysis was conducted for the PCM container's Rayleigh number versus aspect ratio, according to BEJAN (2013), and the results can be seen in Figure 5.32. These results show that the criteria from Eq. (4.26) was met in all three of the PCM containers used in this study, and for all of the twelve tests that composed the main experiment (tests 13 to 24, on Table 3.4). That is, in all cases, the condition $Ra_H^{-1/4} < H/L < Ra_H^{1/4}$ was satisfied, which effectively means that the effects of natural convection are significant and must be considered when calculating the thermal resistance R_{PCM} .

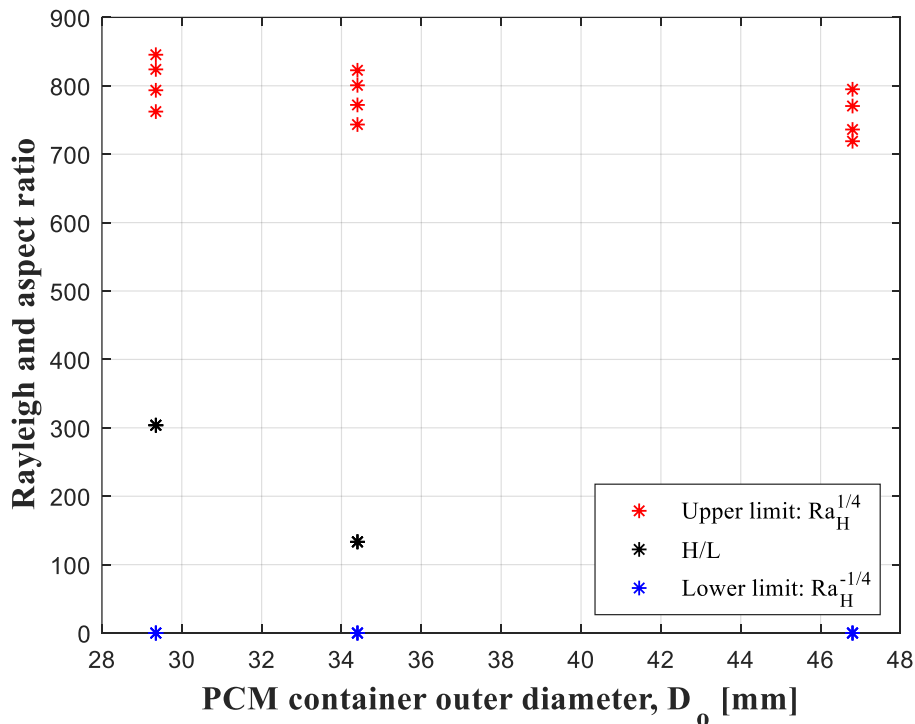


Figure 5.32. Dimensionless values of Rayleigh number and aspect ratio versus PCM diameter for the three PCM containers, and for all tests of the main experiment (tests 13 to 24 in Table 3.4).

With the model for effective conductivity, k_{eff} presented in Eq. (4.36), and the semi-empirical coefficients $C_3 = 0,0025$ and $C_4 = 0,39$ found by using the least squares method to adjust Eq. (4.36) to the data from the main experiment (tests 13 to 24, on Table 3.4). The

correlation for effective conductivity of the PCM pool, which takes into account the effects of natural convection, is given by:

$$\frac{k_{eff}}{k_l} = 0.0025(Ra_{LC}^*)^{0.39} \quad (5.4)$$

The results of the correlation for k_{eff} compared to the experimental data can be seen in Figure 5.33, which shows that the maximum error was $\varepsilon_{max} = \pm 7\%$, and the mean error was $\varepsilon_{mean} = \pm 3\%$, relative to the experimental data. Therefore, the analogy used to express overall heat transfer in the form of effective conductivity is considered valid, also validating the model of the thermal resistance of the PCM liquid pool, R_{PCM} , as a conduction resistance, seen in Eq. (4.38).

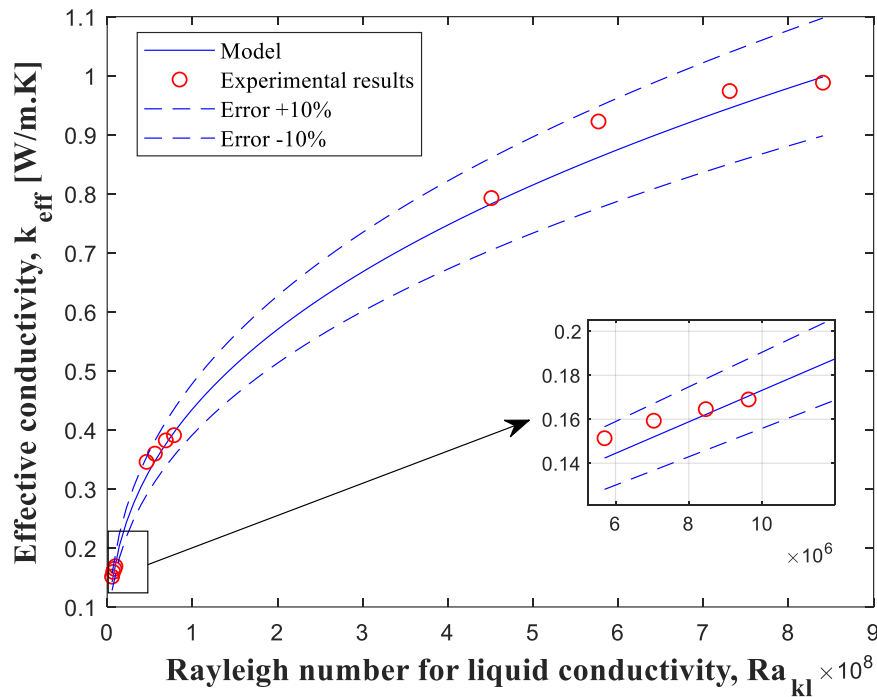


Figure 5.33. Comparison between the semi-empirical model and experimental data for effective conductivity, k_{eff} , versus Ra_{kl} .

5.2.2 MODELS FOR TRANSIENT STATE: LIQUID SENSIBLE COOLING

As mentioned previously in both Section 3.2.2 and Section 3.2.4, after the power supply is shut off, the PCM enters a transient cooling regime that is composed of three stages: liquid sensible cooling, followed by latent cooling, and solid sensible cooling. The total duration

of the liquid sensible cooling regime begins the instant the heat supply was cut off, t_0 ; and ends with the sudden rise in evaporator temperature, T_e , when the liquid – solid phase change begins. However, this end point happened at different temperatures for each test, and is marked by a phenomenon that cannot be accounted for in a sensible heat analysis, making it an unreliable end criterion. Therefore, for the purpose of comparing experimental and analytical results, the end of the liquid sensible cooling regime was considered to be the moment when the average PCM pool temperature reached the PCM melting point, that is, $\overline{T_{PCM}} = T_m$, where $\overline{T_{PCM}}$ is the average between the outer PCM wall temperature and the evaporator temperature, that is $\overline{T_{PCM}} = (T_{PCM} + T_e)/2$. The temperature T_{PCM} was obtained as an average of the readings from the thermocouples placed on the outer wall of the PCM container, while T_e was obtained as an average of the readings from the thermocouples placed on the outer evaporator wall, as seen in Figure 3.4.

As mentioned in Section 4.2.1, the lumped heat capacitance model could not be applied to the liquid transient cooling regime of the PCM. This decision is justified when observing Table 5.4, which shows the values of Bi_L , defined in Eq. (4.43), obtained for the main experiment (tests 13 to 24 on Table 3.4), with the highest value being $Bi_L = 0,32$ for Test 16 and the lowest, $Bi_L = 0,19$ for Test 21. These values did not satisfy the criterion for lumped analysis, that is $Bi_L < 0,1$ (INCROPERA, 2008), indicating that the temperature gradient and heat transfer phenomena within the PCM are not negligible, and must be taken into consideration when modeling the transient sensible cooling regime.

Table 5.4 – Variables and results of dimensionless Bi_L for the main experiment, tests numbered 13 to 24 (Table 3.4).

Test	L [mm]	k_{eff} [W/(m.K)]	h_{eq} [W/(m ² .K)]	Bi_L
13	15,2	0,78	12,9	0,25
14	15,2	0,86	15,7	0,28
15	15,2	0,95	18,6	0,30
16	15,2	1,00	20,9	0,32
17	5,3	0,32	12,9	0,21
18	5,3	0,35	15,7	0,24
19	5,3	0,38	18,5	0,26
20	5,3	0,4	20,7	0,28
21	2,1	0,14	12,9	0,19

22	2,1	0,15	15,8	0,22
23	2,1	0,17	18,6	0,24
24	2,1	0,17	20,8	0,25

The 1D transient heat conduction solution defined in Eq. (4.77) was used as the analytical model for PCM temperatures in the sensible liquid cooling regime, where the dimensionless temperatures are $\theta_{1,1D}$ for the evaporator, referring to the position at $\xi = \xi_1$; $\theta_{2,1D}$ for the outer PCM wall, at $\xi = \xi_2$; and $\theta_{mid,1D}$ at the midsection where $\xi = (\xi_1 + \xi_2)/2$. The experimental data was written in dimensionless variables as $\theta_{1,exp}$, $\theta_{mid,exp}$ and $\theta_{2,exp}$ in the corresponding sections, where $\theta_{mid,exp}$ is obtained as the average between $\theta_{1,exp}$ and $\theta_{2,exp}$, since there were no thermocouples placed at the midsection of the PCM pool. The melting/solidification temperature, T_m , was also expressed in dimensionless terms as θ_m .

The analytical model only accounts for sensible cooling phenomena, and therefore it cannot predict the moment where solidification phase change occurs, which also marks the last moment where this model is applicable to the experimental data. Therefore, an end criterion had to be chosen for this analysis, based on the experimental results. The exact temperatures when solidification started were different for each test of the main experiment (tests 13 to 24 on Table 3.4), so they could not be used as a reliable end criterion. However, it was observed that, for all these tests, phase change began after the average PCM temperature reached the melting point, and before the outer PCM temperature reached the same point, that is, after $\theta_{mid,exp} = \theta_m$, but before $\theta_{2,exp} = \theta_m$. Therefore, the moment when $\theta_{mid,exp} = \theta_m$ was chosen as the end criterion for the liquid sensible cooling analysis, and the total time required for the PCM to go from the initial steady state temperature until this moment was expressed as the total dimensionless time, Fo_{exp} . This experimental data was compared to the 1D analytical model's prediction for the total dimensionless time, Fo_{1D} , when the average PCM temperature reached the melting point, that is, for $\theta_{mid,1D} = \theta_m$. The error for each test was calculated as:

$$\varepsilon = \left| \frac{Fo_{1D} - Fo_{exp}}{Fo_{exp}} \right| \times 100\% \quad (5.5)$$

Figure 5.34 shows a comparison between the 1D conduction analytical model and experimental data for Test 13 (Table 3.4), corresponding to the lowest value of Nusselt number

in the heat sink, $Nu_{d,x}$, with the largest of the three PCM containers (container A, $D_o = 2''$) chosen from the main experiment. Among all the tests analyzed in this section (tests 13 to 24 on Table 3.4), the one presented in Figure 5.34 showed the best agreement between analytical model and experimental data, which can be seen as the predicted moment for $\theta_{mid,1D} = \theta_m$, marked as point (1), occurs at nearly the same time as the experimental moment for $\theta_{mid,exp} = \theta_m$, marked as point (2). The error for this test, calculated as Eq.(5.5), corresponded to the overall minimum error, $\varepsilon_{min} = \pm 1 \%$.

Figure 5.35 shows the result for test 20, with the highest $Nu_{d,x}$, and the medium size PCM container (container B, $D_o = 1 \frac{1}{2}''$). This test showed the worst agreement between experimental and analytical results, which can be seen as point (1) occurs considerably sooner than point (2). The error for this test corresponded to the maximum overall error, $\varepsilon_{max} = \pm 12 \%$.

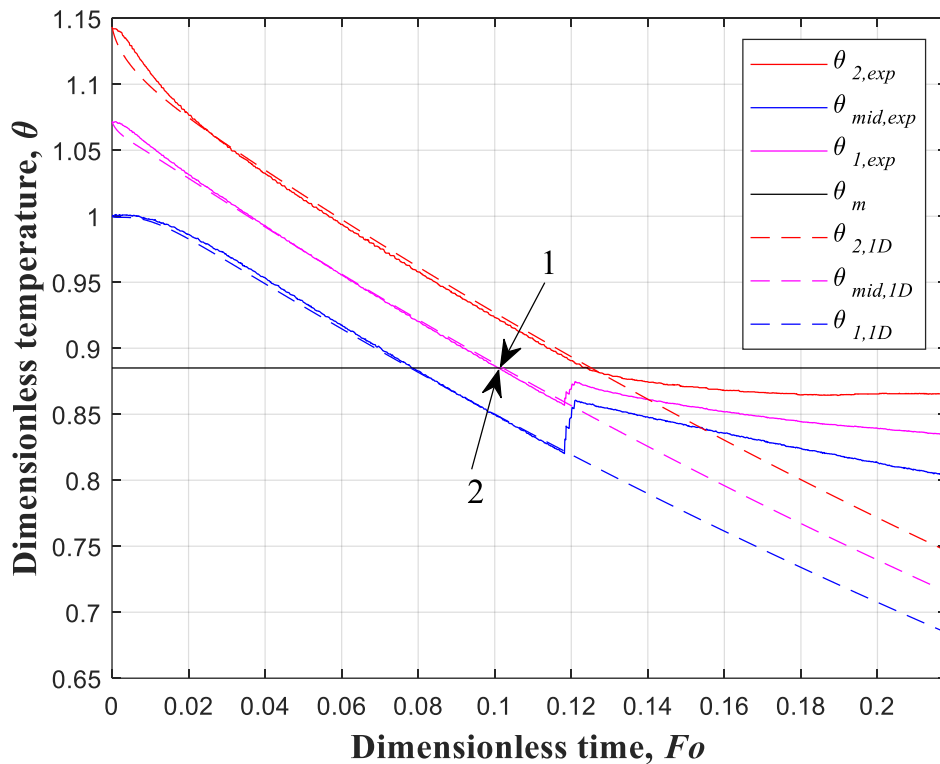


Figure 5.34. Comparison between experimental data and analytical model predictions for dimensionless temperature, θ , as a function of dimensionless time, Fo , for Test 13 (Table 3.4).

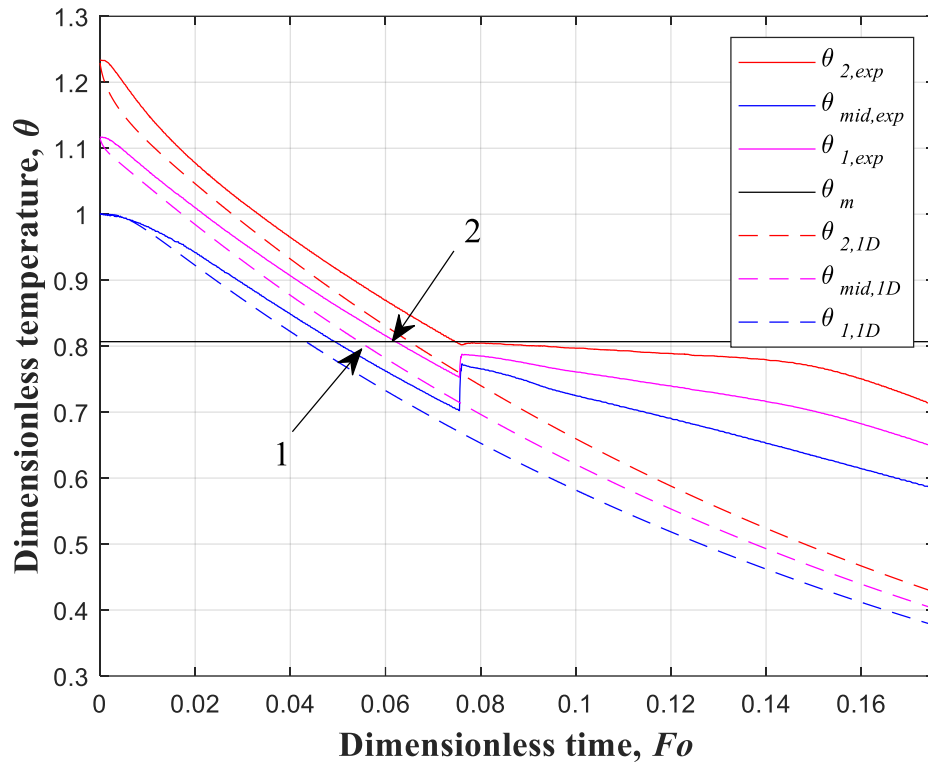


Figure 5.35. Comparison between experimental data and analytical model predictions for dimensionless temperature, θ , as a function of dimensionless time, Fo , for Test 20 (Table 3.4).

A plot of the experimental data and the analytical model predictions as a function of the total dimensionless time is shown in Figure 5.36. The full line corresponds to the perfect match between experimental data and model predictions. The regions between dashed lines represents the error margins of $\pm 15\%$. The mean error was $\varepsilon_{mean} = \pm 7\%$, so the errors can be considered acceptable and the analytical model was therefore valid for this study. This means that the thermal behavior of the system can be appropriately modeled and predicted in the early stages of a thermal oscillation, from the moment it leaves steady state operation, until the moments right before the PCM begins to solidify.

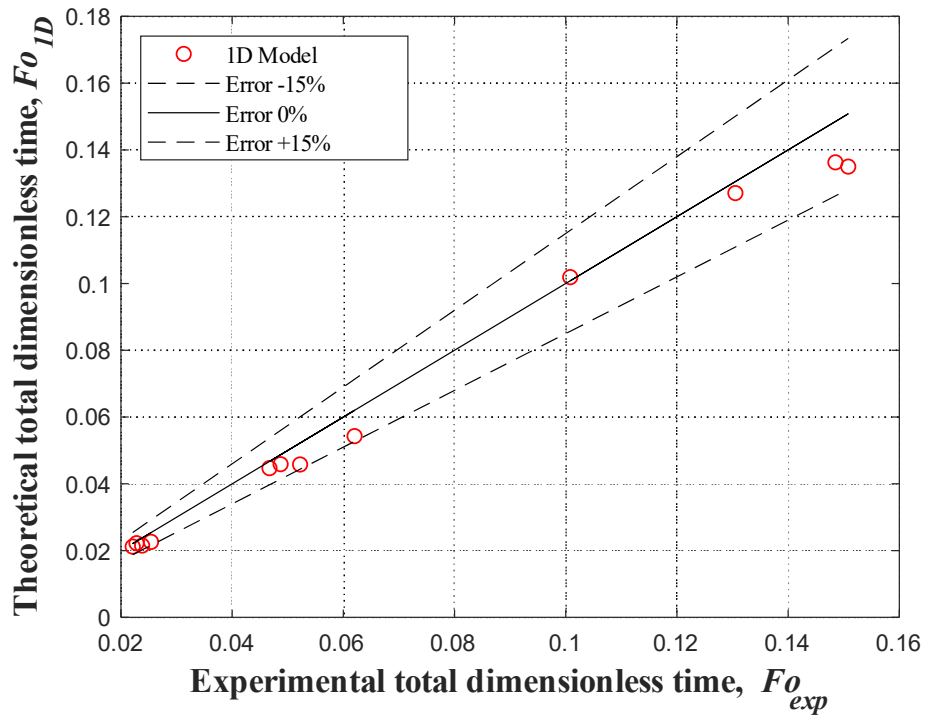


Figure 5.36. Comparison between experimental and analytical model predictions for the total dimensionless time, Fo , for tests 13 to 24 (Table 3.4).

5.2.3 MODELS FOR TRANSIENT STATE: CRITICAL LATENT HEAT OF SOLIDIFICATION

This section presents and discusses the results of the models described in Section 4.3, beginning with the criterion for the critical solidification regime, mentioned in Section 4.3.1, then moving on to the results of the semi-empiric correlation for the duration of the critical regime, as described in Section 4.3.2, and finishing with the results of latent heat effectiveness, a concept defined in Section 4.3.3.

a) CRITERION FOR THE CRITICAL SOLIDIFICATION REGIME

As mentioned in Section 4.3.1, the experimental data from all twelve tests of the main experiment (tests 13 to 24 in Table 3.4) showed a pattern for the evaporator and PCM experimental thermal resistances, that is, $R_{e,exp}$ and $R_{PCM,exp}$ respectively. The pattern becomes clear when observing both Figure 5.37 for test 13, and Figure 5.38 for test 21, shown here as examples. The pattern can be described as follows: at steady state, seen as point (1), PCM resistance is significantly larger than the evaporator resistance, that is, $R_{PCM} \gg R_e$. Then, as

the power supply is cut off at point (2), the system enters transient cooling, and R_{PCM} decreases until eventually stabilizing at an approximately constant value for the liquid sensible cooling regime. After this, at point (3) the PCM begins to solidify, and R_{PCM} drops suddenly until it reaches the same order of magnitude as R_e . This indicates that indeed the heat transfer mechanism for R_{PCM} has shifted from natural convection to liquid-solid phase change, as it matched the thermal resistance of the liquid-vapor phase change associated with R_e . Meanwhile, also near point (3), R_e suddenly rises and then falls just as quickly back to a lower value. This discrepancy can be understood observing the experimental results from Section 5.1.4, where it can be seen that the evaporator is affected first by the release of heat from the PCM solidification, before the other sections of the thermosyphon. Therefore T_e rises first, and then T_a and T_c follow only a few seconds later. This delay causes a temporary increase in the temperature difference $\Delta T = T_e - T_a$ that is used to calculate the resistance R_e . Then, near point (4) R_{PCM} reaches a minimum value while R_e stabilizes at a constant value, which is practically the same as before solidification began, corroborating the hypothesis that the sudden rise of R_e seen at point (3) was only a temporary discrepancy due to the delay of the thermosyphon in experiencing the effects of solidification. After point (4), R_{PCM} continues to increase until $R_{PCM} \gg R_e$ once more. The results for all the other tests of the main experiment can be seen in APPENDIX B.

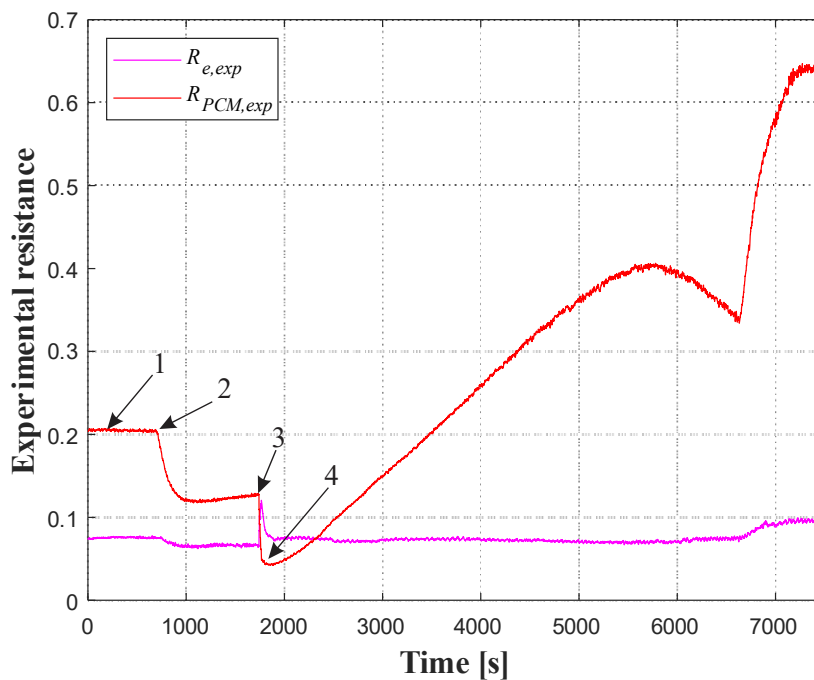


Figure 5.37. Experimental evaporator and PCM resistances as a function of time for test 13 (Table 3.4), with PCM container (A).

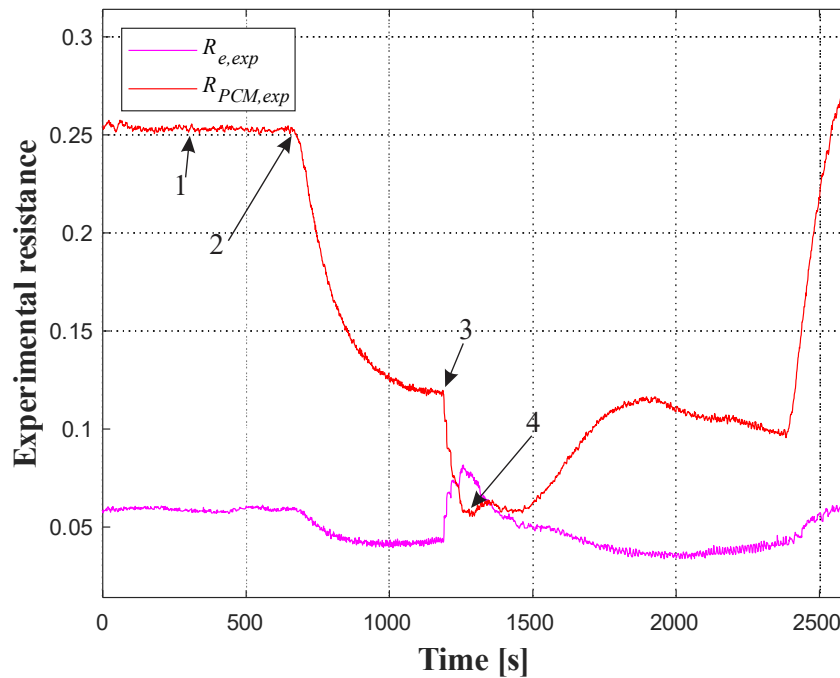


Figure 5.38. Experimental evaporator and PCM resistances as a function of time for test 21 (Table 3.4), with PCM container (C).

Despite the similar trend among all tests, the actual values of R_e and R_{PCM} vary from test to test. The dimensionless number η , defined as the ratio of R_{PCM}/R_e in Eq. (4.60), was then evaluated for all twelve tests of the main experiment (tests 13 to 24 in Table 3.4), in an attempt to identify a common pattern for the beginning and end of the critical solidification period.

The results from the ratio η can be seen in Figure 5.39 for tests 13 to 16, with PCM container (A), in Figure 5.40 for tests 17 to 20, with container (B), and in Figure 5.41 for tests 21 to 24, with container (C). These figures show a detailed view of the critical solidification period, starting shortly before the point marked as point (3) in Figure 5.37 and in Figure 5.38. The analysis of ratio η for all twelve tests revealed a common critical value, $\eta_{cr} = 1,6$, which intersects the early stage of solidification for all tests, marked as point (1) in Figure 5.39, Figure 5.40, and Figure 5.41. This value was chosen because it corresponded to the starting point of all twelve tests, with all three PCM containers, coinciding with the experimental starting point (defined as the moment $T_e = T_{e,0}$ in Section 5.1.4) within a mean difference of 0.5 s and a maximum difference of 10 s. The end of the critical solidification regime was less clear in the experimental analysis of Section 5.1.4, since the actual values of $T_{e,0}$, and the variation of T_e

and T_{PCM} with time were different for each case. Therefore, in the current analysis it is assumed that the end of critical solidification was the moment when η reaches η_{cr} for the second time, marked as point (2).

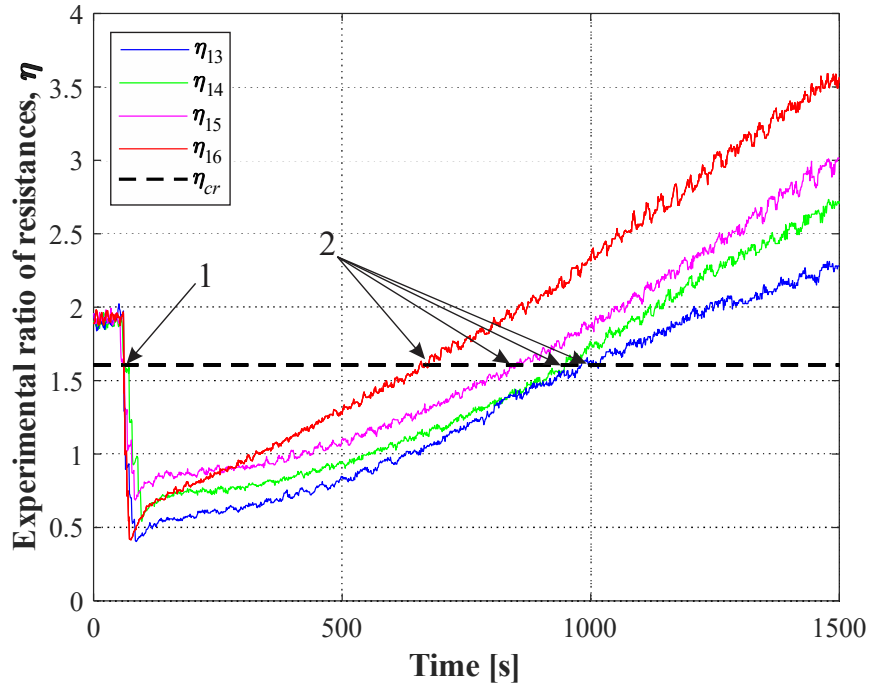


Figure 5.39. Experimental ratio η compared to the critical value, $\eta_{cr} = 1,6$ for tests 13 to 16 (Table 3.4), with PCM container (A).

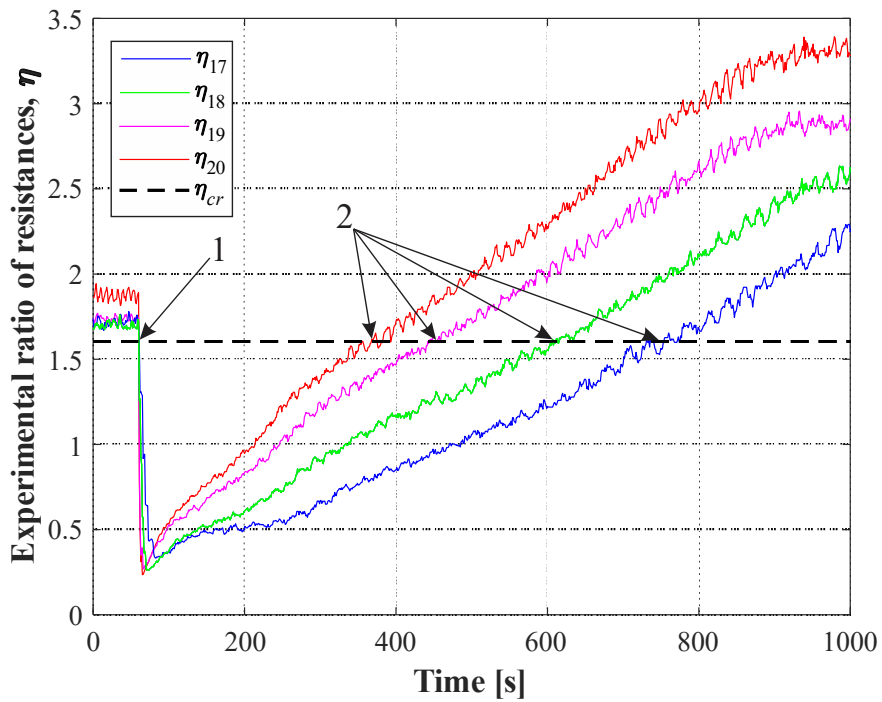


Figure 5.40. Experimental ratio η compared to the critical value, $\eta_{cr} = 1,6$ for tests 17 to 20 (Table 3.4), with PCM container (B).

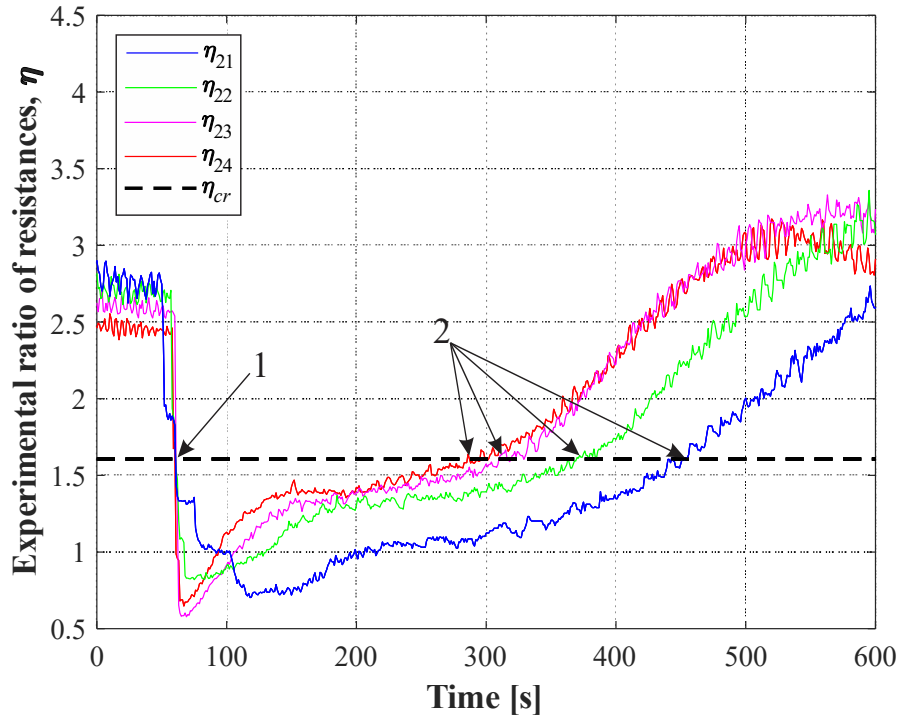


Figure 5.41. Experimental ratio η compared to the critical value, $\eta_{cr} = 1,6$ for tests 21 to 24 (Table 3.4), with PCM container (C).

The results presented in the current section show that the critical solidification period can indeed be observed and quantified in terms of thermal resistances and heat transfer phenomena, with a common start and end criterion that was consistent for all variations of the studied system, including various Nusselt numbers in the heat sink and various PCM masses. This quantification of the phenomenon served as the basis for all the subsequent analytical models and correlations.

b) SEMI-EMPIRICAL CORRELATION FOR THE DURATION OF CRITICAL LATENT HEAT TRANSFER

As discussed in Section 4.3.2, the analytical model for the critical latent heat period of the transient cooling regime was based on a dimensionless analysis of Bi_s vs. Fo_{cr} , where Bi_s is the Biot number based on the solid properties of naphthalene, as given by Eq. (4.83), and Fo_{cr} represents the dimensionless duration of critical solidification, as given by Eq. (4.82). The relationship between Bi_s and Fo_{cr} was defined by Eq. (4.84), using the method of nonlinear

regression, with an adjustment coefficient $C_0 = 0.2545$, resulting in the semi-empirical correlation:

$$Fo_{cr} = \frac{0.2545}{Bi_s} \quad (5.6)$$

The correlation defined in Eq. (5.6) fits the experimental data with $R^2 = 0,966$, within a maximum error of $\varepsilon_{max} = \pm 23\%$, and mean error of $\varepsilon_{mean} = \pm 7\%$, as seen in Figure 5.42, which presents a comparison between the analytical model and the experimental data for the main experiment. This model was therefore considered valid for the prediction of the duration of the critical latent heat period. A comparison between analytical and experimental values of Fo_{cr} , along with the maximum error, can be seen in Figure 5.43.

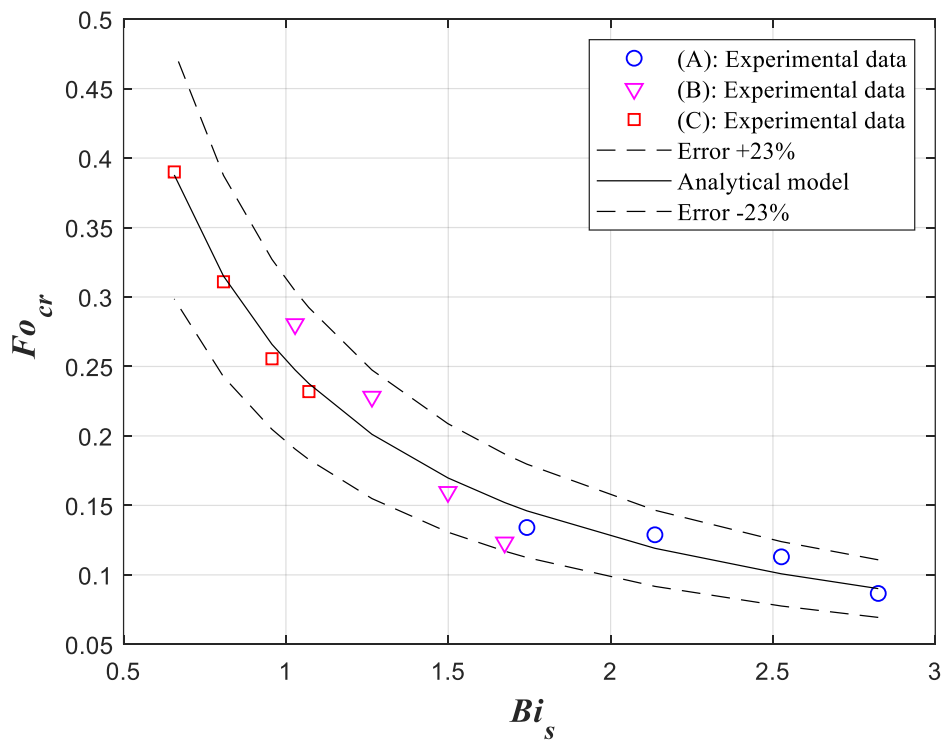


Figure 5.42. Dimensionless parameters Fo_{cr} versus Bi_s for the critical latent period, with experimental data from PCM containers (A), (B), and (C) and the proposed semi-empiric correlation.

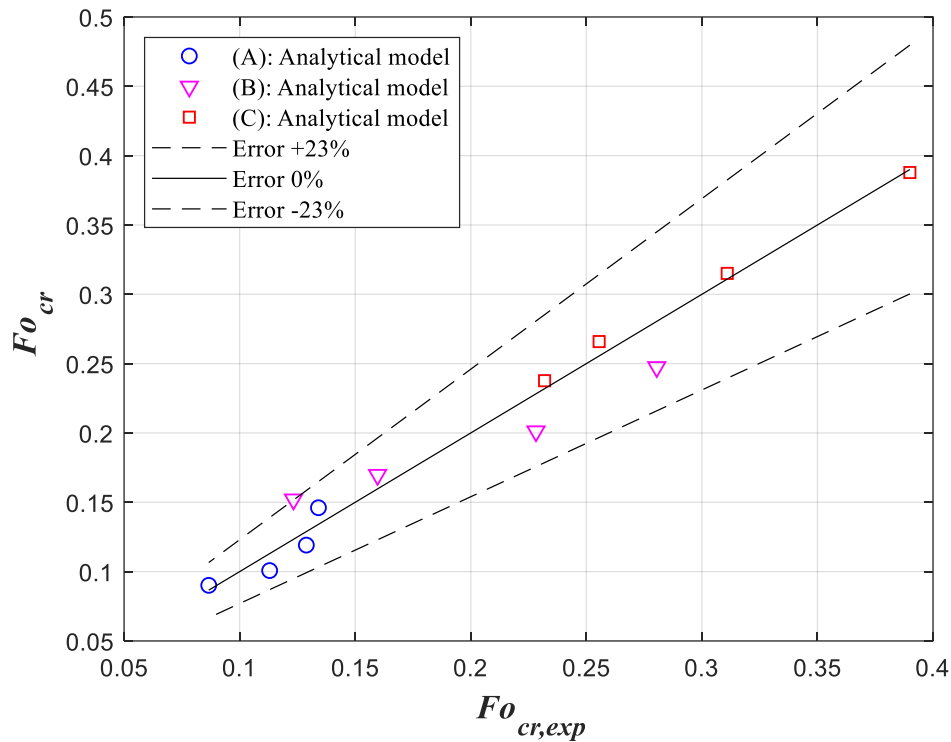


Figure 5.43. Comparison between experimental and analytical values of Fo_c for the critical latent period, and for the main experiment with PCM containers (A), (B), and (C).

c) LATENT HEAT EFFECTIVENESS

The last analytical model presented in this study was defined in Section 4.3.3, for a parameter used to evaluate the fraction of latent heat stored by the PCM that can be effectively used by the thermal process. As discussed, the ideal outcome during PCM solidification is the release of stable heat transfer rate to the thermal process, at a near constant temperature. However, as shown throughout this study, this condition was only met during the critical latent heat period, which was shorter than the time required for complete solidification. In this context, the parameter of latent heat effectiveness, ψ , was defined in Eq. (4.100) as a ratio between the latent heat released by the critical solidified layer, and the latent heat stored in the total PCM mass. The input parameters required for this model can be obtained from the PCM thermal properties, the thermal resistance of the thermosyphon used as the heat exchanger attached to the PCM, and the external temperature of the heat sink, T_∞ . All these variables can be obtained from thermodynamic property tables and established models from the literature, meaning that the PCM effectiveness ψ_{PCM} can be calculated before the construction of a new device, and so be used as a design parameter.

The results are shown in Figure 5.44, with the values of ψ_{PCM} as a function of the ratio of Biot numbers, Bi_d/Bi_s , showing the analytical model's predictions and the experimental data from all tests of the main experiment (tests 13 to 24, on Table 3.4). As one can see, the analytical values follow the same trend as the data. These results showed that, on average, the effectiveness is approximately: 40 % for container (A), 60 % for container (B), and 100% for container (C). These values appear to be consistent with the measurements of the critical solidified layer of PCM from the visualization experiment, as seen in Table 5.2. Those visual results showed a mass fraction, m^* , calculated as the mass of the critical solid layer divided by the total PCM mass, which also represents measurements of the effectiveness of the PCM storage, with values of 23% for container (A), 39 % for container (B), and 100% for container (C). While these results do not match exactly, the PCM effectiveness shown in Figure 5.44 and the mass fraction measured in Section 5.1.2 showed values with a satisfactory result, especially considering that the experiments used different cooling conditions in the heat sink (natural convection for the visual tests, versus controlled forced convection for the main experiment).

Figure 5.45 shows a comparison between the experimental and analytical values for parameter ψ_{PCM} . The analytical model agrees with the experimental data with a maximum error of $\varepsilon_{max} = \pm 25\%$, and a mean error of $\varepsilon_{mean} = \pm 13\%$. This result was considered satisfactory, especially considering that the approach used in this study simplifies a complex heat transfer phenomenon, that is the solidification under transient conditions, into a quantifiable time interval as a function of known experimental parameters.

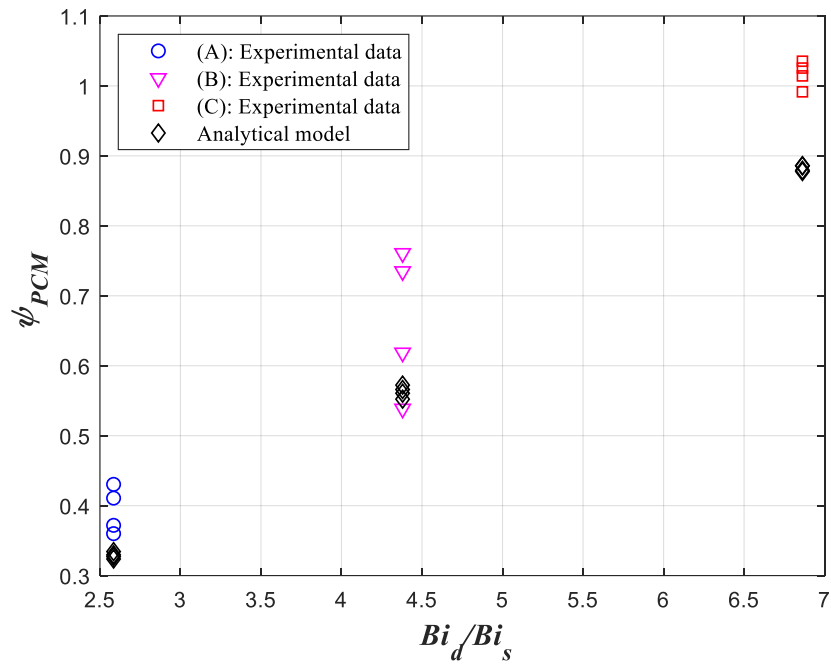


Figure 5.44. PCM latent heat effectiveness, ψ_{PCM} , versus Biot ratio Bi_d/Bi_s for the analytical model predictions and experimental data from PCM containers (A), (B), and (C).

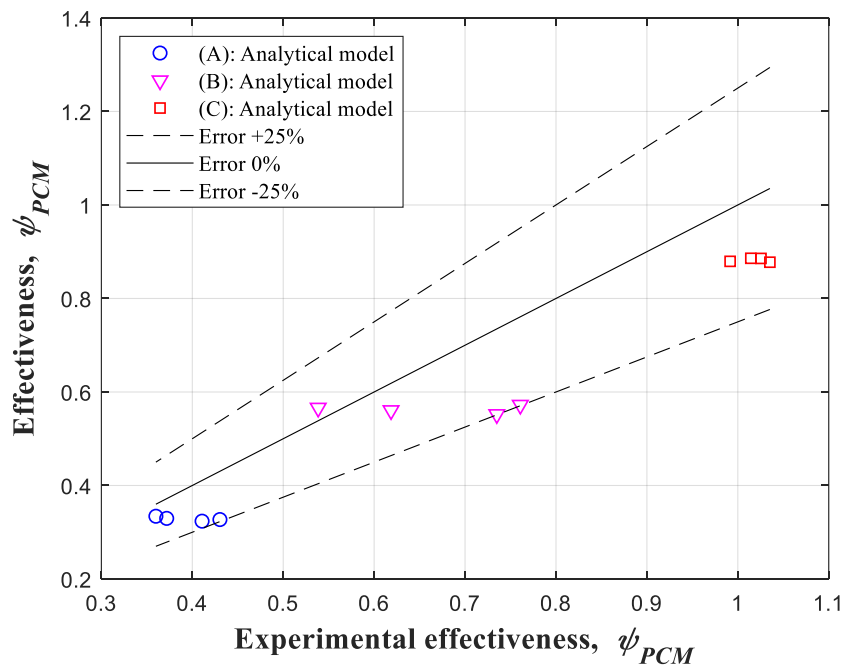


Figure 5.45. Comparison between experimental and analytical values of PCM latent heat effectiveness, ψ_{PCM} , for the main experiment and with PCM containers (A), (B), and (C).

This chapter presented both experimental and analytical results that described the formation of a critical solidified layer of PCM during the discharge of a latent heat storage system. The initial experiments yielded visual confirmation of the phenomenon, along with measurements of the solid layer thickness as a function of total PCM mass. The subsequent

experiments used controlled parameters and quantified the duration of the period of critical latent heat transfer associated with the formation of this solid layer, as a function of PCM mass and heat transfer rate to the heat sink.

The analytical models proposed in Chapter 4 were evaluated first at steady state, then at the transient liquid cooling regime. The basis for this analysis was the representation of all system components in the form of thermal resistances, first by choosing correlations from the literature for the closed thermosyphon, then by proposing a model for the PCM container. The models for both components were compared to the experimental data and considered satisfactory.

The validated models for steady state operation served as the basis for the transient state analytical models, which consisted of two analyses: one for the liquid sensible cooling stage, and another for the critical latent heat of solidification. The first was simplified as the solution to a problem of one-dimensional heat conduction, which was compared to the experimental data with satisfactory results. The modeling of the critical latent period, however, required more steps. First, this critical period was defined in terms of a beginning and end criterion, which was compared to the experimental results and considered valid. Then, the proposed semi-empirical correlation for the duration of the critical latent period was validated in comparison to the experimental data. Finally, the proposed correlation for latent heat effectiveness was analyzed with regards to the experimental results and considered satisfactory as well. Therefore, the operation of the studied thermal system was characterized for both steady state and transient cooling. More importantly, the formation of a critical solidified layer, which is the phenomenon investigated in this work, was experimentally confirmed and quantified, as well as analytically described.

6. CONCLUSIONS

This study investigated the early stages of PCM solidification coupled with a closed two-phase thermosyphon as the heat exchanger. Initial tests observed the formation of a critical solid layer of PCM over the thermosyphon surface, which acts as a thermal barrier between the heat exchanger and the PCM pool and corresponds to the period of highest heat transfer efficiency from the PCM to the process, which was called the critical latent period. The experimental results from further tests were used to obtain semi-empirical correlations for the duration of this time period, as well as a parameter for latent heat effectiveness. The proposed correlations agreed with the experimental data within a maximum error of 25 % and a mean error of 13 %, and were deemed satisfactory as a simplified model for a complex heat transfer phenomenon. These models can be used as a design parameter for PCM containers coupled with heat exchangers in order to improve the energy efficiency during latent heat extraction.

The main accomplishments and conclusions of this work are listed as follows:

- A visualization experiment was performed to observe the critical solid layer of PCM. The experimental results showed that a clearly defined solid layer is formed over the heat transfer surface, which corresponds to the time interval when the latent heat transfer rate was highest. This is considered a satisfactory confirmation of the initial hypothesis that, once the solid layer was formed, it acted as a thermal barrier between the liquid PCM and the heat exchanger, and is responsible for the low energy efficiency during PCM discharge.
- An experimental setup was designed and manufactured in order to test different sizes of PCM containers coupled with a thermosyphon under controlled heat transfer conditions, that is, heat transfer rate input, operating temperatures, and heat removal coefficient. The test conditions were considered stable and repeatable, and a semi-empirical correlation was obtained for the Nusselt number of the system's heat sink that agreed with the experimental data within a ± 5 % error.
- A comparison between the baseline and main experiment showed that the addition of PCM significantly increased the total cooling time of the thermal process, both in terms of sensible and latent heat, with latent heat showing the largest contribution.

- An analytical model was developed for the sensible stage of the transient cooling regime. The model simplified all heat transfer phenomena within the PCM container as 1D heat conduction, and used an effective conductivity value obtained from a semi-empirical correlation which agreed with the experimental data within a maximum error of 12 %, and a mean error of 7 %.
- A semi-empirical correlation was proposed for the critical latent stage of the transient cooling regime, which agreed with the experimental data within a maximum error 23 %, and mean error of 7 %.
- A parameter was defined for PCM latent heat effectiveness, which compares the total latent heat stored in the PCM container versus the latent heat provided during the critical solidification period. Then, an analytical model was developed for this parameter, which was then compared to the experimental data and showed an agreement with a maximum error of 25 % and a mean error of 13 %.
- In general, the analytical and semi-empirical correlations obtained in this study were able to model the desired outputs to a satisfactory degree, especially considering that the approach used in this study simplifies a complex heat transfer phenomenon, which is the sensible cooling and solidification of a PCM container coupled with a two-phase thermosyphon under transient conditions, into quantifiable time intervals as functions of known experimental parameters.

All the analytical models proposed in this work required input parameters that could be obtained during the design phase of the thermal system, before manufacturing, that is, the PCM thermal properties, the thermal resistance of the thermosyphon, and the heat transfer conditions at the system's heat sink. Therefore, the models can be used as design tools for the construction of new devices, maximizing the PCM effectiveness, and thus making a better use of the heat storage system.

6.1 SUGGESTIONS FOR FUTURE WORKS

Future works should explore the critical solidified layer, or thermal barrier layer, using different combinations of PCM and working fluids, in order to investigate the validity of the

correlations presented in this work. Further visualization tests could also provide useful insight into the formation and geometry of the critical layer, especially with the PCM container made with a transparent material, such as glass or acrylic, to allow for observation of the PCM during the tests.

Additionally, different geometries of heat exchanger and PCM container should be designed and tested using the critical solidified layer as an optimization parameter, seeking the ideal ratio of PCM volume per heat exchanger surface area. In particular, a compact heat exchanger, composed of several closed two-phase thermosyphons, immersed in a PCM pool, would feature a large surface area for heat extraction and high thermal conductivity.

REFERENCES

- AL-MUDHAFAR, A. H. N.; NOWAKOWSKI, A. F.; NICOLLEAU, F. C. G. A. Enhancing the thermal performance of PCM in a shell and tube latent heat energy storage system by utilizing innovative fins. **Energy Reports**, v. 7, 2021. 120–126 pp.
- ASHRAE. **ASHRAE Handbook - Fundamentals**, American Society of Heating, Refrigerating, and Air Conditioning Engineers. Atlanta, EUA, 2005.
- BEHI, H.; KARIMI, D.; GANDOMAN, F. H.; AKBARZADEH, M.; KHALEGHI, S.; KALOGIANNIS, T.; HOSEN, M. S.; JAGUEMONT, J.; MIERLO, J. V.; BERECIBAR, M. PCM assisted heat pipe cooling system for the thermal management of an LTO cell for high-current profiles. **Case Studies in Thermal Engineering**, v. 25, 2021, 100920. ISSN 2214-157X, DOI:10.1016/j.csite.2021.100920.
- BEJAN, A. **Convection Heat Transfer**. 4th ed. United States: John Wiley & Sons, 2013. 233 – 241 pp. ISBN 9780470900376, 9781118671627.
- BELLANI, P. L. **Termossifão bifásico em circuito para aquecimento solar residencial**. Dissertation thesis (Masters) – Federal University of Santa Catarina (UFSC), Florianópolis - Brazil, 2017.
- COOLPROP - R141b References**. Available at: <http://www.coolprop.org/fluid_properties/fluids/R141b.html>. Accessed on November 16, 2021.
- CHOI, D. H.; LEE, J.; HONG, H.; KANG, Y. T. Thermal conductivity and heat transfer performance enhancement of phase change materials (PCM) containing carbon additives for heat storage application. **International Journal of Refrigeration**, v. 42, June 2014, 112-120 pp. DOI: 10.1016/j.ijrefrig.2014.02.004.
- DIAO, Y.; QI, N.; WANG, Z.; ZHAO, Y.; CHEN, C.; WANG, Z. **Thermal performance analysis of a solar air collection–cascade storage system integrated with micro-heat pipe arrays**. *Solar Energy*, v. 224, 2021. 1271–1290 pp.
- EPE. **Relatório Síntese do Balanço Energético Nacional 2019: Ano base 2018**. Empresa de Pesquisa Energética. Rio de Janeiro: EPE, 2019.
- FARSI, H.; JOLY, J. L.; MISCEVIC, M.; PLATEL, V.; MAZET, N. An experimental and theoretical investigation of the transient behavior of a two-phase closed thermosyphon, **Applied Thermal Engineering**, v. 23, Issue 15, 2003, 1895-1912 pp. ISSN 1359-4311, DOI: 10.1016/S1359-4311(03)00147-9.
- GIL, A.; PEIRÓ, G.; ORÓ, E.; CABEZA, L. Experimental analysis of the effective thermal conductivity enhancement of PCM using finned tubes in high temperature bulk tanks. **Applied Thermal Engineering**, v. 142, pp. 736-744, 2018.

GIL, A.; MEDRANO, M.; MARTORELL, I.; LÁZARO, A.; DOLADO, P.; ZALBA, B.; CABEZA, L. F. State of the art on high temperature thermal energy storage for power generation. **Renewable and Sustainable Energy Reviews**, v. 14, pp. 31–55, 2010.

GOENFLO, D; KANBE, V.; BIELING, V. Bubble density on surfaces with nucleate boiling—its influence on heat transfer and burnout heat flux at elevated saturation pressures. In: **Proceedings of the 8th international heat transfer conference**, San Francisco, 1986, 1995–2000 pp.

GROLL, M.; ROSLER, S. Operation Principles and Performance of Heat Pipes and Closed Two-Phase Thermosyphons. **Journal of Non-Equilibrium Thermodynamic**, v. 17, 1992, 91–151 pp.

HIGGO, A. R.; ZHANG, T. J. Characterization of a compact organic Rankine cycle prototype for low-grade transient solar energy conversion. **Energy Procedia**, 2015, v. 69(May), 1113–22 pp.

HUANG, Y.; SONG, L.; WU, S.; LIU, X. Investigation on the thermal performance of a multi-tube finned latent heat thermal storage pool. **Applied Thermal Engineering**, Volume 200, 2022, 117658, ISSN 1359-4311.

INCROPERA, F. P.; DEWITT, D. P.; BERGMAN, T. L.; LAVINE, A. S. **Fundamentals of heat and mass transfer**. 7th ed. United States: John Wiley & Sons, 2008. 458-459 pp. ISBN 13 978-0470-50197-9.

JAKOB, U. **6 - Solar cooling technologies**. Renewable Heating and Cooling. Woodhead Publishing, 2016, 119-136 pp. ISBN 9781782422136.

KALOGIROU, S. A. Chapter Five - Solar Water Heating Systems. **Solar Energy Engineering**. Academic Press, 2009, 251–314 pp. ISBN 9780123745019.

KANNAN, K. G.; KAMATCHI, R. Experimental investigation on thermosyphon aid phase change material heat exchanger for electronic cooling applications. **Journal of Energy Storage**, v. 39, 2021, 102649 p.

KAMINAGA, F.; HASHIMOTO, H.; FERROZ, C.; GOTO, K.; MATSUMURA, K. Heat Transfer Characteristics of Evaporation and Condensation in a Two-Phase Closed Thermosyphon, **10th International Heat Pipe Conference**, Stuttgart, Germany, 1997.

KIYOMURA, I. S.; MOGAJI, T. S.; MANETTI, L.L.; CARDOSO, E.M. A predictive model for confined and unconfined nucleate boiling heat transfer coefficient, **Applied Thermal Engineering**, v. 127, 2017, 1274–1284 pp.

KREYSZIG, E. **Advanced Engineering Mathematics**. 10th ed. United States: John Wiley & Sons, 2010.

LIU, H.; WANG, Z.; MA, C. An experimental study on heat transfer characteristics of heat pipe heat exchanger with latent heat storage. Part I: Charging only and discharging only modes. **Energy Conversion and Management**, v. 47, Issues 7–8,

2006, 944-966, pp. ISSN 0196-8904, DOI: 10.1016/j.enconman.2005.06.004.

LUU, M. T.; MILANIB, D.; NOMVARC, M.; ABBASA, A. A design protocol for enhanced discharge exergy in phase change material heat battery. **Applied Energy**, v. 265, 2020.

MACHIDA, H.; SUGAHARA, T.; HIRASAWA, I. (2021). **The moment of initial crystallization captured on functionalized nanoparticles**, *Communications Materials*, 2(1), 2021.DOI:10.1038/s43246-021-00171-w

MADHAV, H. V.; RAGHAVENDRA, V.; KUMAR, P.; AMBIRAJAN, A.; DUTTA, P. Development of a Canister Module For PCM Coupled Heat Pipe in Spacecraft Thermal Management. **IEEE Transactions on Components, Packaging and Manufacturing Technology**, 2021.DOI: 10.1109/TCPMT.2021.3114195.

MALDONADO, J. M.; VEREZ, D.; GARCI, A.; CABEZA, L. F. Comparative study between heat pipe and shell-and-tube thermal energy storage, **Applied Thermal Engineering**, v. 192,2021,116974. ISSN 1359-4311.
<<https://doi.org/10.1016/j.applthermaleng.2021.116974>>.

MANTELLI, M. B. H. **Thermosyphons and Heat Pipes: Theory and Applications**. 1st ed. Switzerland: Springer, 2021.ISBN13 978-3030627720.

MANTELLI, M. B. H. **Tubos de Calor e Termossifões**, Notas de aula em Departamento de Engenharia Mecânica, Universidade Federal de Santa Catarina – UFSC, Florianópolis, 2012.

NITHYANANDAM, K; PITCHUMANI, R. Design of a Latent Thermal Energy Storage System with Embedded Heat Pipes. **Applied Energy**, v. 126, 2014, 266–280 pp.

NIST Livro de Química na Web, SRD 69. NIST – National Institute of Standards and Technology, U.S. Department of Commerce. Gaithersburg, United States, 2021. Available at: <<https://webbook.nist.gov/cgi/cbook.cgi?ID=C91203&Mask=2>>. Accessed on November 16, 2021.

NOIE, S. H; KALAEI, M. H.; KOSHNOODI, M. Experimental investigation of a two phase closed thermosyphon, **7th International Heat Pipe Symposium Proceedings**, Jeju, Korea,2003.

OCHTERBECK, J. M. Heat Pipes, in **Heat Transfer Handbook**. New Jersey, John Wiley & Sons, 2003.

OSHMANN, C.; REA, J.; HARDIN, C.; SINGH, A.; ALLEMAN, J.; OLSEN, M.; GLATZMAIER, G.; PARILLA, P.; SIEGEL, N.; GINLEY, D.; TOBERER, E. S. Demonstration of a thermosyphon thermal valve for controlled extraction of stored solar thermal energy. **AIP Conference Proceedings**, v. 2033, 2018, 09002-1 – 090021-7 pp.

CUNHA, J. P.; EAMES, P. Thermal energy storage for low and medium temperature applications using phase change materials – A review. **Applied Energy**, v. 177, 2016, 227–238 pp.

PEREIRA, E. B.; MARTINS, F. R.; GONÇALVES, A. R.; COSTA, R. S.; LIMA, F. J. L.; RÜTHER, R.; ABREU, S. L.; TIEPOLO, G. M.; PEREIRA, S. V.; SOUZA, J. G. **Atlas brasileiro de energia solar**. 2 ed. São José dos Campos: Instituto Nacional de Pesquisas Espaciais, 2017.

PIZZOLATO, A; SHARMAB, A.; MAUTEB, K.; SCIACOVELLIC, A.; VERDA, V. **Design of effective fins for fast PCM melting and solidification in shell-and-tube latent heat thermal energy storage through topology optimization**. *Applied Energy*, v. 208, pp. 210-227, 2017.

PRUPPACHER, H. R.; KLETT, J. D. **Heterogeneous Nucleation**, *Microphysics of Clouds and Precipitation*, v. 18, 2010, ISBN : 978-0-7923-4211-3

REAY, D.A.; KEW, P. A.; MCGLEAN, R. J. **Heat Pipes: Theory, Design and Applications**. 6th ed. Edition, Elsevier, 2014.

ROBAK, C. W.; BERGMAN, T. L.; FAGHRI, A. Enhancement of latent heat energy storage using embedded heat pipes. **International Journal of Heat and Mass Transfer**, v.54, 2011, 3476–3484, pp.

SAYEEF, S.; HESLOP, S.; CORNFORTH, D.; MOORE, T.; PERCY, S.; WARD, J.; BERRY, A.; ROWE, D. **Solar intermittency: Australia’s clean energy challenge**. Australian Solar Institute, 2012.

SHARMA, S. D.; KITANO, H.; SAGARA, K. Phase change materials for low temperature solar thermal applications. **Res. Rep. Fac. Eng. Mie Univ**, v. 29, n. 1, p. 31-64, 2004.

SILVA, R. C.; NETO, I. M.; SEIFERT, S. S. Electricity supply security and the future role of renewable energy sources in Brazil. **Renewable and Sustainable Energy Reviews**, v. 59, 2016, pp. 328–341.

SPARROW, E. M.; ABRAHAM, J. P.; TONG, J. C. K. Archival correlations for average heat transfer coefficients for non-circular and circular cylinders and for spheres in cross-flow. **International Journal of Heat and Mass Transfer**, v. 47, 2004. 5285–529 pp.

SPIEGEL, M. R.; LIPSCHUTZ, S.; LIU, J. **Mathematical Handbook of Formulas and Tables**. 3rd ed. United States: McGraw Hill, 2009. 153 p.

STEINMANN, W. D. “Thermal energy storage systems for concentrating solar power (CSP) plants”, in **Concentrating Solar Power Technology: Principles, Developments and Applications**. Lovegrove, K.; Stein, W. Elsevier, 2012, pp. 362–394.

XIANG H.; CHUQIAO Z.; YAXUE L.; GUIYIN F. Thermal properties and applications of microencapsulated PCM for thermal energy storage: A review. **Applied Thermal Engineering**, v. 147, 2019, 841-855 pp.

YANG, L.; PENG, H.; LING, X.; DONG, H. Numerical analysis on performance of naphthalene phase change thermal storage system in aluminum plate-fin unit. **Heat and Mass Transfer**, v. 51, 2015. DOI: 10.1007/s00231-014-1400-7.

APPENDIX A

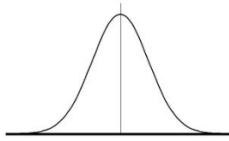

This appendix presents the uncertainty analysis of the experimental data obtained in this study, identifying the input parameters with their respective uncertainties and calculating their influence on the calculated variables. This was made using the uncertainty propagation techniques recommended by the Joint Committee for Guides in Metrology (JCGM, 2008).

A.1 MEASUREMENT UNCERTAINTY

The result of a measurement represents only an estimate of the true value of the measured quantity, due to both random and systematic effects that cause errors. Therefore, such a result is only complete when it is accompanied by its associated uncertainty, which is the statistical dispersion of values attributed to the measured quantity (JCGM, 2008).

The standard uncertainty, u , of a quantity that varies randomly can be obtained using either a type A or a type B evaluation. A type A evaluation uses the experimental standard deviation of a series of measurements to obtain the uncertainty, while a type B evaluation uses a single measurement and a pool of available data such as manufacturer's manuals, calibration certificates or reference data from handbooks. Most of the measured quantities in this study varied over time, and could only be measured once before changing, therefore requiring the type B evaluation of uncertainty. Depending on the type of measurement, different probability distribution functions are used to determine the standard uncertainty, where the two most common distributions are shown in Table A.1.

Table A.1 – Most common types of probability distribution and their application. Adapted from HOGAN, 2015.

Type of evaluation	Probability distribution	Standard uncertainty, u	Application
A	Normal 	$u = \frac{\sigma}{\sqrt{n}}$	Series of n repeated measurements, with standard deviation σ .
B	Rectangular 	$u = \frac{a}{\sqrt{3}}$	Single measurement with a digital display or unknown data distribution, with known maximum and minimum values ($\pm a$).

When a measurement is the result of a combination of n measuring devices, it carries a combined standard uncertainty, u_c , from the uncertainty associated with each device, u_i , expressed as Eq. (A.1). Similarly, when a variable is not the result of a direct measurement, but is instead calculated from other uncorrelated measured quantities, it also carries a combined standard uncertainty expressed in Eq. (A.2), where x_i is a measured quantity and f is the function that relates the desired variable to that measurement.

$$u_c^2 = \sum_{i=1}^n u_i^2 \quad (\text{A.1})$$

$$u_c^2(f) = \sum_{i=1}^n \left(\frac{\partial f}{\partial x_i} \right)^2 u_i^2(x_i) \quad (\text{A.2})$$

The last concept needed for this analysis is that of expanded uncertainty, U , which encompasses an interval around the measurement result that contains a large portion of the probability distribution, with a level of confidence level p . The expanded uncertainty is defined in Eq. (A.3), where k_p is a coverage factor associated with the confidence level p . In this study, this factor is obtained as $k_p = 2,00$ from the t-Student table for a confidence level $p = 95,45$ %.

$$U = u_c k_p \quad (\text{A.3})$$

Once the uncertainty analysis for each variable, y , is complete, the result is expressed as $y \pm U$. The next sections present the results for the uncertainty analysis of directly measured quantities, and for quantities calculated from these measurements.

A.1.1 DIRECT MEASUREMENTS

Among the experimental data in this study, five variables were the result of direct measurements: temperature, air velocity in the wind tunnel, current and tension provided by the DC power source, and length. These measurements and their uncertainty information are discussed in this section.

a) Length

The length of the PCM containers and of each section of the thermosyphon were measured using a steel ruler, with a minimal resolution of 1 mm. Therefore, its expanded uncertainty can be assumed as $U(l) = \pm 0,5$ mm due to lack of visible markers between millimeters, and the standard uncertainty $u(l)$ can be obtained from Eq. (A.3), using the $k_p = 2,00$. Therefore, the uncertainty of length measurements in this study is $u(l) = \pm 0,25$ mm.

b) Temperature

The temperature values used in this study were obtained as a direct measurement using K-type thermocouples connected to a Campbell Scientific CR1000 datalogger, via an AM25T Multiplexer. Each of these components carries an uncertainty u_i , so that the combined uncertainty for the temperature measurement, $u_c(T)$, is obtained from Eq. (A.1). The measuring devices are digital, with rectangular improbability distributions, as seen in Table , and since the temperature varied over time, its instant value was obtained from a single measurement, constituting a type B evaluation. The resulting uncertainty evaluation for temperature is seen in Table A.2.

Table A.2 – Uncertainty analysis for temperature measurements.

Symbol	Description	a [°C]	Distribution	Resulting uncertainty [°C]
u_1	K-type thermocouple	1,1	Rectangular	0,32
u_2	AM25T multiplexer	0,4	Rectangular	0,12
u_3	CR1000 datalogger	0,8	Rectangular	0,23
$u_c(T)$	Combined uncertainty	-	-	0,41
$U(T)$	Expanded uncertainty	-	-	0,82

c) Air velocity in the wind tunnel

As discussed in section 3.2.1, the mean air velocity, v_∞ , in the wind tunnel for each set frequency was measured using a pitot tube and following the traverse method, as recommended by ASHRAE (2005). A total of six points along the diameter of the wind tunnel were measured, each of them four times. Then, the average and standard deviation were obtained for each point, and the mean velocity was obtained as the arithmetic average of these

six points. Therefore, the uncertainty of v_∞ is obtained from a series of measurements and their standard deviation, constituting a type A evaluation. The direct measurements can be seen in Table A.3, where f is the frequency set at the inverter, μ is the average of $n = 4$ measurements, and u_i is the resulting uncertainty of the measured point i . Then, the resulting analysis is summarized in

A.4, where an additional frequency $f = 45$ Hz is shown, obtained as the average of the frequencies $f = 40$ Hz and $f = 50$ Hz.

Table A.3 – Uncertainty analysis for air velocity measurements, with $n = 4$ measurements for each point.

f (Hz)	Symbol	Description	Distribution	μ_i [m/s]	σ_i [m/s]	u_i [m/s]
20	$i = 1$	Point 1	Normal	3,78	0,15	0,07
	$i = 2$	Point 2	Normal	4,49	0,00	0,00
	$i = 3$	Point 3	Normal	4,63	0,05	0,03
	$i = 4$	Point 4	Normal	4,59	0,05	0,02
	$i = 5$	Point 5	Normal	4,40	0,05	0,02
	$i = 6$	Point 6	Normal	3,84	0,15	0,07
30	$i = 1$	Point 1	Normal	5,91	0,04	0,02
	$i = 2$	Point 2	Normal	6,96	0,11	0,06
	$i = 3$	Point 3	Normal	7,19	0,03	0,02
	$i = 4$	Point 4	Normal	7,08	0,08	0,04
	$i = 5$	Point 5	Normal	6,77	0,13	0,06
	$i = 6$	Point 6	Normal	5,87	0,19	0,09
40	$i = 1$	Point 1	Normal	7,73	0,08	0,04
	$i = 2$	Point 2	Normal	8,92	0,10	0,05
	$i = 3$	Point 3	Normal	9,31	0,02	0,01
	$i = 4$	Point 4	Normal	9,24	0,07	0,03
	$i = 5$	Point 5	Normal	8,80	0,08	0,04
	$i = 6$	Point 6	Normal	7,70	0,13	0,07
50	$i = 1$	Point 1	Normal	9,49	0,13	0,07
	$i = 2$	Point 2	Normal	10,97	0,19	0,10
	$i = 3$	Point 3	Normal	11,42	0,13	0,06
	$i = 4$	Point 4	Normal	11,40	0,04	0,02

	$i = 5$	Point 5	Normal	11,01	0,18	0,09
	$i = 6$	Point 6	Normal	9,60	0,14	0,07
60	$i = 1$	Point 1	Normal	11,18	0,24	0,12
	$i = 2$	Point 2	Normal	12,84	0,27	0,13
	$i = 3$	Point 3	Normal	13,34	0,16	0,08
	$i = 4$	Point 4	Normal	13,36	0,06	0,03
	$i = 5$	Point 5	Normal	12,93	0,13	0,07
	$i = 6$	Point 6	Normal	11,33	0,12	0,06

Table A.4 – Uncertainty analysis for mean air velocity, based on the results from Table A.3.

Set frequency (Hz)	Mean velocity, v_{∞} [m/s]	Symbol	Description	Resulting uncertainty, [m/s]
20	4,45	$u_c(v_{\infty})$	Combined uncertainty	0,11
		$U(v_{\infty})$	Expanded uncertainty	0,22
30	6,84	$u_c(v_{\infty})$	Combined uncertainty	0,13
		$U(v_{\infty})$	Expanded uncertainty	0,27
40	8,86	$u_c(v_{\infty})$	Combined uncertainty	0,11
		$U(v_{\infty})$	Expanded uncertainty	0,22
45	9,94	$u_c(v_{\infty})$	Combined uncertainty	0,21
		$U(v_{\infty})$	Expanded uncertainty	0,41
50	10,99	$u_c(v_{\infty})$	Combined uncertainty	0,18
		$U(v_{\infty})$	Expanded uncertainty	0,36
60	12,93	$u_c(v_{\infty})$	Combined uncertainty	0,22
		$U(v_{\infty})$	Expanded uncertainty	0,44

d) Electric current and tension

The values of electric current, i , and tension, V , were obtained directly from the display of the DC power source, MCE-1310. The uncertainty of each variable according to the manufacturer was of $\pm 1\%$ of the displayed value (MCE, 2005), with a rectangular distribution due to the digital nature of the display. Since the electric resistance of the tested device, R_{el} , attached to this power source was constant, each set value of current corresponded to a set value of tension, due to Ohm's law seen in Eq. (A.4). Therefore, the studied values of V and i are shown in pairs on Table A.5, along with their uncertainty analysis.

$$V = R_{el} \times i \quad (\text{A.4})$$

Table A.5 – Uncertainty analysis for current and tension displayed in the DC power source.

Displayed value	Symbol	Description	a	Distribution	Resulting uncertainty
$i = 0,66 \text{ A}$	$u_1(i)$	Tension standard uncertainty	0,01	Rectangular	0,00 [A]
$V = 37,9 \text{ V}$	$u_1(V)$	Current standard uncertainty	0,4	Rectangular	0,1 [V]
$i = 1,00 \text{ A}$	$u_2(i)$	Tension standard uncertainty	0,01	Rectangular	0,00 [A]
$V = 40,2 \text{ V}$	$u_2(V)$	Current standard uncertainty	0,4	Rectangular	0,1 [V]
$i = 0,94 \text{ A}$	$u_3(i)$	Tension standard uncertainty	0,01	Rectangular	0,00 [A]
$V = 53,3 \text{ V}$	$u_3(V)$	Current standard uncertainty	0,5	Rectangular	0,2 [V]
$i = 1,02 \text{ A}$	$u_4(i)$	Tension standard uncertainty	0,01	Rectangular	0,00 [A]
$V = 58,6 \text{ V}$	$u_4(V)$	Current standard uncertainty	0,6	Rectangular	0,2 [V]
$i = 1,11 \text{ A}$	$u_5(i)$	Tension standard uncertainty	0,01	Rectangular	0,00 [A]
$V = 63,5 \text{ V}$	$u_5(V)$	Current standard uncertainty	0,6	Rectangular	0,2 [V]
$i = 1,18 \text{ A}$	$u_6(i)$	Tension standard uncertainty	0,01	Rectangular	0,00 [A]
$V = 67,8 \text{ V}$	$u_6(V)$	Current standard uncertainty	0,7	Rectangular	0,2 [V]

A.1.2 INDIRECT MEASUREMENTS

Several experimental variables used in this study were indirectly obtained as functions of the direct measurements from the previous section, and their uncertainties in turn were calculated using Eq. (A.2). These variables are listed as: electric power from the DC power source, P_{el} , Reynolds and Nusselt numbers for the air flow in the wind tunnel, Re and Nu , respectively, and experimental thermal resistances on the evaporator and PCM container, R_e and R_{PCM} respectively. Their uncertainty analysis is detailed in the following topics.

a) Electric power

The electric power, P_{el} , provided to the electric resistance that heats the thermal system, is calculated directly from the displayed values of V and i , using Eq. (A.5). Therefore, the combined standard uncertainty, u_c , for P_{el} is obtained from Eq. (A.6), where the relevant partial derivatives are shown in Eq. (A.7) and Eq. (A.8), and the uncertainties $u(i)$ and $u(V)$ were obtained from the previous analysis. The resulting uncertainty analysis can be seen in Table A.6, with the expanded uncertainty being shown as an absolute value and as a percentage of the result, in parenthesis.

$$P_{el} = i \times V \quad (A.5)$$

$$u_c(P_{el}) = \sqrt{\left[\frac{\partial P_{el}}{\partial i} u(i)\right]^2 + \left[\frac{\partial P_{el}}{\partial V} u(V)\right]^2} \quad (A.6)$$

$$\frac{\partial P_{el}}{\partial i} = V \quad (A.7)$$

$$\frac{\partial P_{el}}{\partial V} = i \quad (A.8)$$

Table A.6 – Uncertainty analysis for current and tension displayed in the DC power source.

Power value, P_{el} [W]	Combined standard uncertainty,	Expanded uncertainty,
	$u_c(P_{el})$ [W]	$U(P_{el})$ [W]
25,0	$\pm 0,1$	$\pm 0,2(\pm 1 \%)$
40,2	$\pm 0,1$	$\pm 0,3(\pm 1 \%)$
50,1	$\pm 0,2$	$\pm 0,4(\pm 1 \%)$
59,8	$\pm 0,2$	$\pm 0,5(\pm 1 \%)$
70,5	$\pm 0,3$	$\pm 0,6(\pm 1 \%)$
80,0	0,3	0,7($\pm 1 \%$)

b) Reynolds number

The Reynolds number for the air flow in the wind tunnel, Re_∞ , is given by Eq. (A.9), where d_e is the external diameter of the closed thermosyphon's condenser, v_∞ was obtained from direct measurements as shown in previous sections, and ν is the cinematic viscosity of air at temperature T_∞ . The value for the diameter d_e is fixed by the manufacturer as $d_e = 1''$ (or 25,4 mm), and was not subjected to an uncertainty analysis. Therefore, the combined uncertainty for Re_∞ , $u_c(Re_\infty)$, is obtained from Eq. (A.10), where the necessary derivatives are detailed in Eq.(A.11) and Eq. (A.12).

$$Re_\infty = \frac{v_\infty d_e}{\nu} \quad (\text{A.9})$$

$$u_c(Re_\infty) = \sqrt{\left[\frac{\partial Re_\infty}{\partial v_\infty} u(v_\infty)\right]^2 + \left[\frac{\partial Re_\infty}{\partial \nu} u(\nu)\right]^2} \quad (\text{A.10})$$

$$\frac{\partial Re_\infty}{\partial v_\infty} = \frac{Re_\infty}{v_\infty} \quad (\text{A.11})$$

$$\frac{\partial Re_\infty}{\partial \nu} = \frac{-Re_\infty}{\nu} \quad (\text{A.12})$$

The uncertainty of air viscosity, $u(\nu)$, is not known, but it is a function of temperature. Therefore, it was obtained as Eq. (A.13), where the derivative $\frac{\partial \nu}{\partial T}$ is approximated as Eq. (A.14), using a small temperature interval, $\Delta T = 1$ °C, surrounding the measured air temperature T_∞ .

$$u(\nu) = \frac{\partial \nu}{\partial T} u(T) \quad (\text{A.13})$$

$$\frac{\partial \nu}{\partial T} = \frac{\nu(T + \Delta T) - \nu(T - \Delta T)}{2\Delta T} \quad (\text{A.14})$$

The uncertainty analysis results for Re_∞ relative to the main experiment are detailed in Table A.7, with the expanded uncertainty being shown as an absolute value and as a percentage of the result, in parenthesis.

Table A.7 – Uncertainty analysis for Reynolds at air temperature, Re_∞ for the values pertaining to the main experiment.

Reynolds, Re_∞	Variables, x_i	Partial derivatives, $\frac{\partial Re_\infty}{\partial x_i}$	Standard uncertainties, $u(x_i)$	Combined uncertainty, $u_c(Re_\infty)$	Expanded uncertainty, $U(Re_\infty)$
7323	ν_∞	$1,65 \times 10^3$	0,11	± 185	± 369 (± 5 %)
	ν	$-4,75 \times 10^8$	$3,81 \times 10^{-8}$		
11134	ν_∞	$1,63 \times 10^3$	0,13	± 221	± 443 (± 4 %)
	ν	$-7,14 \times 10^8$	$3,82 \times 10^{-8}$		
16246	ν_∞	$1,63 \times 10^3$	0,21	± 339	± 677 (± 4 %)
	ν	$-1,05 \times 10^9$	$3,82 \times 10^{-8}$		
21185	ν_∞	$1,64 \times 10^3$	0,22	± 362	± 725 (± 3 %)
	ν	$-1,37 \times 10^9$	$3,81 \times 10^{-8}$		

c) Experimental Nusselt number

The experimental Nusselt number related to heat transfer from the thermosyphon to the wind tunnel, $\overline{Nu}_{d,exp}$, from section 3.2.1 can be calculated from experimental data using Eq. (3.7), as a function of the power supplied, P_{el} , the condenser length, l_c , the temperatures of air and the condenser wall, T_∞ and T_c respectively, and the air conductivity, k_{air} , obtained at T_∞ . Therefore, the combined uncertainty for $\overline{Nu}_{d,exp}$, $u_c(\overline{Nu}_{d,exp})$, is obtained from Eq. (A.15), where the terms of the sum are described in Eq. (A.16), and the necessary derivatives are detailed in Eq. (A.18), Eq. (A.19), Eq. (A.22), Eq. (A.23) and Eq. (A.21).

$$u_c(\overline{Nu}_{d,exp}) = \sqrt{\sum_{i=1}^5 \left[\frac{\partial \overline{Nu}_{d,exp}}{\partial x_i} u(x_i) \right]^2} \quad (\text{A.15})$$

$$\begin{aligned} \sum_{i=1}^5 \left[\frac{\partial \overline{Nu}_{d,exp}}{\partial x_i} u(x_i) \right]^2 &= \left[\frac{\partial \overline{Nu}_{d,exp}}{\partial P_{el}} u(P_{el}) \right]^2 + \left[\frac{\partial \overline{Nu}_{d,exp}}{\partial l_c} u(l) \right]^2 \\ &+ \left[\frac{\partial \overline{Nu}_{d,exp}}{\partial T_\infty} u(T) \right]^2 + \left[\frac{\partial \overline{Nu}_{d,exp}}{\partial T_c} u(T) \right]^2 \\ &+ \left[\frac{\partial \overline{Nu}_{d,exp}}{\partial k_{air}} u(k_{air}) \right]^2 \end{aligned} \quad (\text{A.16})$$

$$\frac{\partial \overline{Nu}_{d,exp}}{\partial l_c} = \frac{1}{\pi l_c k_{air} (T_c - T_\infty)} \quad (\text{A.17})$$

$$\frac{\partial \overline{Nu}_{d,exp}}{\partial l_c} = \frac{-\overline{Nu}_{d,exp}}{l_c} \quad (\text{A.18})$$

$$\frac{\partial \overline{Nu}_{d,exp}}{\partial T_\infty} = \frac{\overline{Nu}_{d,exp}}{(T_c - T_\infty)} \quad (\text{A.19})$$

$$\frac{\partial \overline{Nu}_{d,exp}}{\partial T_c} = \frac{-\overline{Nu}_{d,exp}}{(T_c - T_\infty)} \quad (\text{A.20})$$

$$\frac{\partial \overline{Nu}_{d,exp}}{\partial k_{air}} = \frac{-\overline{Nu}_{d,exp}}{k_{air}} \quad (\text{A.21})$$

The uncertainty of air conductivity, $u(k_{air})$, is not known, but it is a function of temperature. Therefore, it was obtained similarly to that of air viscosity, as Eq.(A.22), where the derivative $\frac{\partial k_{air}}{\partial T}$ is approximated as Eq.(A.23), using a small temperature interval, $\Delta T = 1$ °C, surrounding the measured air temperature T_{∞} .

$$u(k_{air}) = \frac{\partial k_{air}}{\partial T} u(T) \quad (\text{A.22})$$

$$\frac{\partial k_{air}}{\partial T} = \frac{k_{air}(T + \Delta T) - k_{air}(T - \Delta T)}{2\Delta T} \quad (\text{A.23})$$

The uncertainty analysis results for $\overline{Nu}_{d,exp}$ relative to the main experiment are detailed in Table A.8, with the expanded uncertainty being shown as an absolute value and as a percentage of the result, in parenthesis.

Table A.8 – Uncertainty analysis for experimental Nusselt, $\overline{Nu}_{d,exp}$, for the values pertaining to the main experiment.

Experimental Nusselt, $\overline{Nu}_{d,exp}$	Variables, x_i	Partial derivatives, $\frac{\partial \overline{Nu}_{d,exp}}{\partial x_i}$	Standard uncertainties, $u(x_i)$	Combined uncertainty, $u_c(\overline{Nu}_{d,exp})$	Expanded uncertainty, $U(\overline{Nu}_{d,exp})$
119,1	P_{el} [W]	2,38	0,20	$\pm 1,4$	$\pm 2,9$ ($\pm 2\%$)
	l_c [m]	$-1,23 \times 10^3$	$2,5 \times 10^{-4}$		
	T_∞ [°C]	2,26	0,69		
	T_c [°C]	-2,26	0,69		
	k_{air} [W/(m.°C)]	$-4,56 \times 10^3$	$3,1 \times 10^{-5}$		
142,2	P_{el} [W]	2,37	0,24	$\pm 1,7$	$\pm 3,4$ ($\pm 2\%$)
	l_c [m]	$-1,47 \times 10^3$	$2,5 \times 10^{-4}$		
	T_∞ [°C]	2,70	0,69		
	T_c [°C]	-2,70	0,69		
	k_{air} [W/(m.°C)]	$-5,42 \times 10^3$	$3,0 \times 10^{-5}$		
163,2	P_{el} [W]	2,33	0,29	$\pm 1,9$	$\pm 3,9$ ($\pm 2\%$)
	l_c [m]	$-1,68 \times 10^3$	$2,5 \times 10^{-4}$		
	T_∞ [°C]	3,04	0,69		
	T_c [°C]	-3,04	0,69		
	k_{air} [W/(m.°C)]	$-6,23 \times 10^3$	$3,0 \times 10^{-5}$		
191,6	P_{el} [W]	2,39	0,33	$\pm 2,3$	$\pm 4,7$ ($\pm 2\%$)
	l_c [m]	$-1,97 \times 10^3$	$2,5 \times 10^{-4}$		
	T_∞ [°C]	3,66	0,69		
	T_c [°C]	-3,66	0,69		
	k_{air} [W/(m.°C)]	$-7,32 \times 10^3$	$3,0 \times 10^{-5}$		

d) Experimental thermal resistances

The baseline experimental values for steady state thermal resistance of the PCM container, $R_{PCM,exp}$ were obtained from Eq. (A.24), while the baseline experimental resistance of the thermosyphon evaporator, $R_{e,exp}$, was obtained from Eq. (A.25), as functions of the power supplied to the device, P_{el} , and the average PCM, evaporator and adiabatic section temperatures, T_{PCM} , T_e , and T_a respectively. Therefore, the combined uncertainty for $R_{PCM,exp}$, $u_c(R_{PCM,exp})$, is obtained from Eq. (A.26), and the combined uncertainty for $R_{e,exp}$, $u_c(R_{e,exp})$, is obtained from Eq. (A.27), where the necessary partial derivatives are detailed in Eq. (A.28), Eq. (A.29), Eq. (A.30), and Eq. (A.31).

$$R_{PCM,exp} = \frac{T_{PCM} - T_e}{P_{el}} \quad (A.24)$$

$$R_{e,exp} = \frac{T_e - T_a}{P_{el}} \quad (A.25)$$

$$u_c(R_{PCM,exp}) = \left[\frac{\partial R_{PCM,exp}}{\partial T_{PCM}} u(T) \right]^2 + \left[\frac{\partial R_{PCM,exp}}{\partial T_e} u(T) \right]^2 + \left[\frac{\partial R_{PCM,exp}}{\partial P_{el}} u(P_{el}) \right]^2 \quad (A.26)$$

$$u_c(R_{e,exp}) = \left[\frac{\partial R_{e,exp}}{\partial T_e} u(T) \right]^2 + \left[\frac{\partial R_{e,exp}}{\partial T_a} u(T) \right]^2 + \left[\frac{\partial R_{e,exp}}{\partial P_{el}} u(P_{el}) \right]^2 \quad (A.27)$$

$$\frac{\partial R_{PCM,exp}}{\partial T_{PCM}} = \frac{\partial R_{e,exp}}{\partial T_e} = \frac{1}{P_{el}} \quad (A.28)$$

$$\frac{\partial R_{PCM,exp}}{\partial T_e} = \frac{\partial R_{e,exp}}{\partial T_a} = -\frac{1}{P_{el}} \quad (A.29)$$

$$\frac{\partial R_{PCM,exp}}{\partial P_{el}} = -\frac{R_{PCM,exp}}{P_{el}} \quad (A.30)$$

$$\frac{\partial R_{e,exp}}{\partial P_{el}} = -\frac{R_{e,exp}}{P_{el}} \quad (\text{A.31})$$

The uncertainty analysis results for $R_{PCM,exp}$ relative to the main experiment are detailed in Table A.9 and for $R_{e,exp}$ in Table A.10, where all twelve tests are shown due to the impact of PCM container size on the overall resistances, with the expanded uncertainty being shown as an absolute value and as a percentage of the result, in parenthesis.

Table A.9 – Uncertainty analysis for experimental thermal resistance $R_{PCM,exp}$, for all tests pertaining to the main experiment.

PCM container	Test	$R_{PCM,exp}$ $\times 10^{-2}$ [°C/W]	$\frac{\partial R_{PCM,exp}}{\partial P_{el}}$ $\times 10^{-3}$	$\left[\frac{\partial R_{PCM,exp}}{\partial T_{PCM}} \right]$ $= -\frac{\partial R_{PCM,exp}}{\partial T_e}$ $\times 10^{-2}$	$u_c(R_{PCM,ex})$ $\times 10^{-2}$ [°C/W]	$U(R_{PCM,exp})$ $\times 10^{-2}$ [°C/W]	
A	13	18	-3,7	2,0	±1,2	±2,3	(±13 %)
	14	17	-2,8	1,7	±0,97	±1,9	(±12 %)
	15	17	-2,4	1,4	±0,82	±1,6	(±10 %)
	16	17	-2,1	1,2	±0,72	±1,4	(±9 %)
B	17	21	-4,1	2,0	±1,2	±2,3	(±11 %)
	18	20	-3,4	1,7	±0,97	±1,9	(±10 %)
	19	20	-2,8	1,4	±0,82	±1,6	(±8 %)
	20	19	-2,4	1,2	±0,72	±1,4	(±7 %)
C	21	23	-4,6	2,0	±1,2	±2,3	(±10 %)
	22	22	-3,8	1,7	±0,97	±1,9	(±9 %)
	23	22	-3,2	1,4	±0,82	±1,6	(±7 %)
	24	22	-2,7	1,2	±0,72	±1,4	(±7 %)

Table A.10 – Uncertainty analysis for experimental thermal resistance $R_{e,exp}$, for all tests pertaining to the main experiment.

PCM container	Test	$R_{e,exp}$ $\times 10^{-2}$ [°C/W]	$\frac{\partial R_{e,exp}}{\partial P_{el}}$ $\times 10^{-4}$	$\left[\frac{\partial R_{e,exp}}{\partial T_e} = - \frac{\partial R_{e,exp}}{\partial T_a} \right]$ $\times 10^{-2}$	$u_c(R_{e,exp})$ $\times 10^{-2}$ [°C/W]	$U(R_{e,exp})$ $\times 10^{-2}$ [°C/W]	
A	13	6,7	-13	2,0	$\pm 1,2$	$\pm 2,3$	(± 34 %)
	14	5,6	-9,3	1,7	$\pm 0,97$	$\pm 1,9$	(± 35 %)
	15	6,0	-8,6	1,4	$\pm 0,82$	$\pm 1,6$	(± 27 %)
	16	5,7	-7,2	1,2	$\pm 0,72$	$\pm 1,4$	(± 25 %)
B	17	8,2	-16	2,0	$\pm 1,2$	$\pm 2,3$	(± 28 %)
	18	8,2	-14	1,7	$\pm 0,97$	$\pm 1,9$	(± 24 %)
	19	7,4	-10	1,4	$\pm 0,82$	$\pm 1,6$	(± 22 %)
	20	7,2	-8,9	1,2	$\pm 0,72$	$\pm 1,4$	(± 20 %)
C	21	5,4	-11	2,0	$\pm 1,2$	$\pm 2,3$	(± 42 %)
	22	5,8	-9,8	1,7	$\pm 0,97$	$\pm 1,9$	(± 33 %)
	23	5,8	-8,2	1,4	$\pm 0,82$	$\pm 1,6$	(± 29 %)
	24	6,0	-7,5	1,2	$\pm 0,72$	$\pm 1,4$	(± 24 %)

REFERENCES FOR APPENDIX A

ALBERTAZZI, Armando; SOUSA, André R. de. **Fundamentos de Metrologia Científica e Industrial**. 1st ed. Brazil: Manole, 2008.

ASHRAE. **ASHRAE Handbook - Fundamentals**, American Society of Heating, Refrigerating, and Air Conditioning Engineers. Atlanta, EUA, 2005.

HOGAN, Richard. **Probability Distributions for Measurement Uncertainty**.

2015. Available at:

<<https://www.isobudgets.com/probability-distributions-for-measurement-uncertainty/>>.

Accessed on: November 17, 2021.

JCGM 100:2008. **Evaluation of measurement data** — Guide to the expression of uncertainty in measurement. Joint Committee for Guides in Metrology, 2008.

INMETRO. **Avaliação de dados de medição - Guia para a expressão de incerteza de medição – GUM 2008**. Available at:

<http://www.inmetro.gov.br/inovacao/publicacoes/gum_final.pdf>. Accessed on: November 17, 2021.

MICROTÉCNICA SISTEMAS DE ENERGIA - MCE. **Catálogo de Variáveis Digitais - Saída simples / dupla. 2020**. Available at:

<[https://www.mctecnica.com.br/gerenciarportal/area-](https://www.mctecnica.com.br/gerenciarportal/area-adm/produto/0.220342001592309856.htm)

[adm/produto/0.220342001592309856.htm](https://www.mctecnica.com.br/gerenciarportal/area-adm/produto/0.220342001592309856.htm)>. Accessed on: November 19, 2021.

CAMPBELL SCIENTIFIC. **Instruction Manual - AM25T Solid-State Thermocouple Multiplexer**. 2017. Available at:

<https://s.campbellsci.com/documents/ca/manuals/am25t_man.pdf>. Accessed on: November 19, 2021.

CAMPBELL SCIENTIFIC. **Operator's Manual - CR1000 Datalogger**. 2018. Available at:

<<https://s.campbellsci.com/documents/us/manuals/cr1000.pdf>>. Accessed on: November 19, 2021.

OMEGA. **Códigos de Cores e Limites de Erro**. 2015a. Available at:

<<https://br.omega.com/techref/colorcodes.html>>. Accessed on: November 19, 2021.

APPENDIX B

This appendix presents the experimental results of temperature as a function of time for the remaining tests that were omitted from Chapter 5.

B.1 BASELINE EXPERIMENT

Further test results mentioned in Section 3.2.3 are presented in Figures B.1 to B.4.

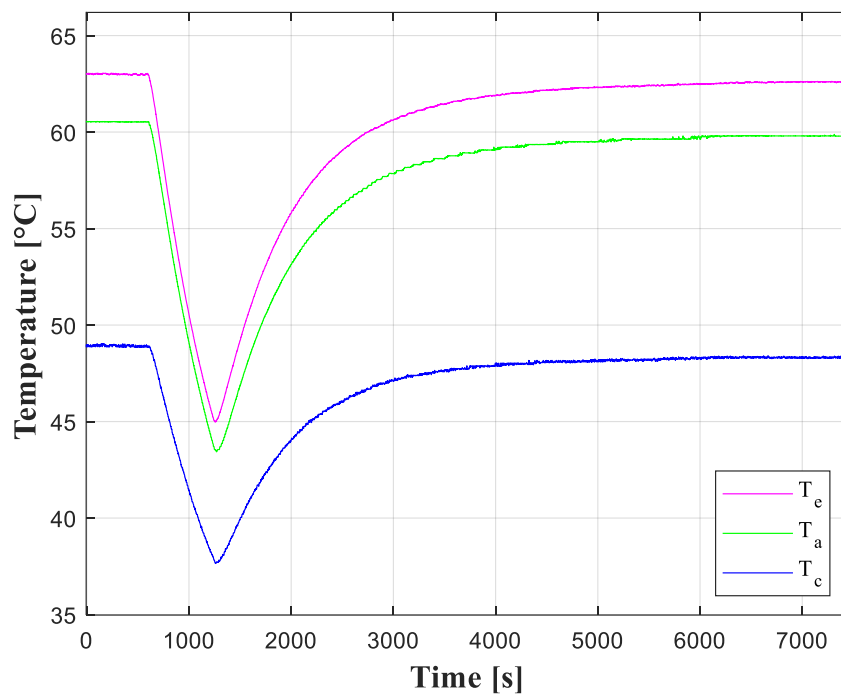


Figure B.1. Temperatures as a function of time for Test 8 (Table 3.4).

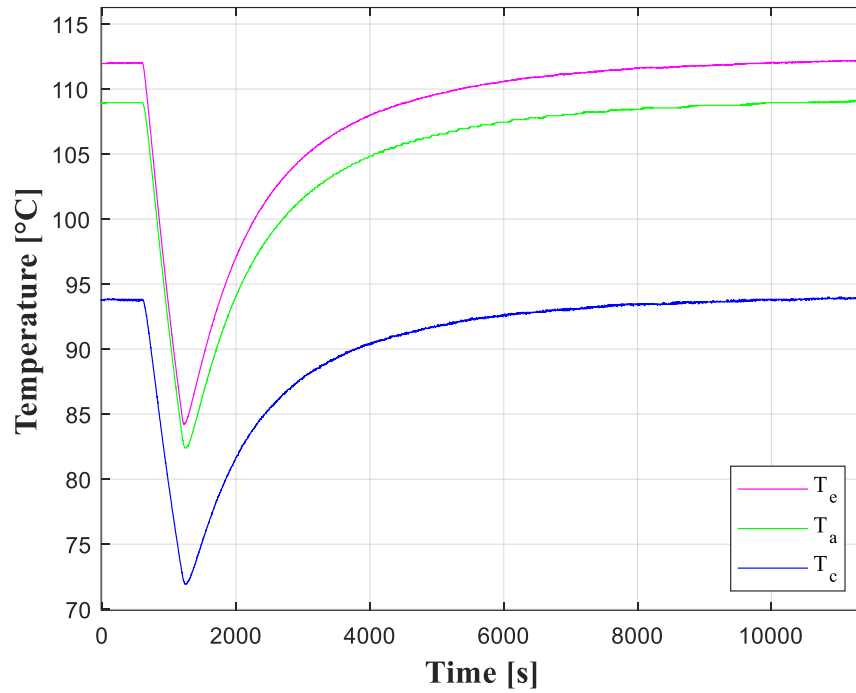


Figure B.2. Temperatures as a function of time for Test 9 (Table 3.4).

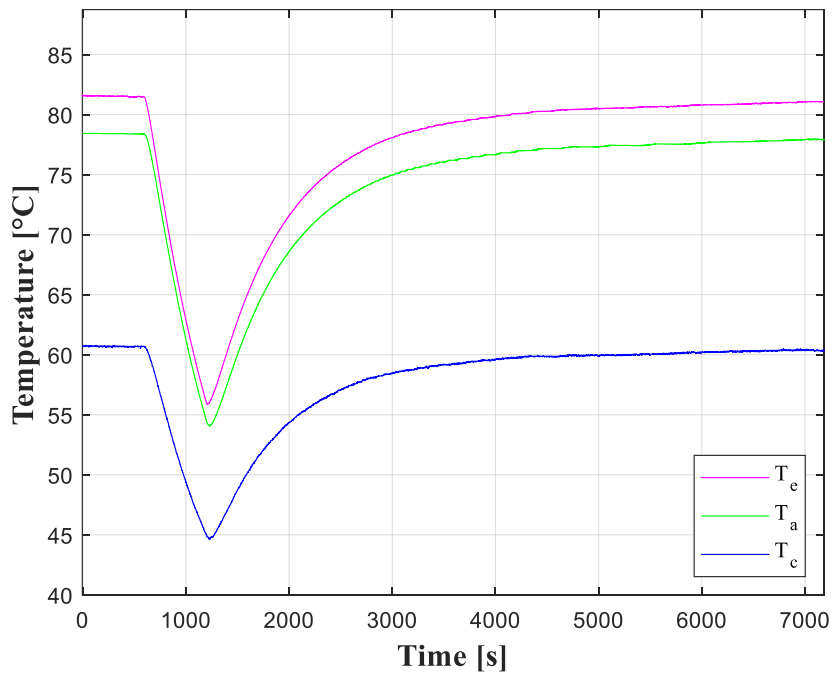


Figure B.3. Temperatures as a function of time for Test 10 (Table 3.4).

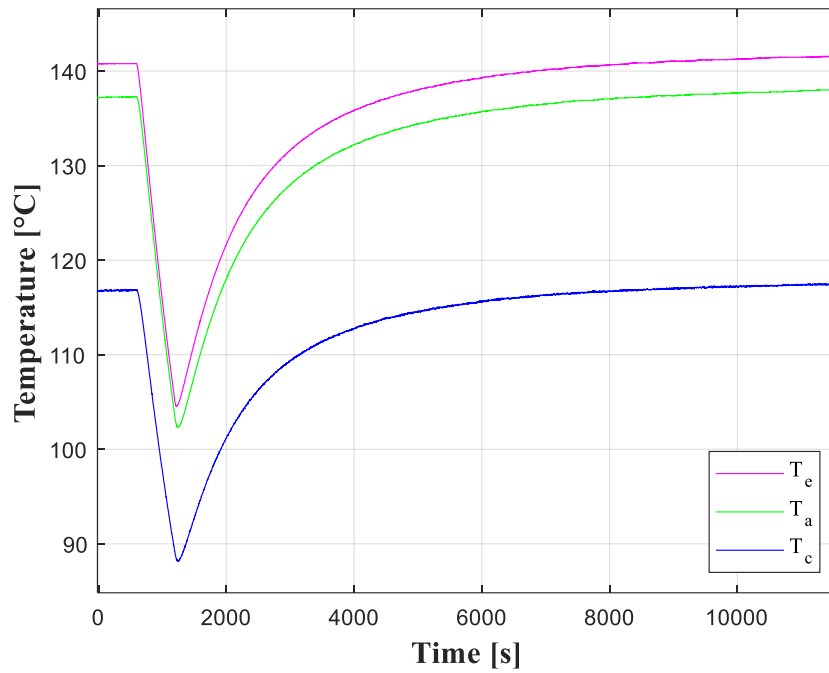


Figure B.4. Temperatures as a function of time for Test 11 (Table 3.4).

B.2 MAIN EXPERIMENT

Further tests results mentioned in Section 5.1.4 are presented in Figures B.5 to B.10.

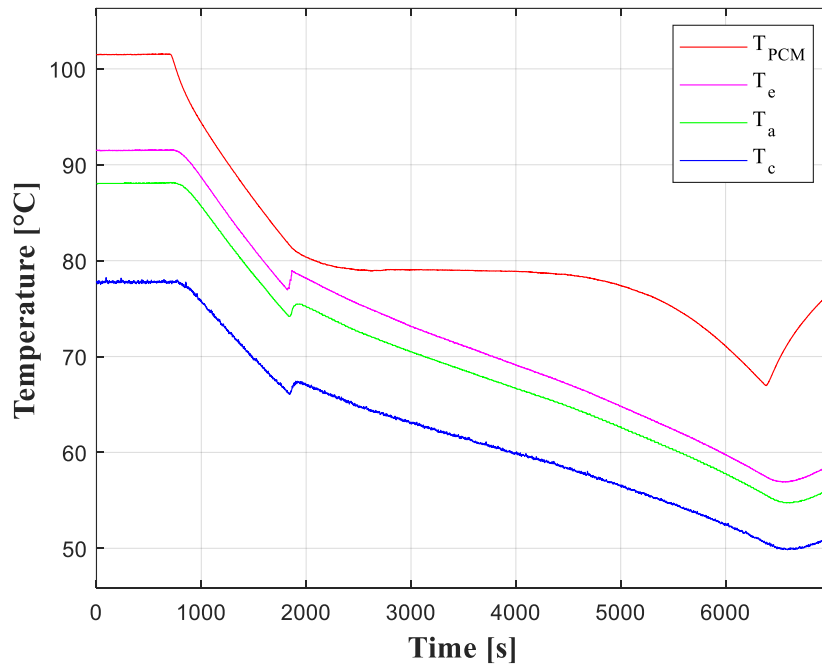


Figure B.5. Temperatures as a function of time for Test 14 (Table 3.4), with inputs of $\dot{q}_{in} = 60$ W and $v_{\infty} = 6,83$ m/s.

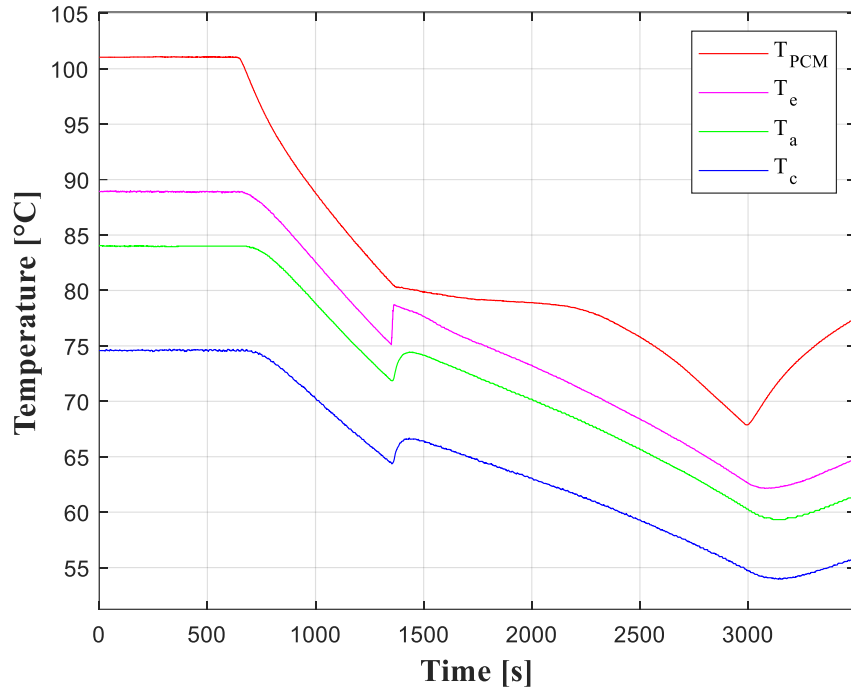


Figure B.6. Temperatures as a function of time for Test 18 (Table 3.4).

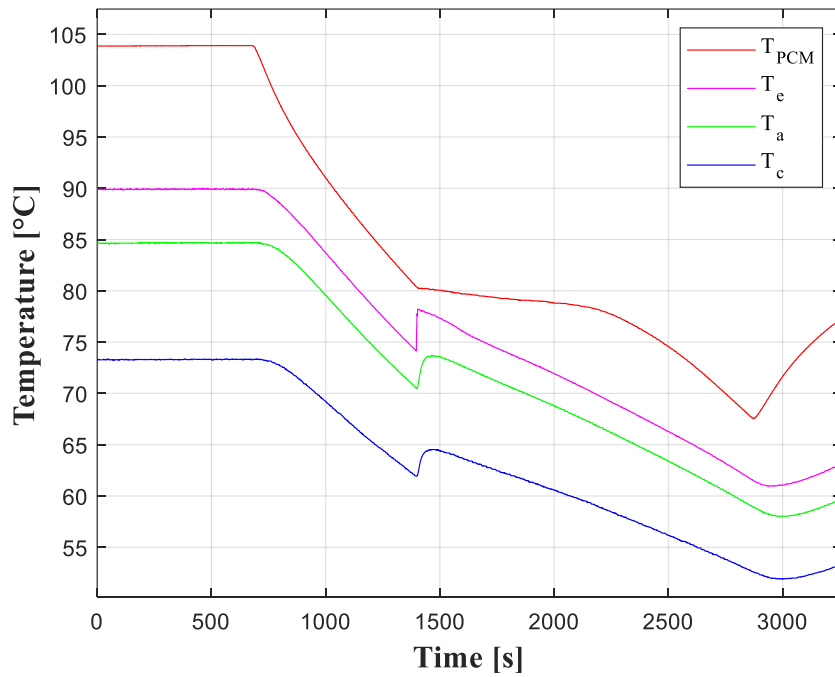


Figure B.7. Temperatures as a function of time for Test 19 (Table 3.5).

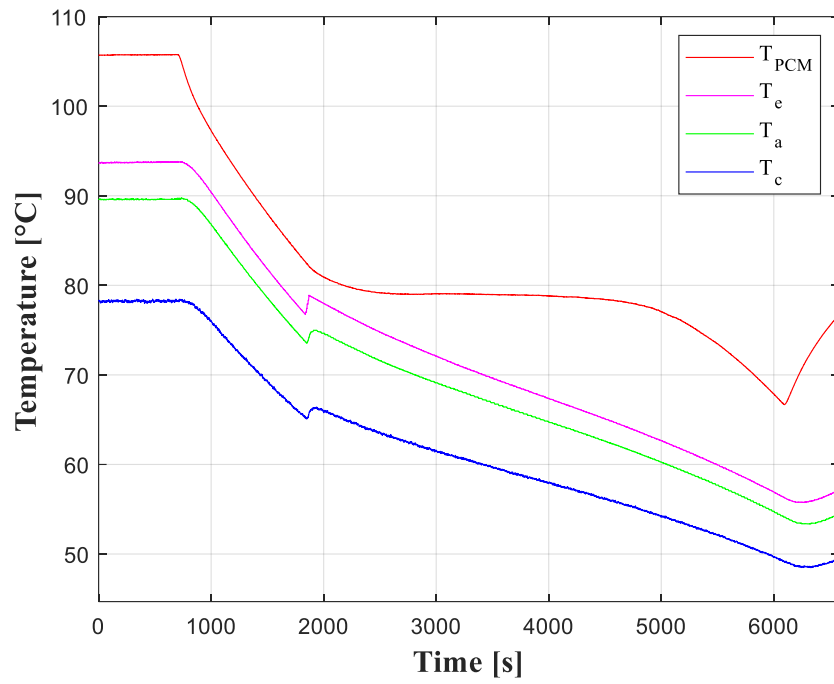


Figure B.8. Temperatures as a function of time for Test 15 (Table 3.4), with inputs of $\dot{q}_{in} = 70$ W and $v_{\infty} = 9,94$ m/s.

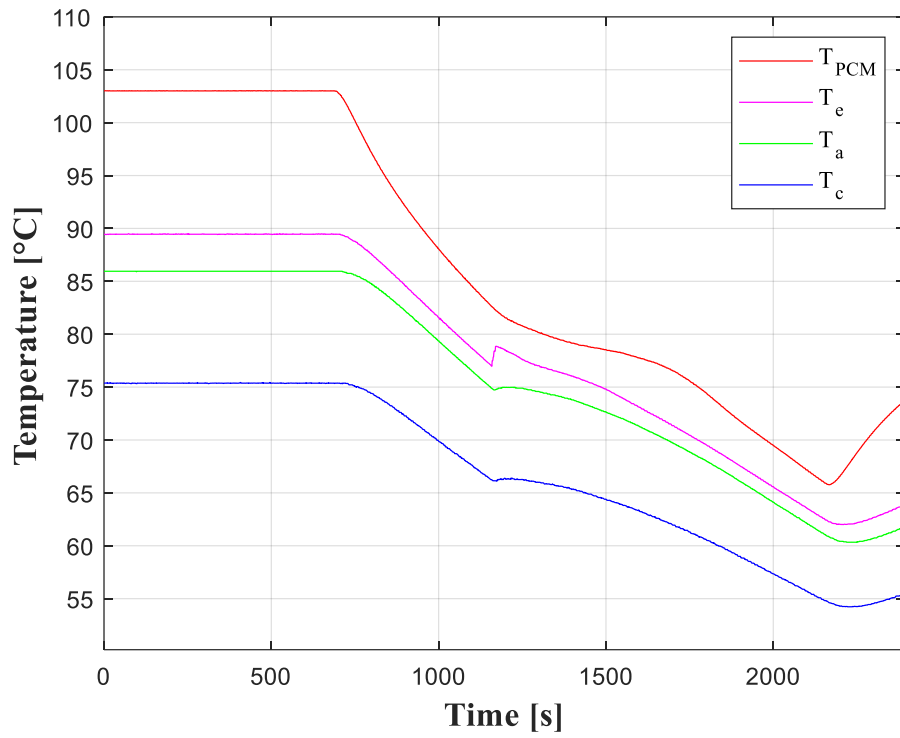


Figure B.9. Temperatures as a function of time for Test 22 (Table 3.4).

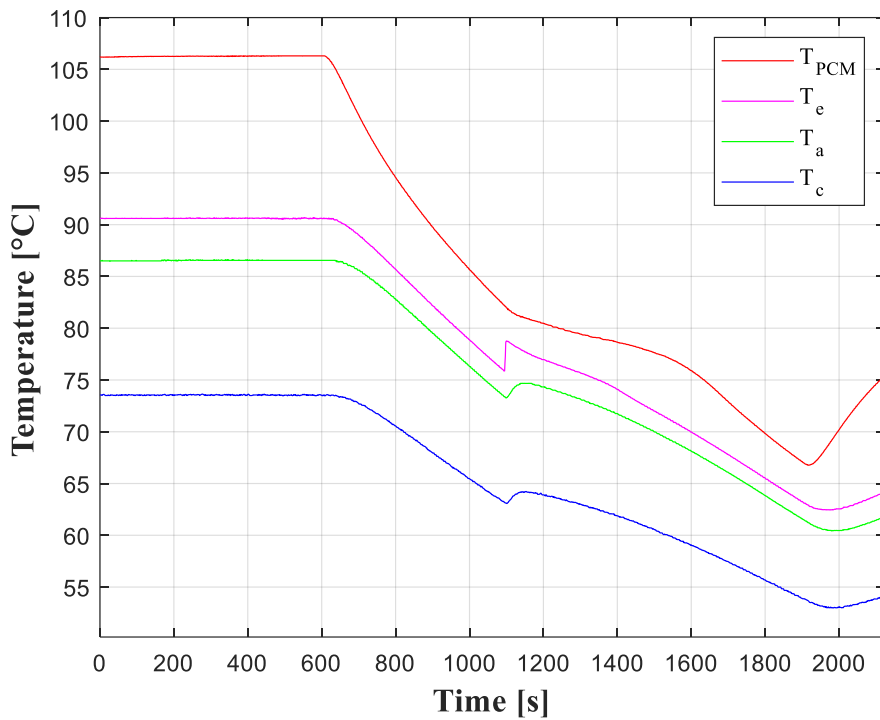


Figure B.10. Temperatures as a function of time for Test 23 (Table 3.4).

B.3 CRITICAL LATENT PERIOD

Further tests results mentioned in Section 4.3 are presented in Figures B.11 to B.20.

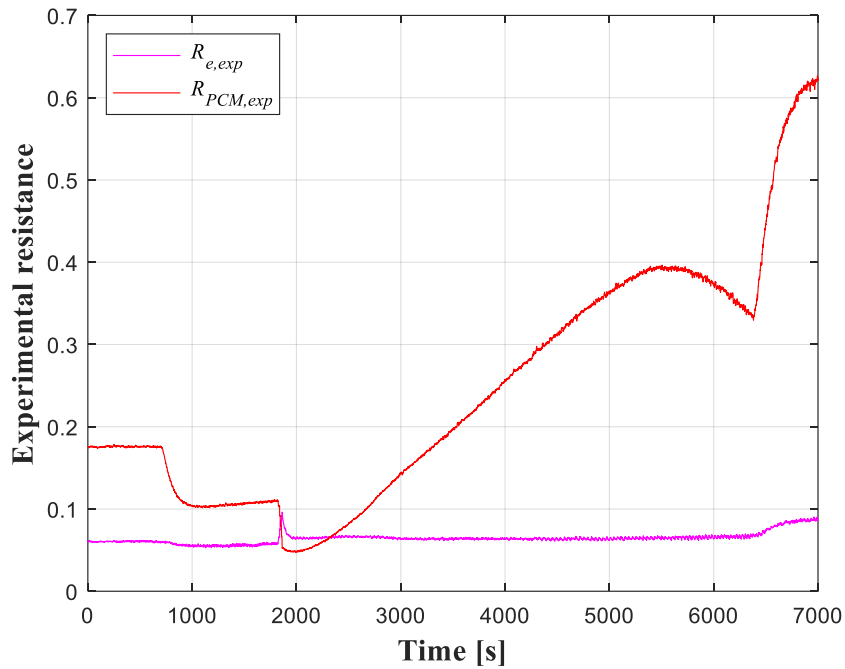


Figure B.11. Experimental evaporator and PCM resistances as a function of time for test 14 (Table 3.4), with PCM container (A).

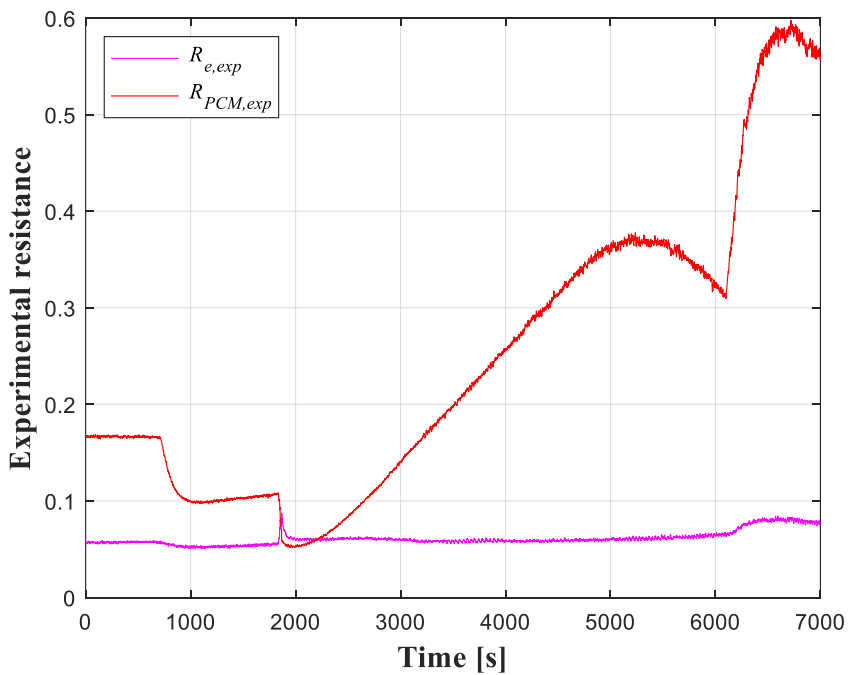


Figure B.12. Experimental evaporator and PCM resistances as a function of time for test 15 (Table 3.4), with PCM container (A).

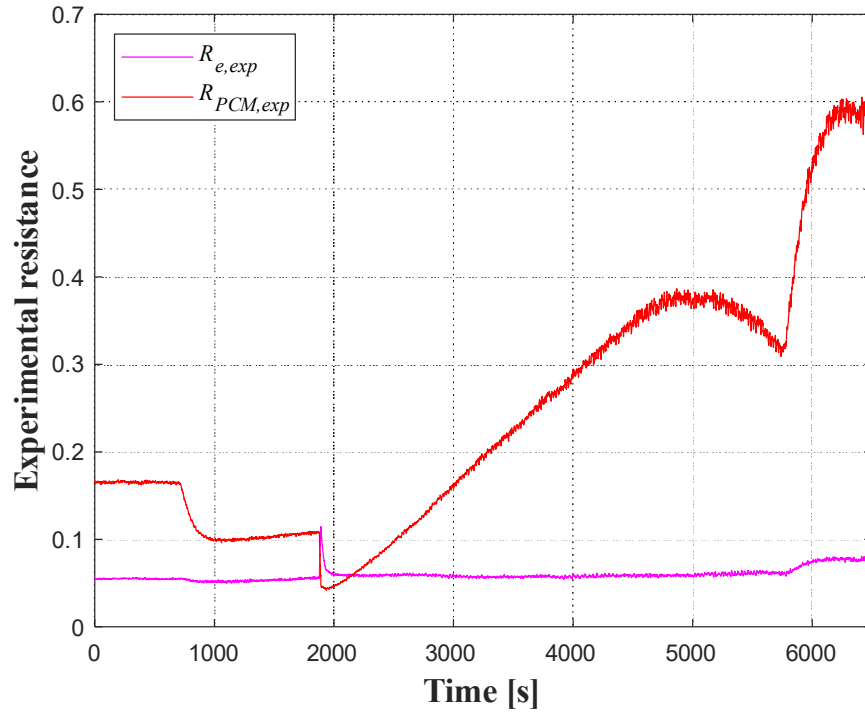


Figure B.13. Experimental evaporator and PCM resistances as a function of time for test 16 (Table 3.4), with PCM container (A).

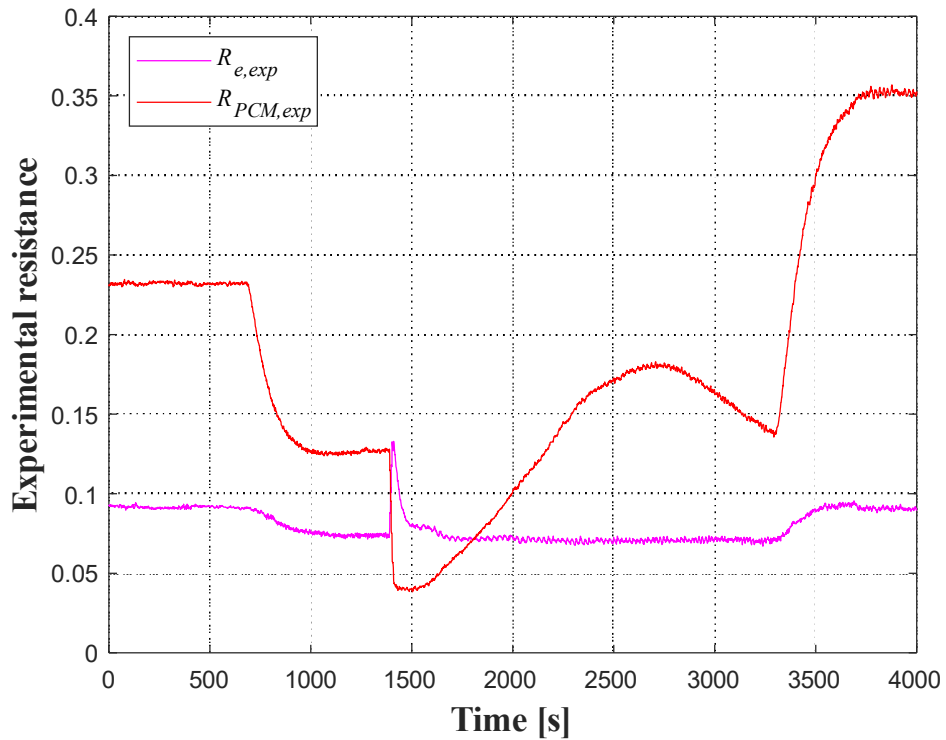


Figure B.14. Experimental evaporator and PCM resistances as a function of time for test 17 (Table 3.4), with PCM container (B).

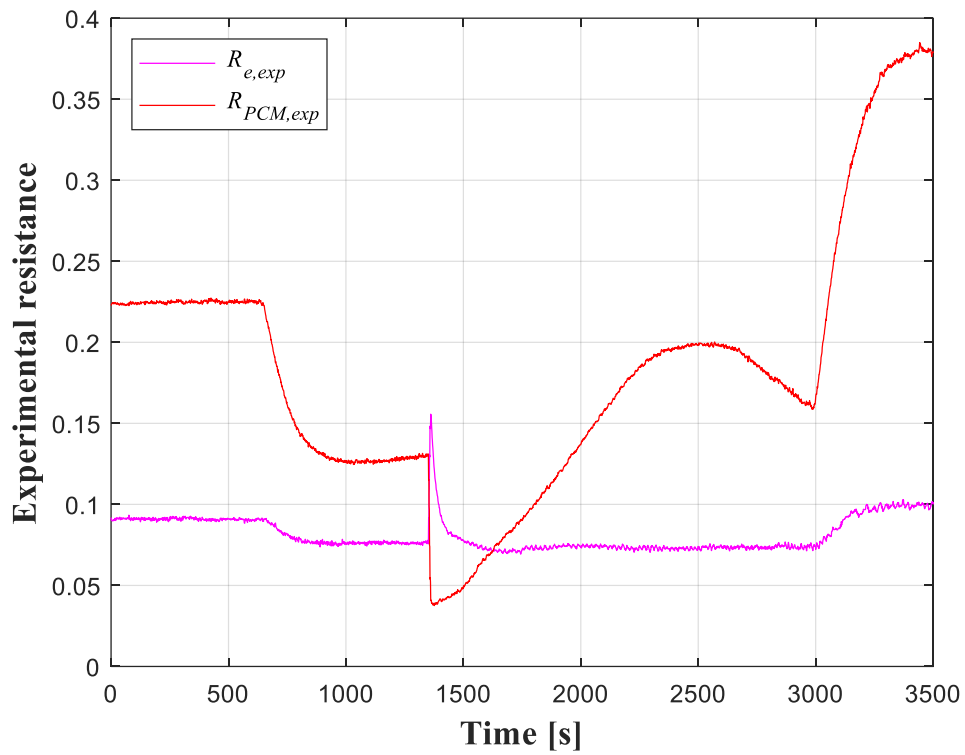


Figure B.15. Experimental evaporator and PCM resistances as a function of time for test 18 (Table 3.4), with PCM container (B).

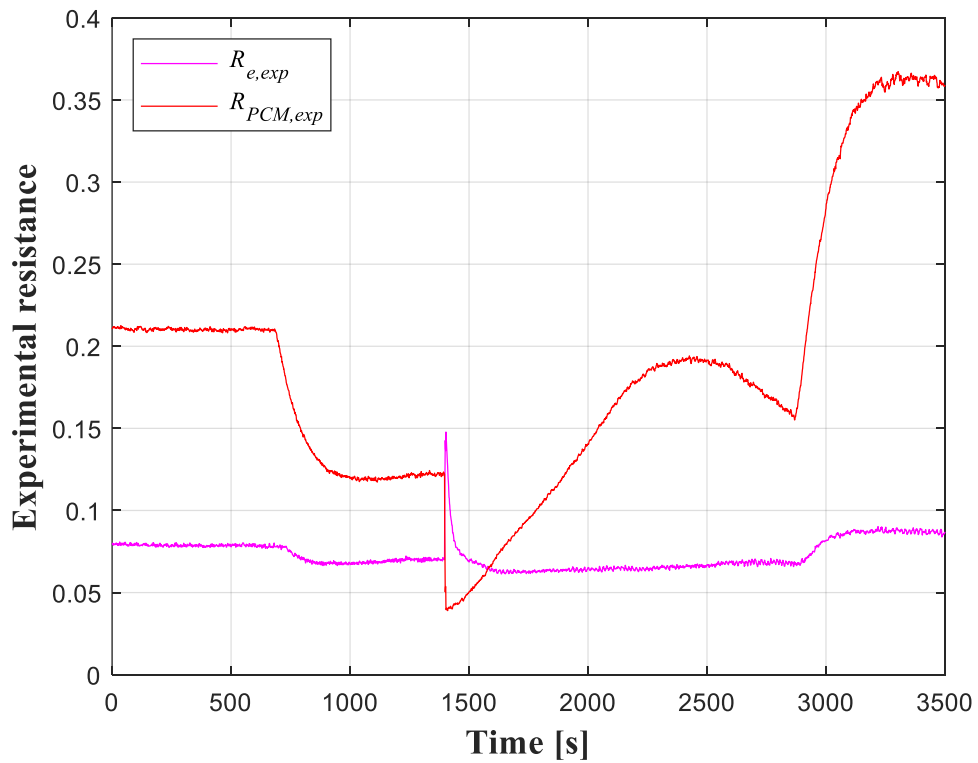


Figure B.16. Experimental evaporator and PCM resistances as a function of time for test 19 (Table 3.4), with PCM container (B).

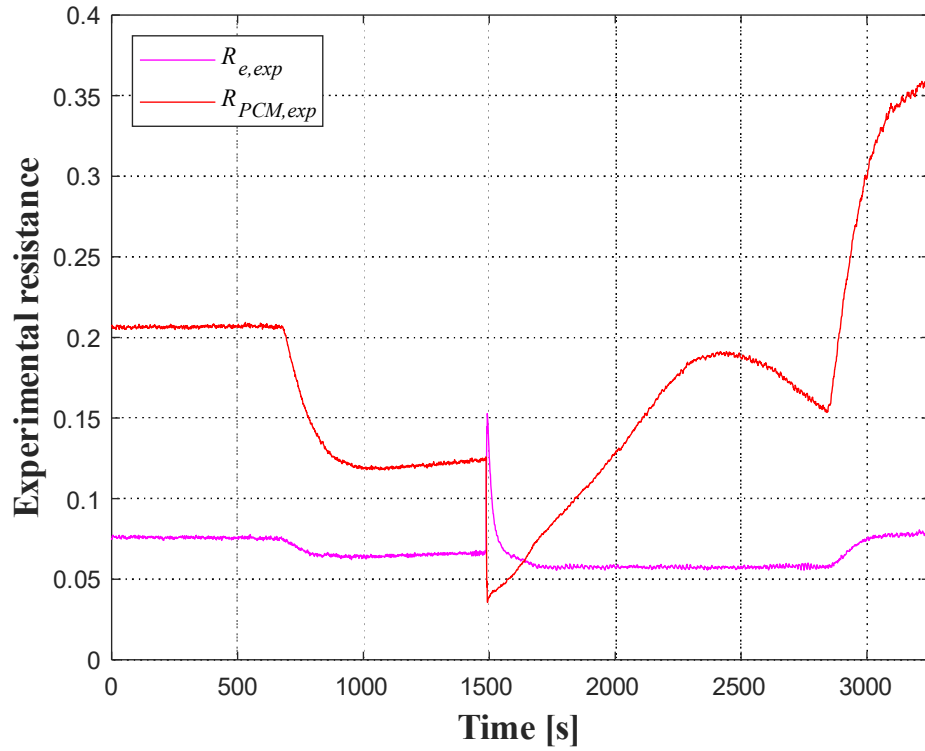


Figure B.17. Experimental evaporator and PCM resistances as a function of time for test 20 (Table 3.4), with PCM container (B).

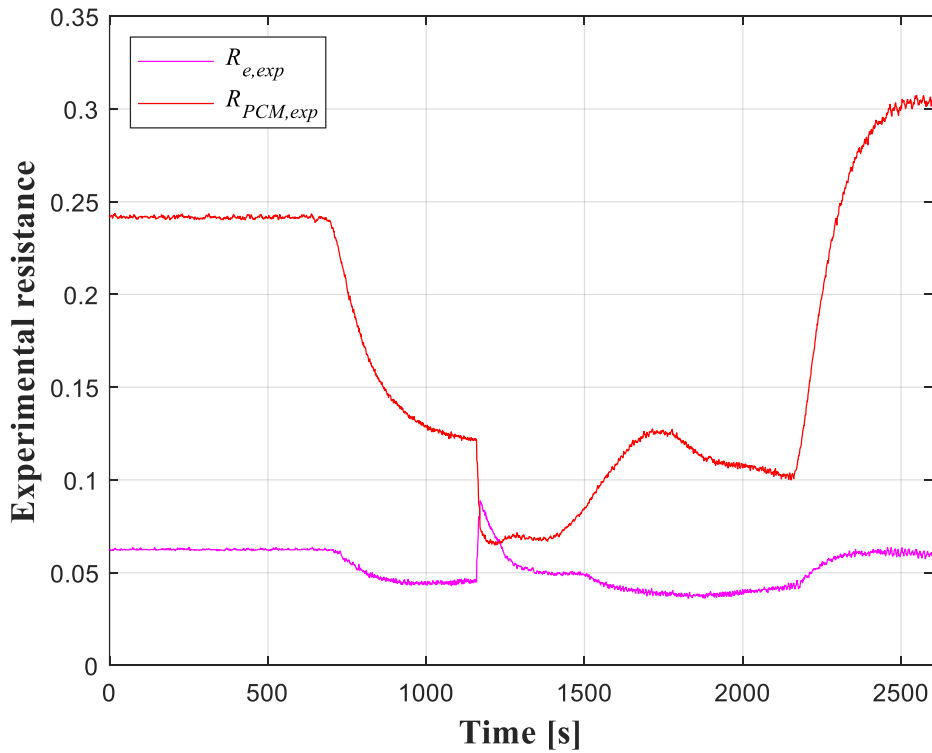


Figure B.18. Experimental evaporator and PCM resistances as a function of time for test 22 (Table 3.4), with PCM container (C).

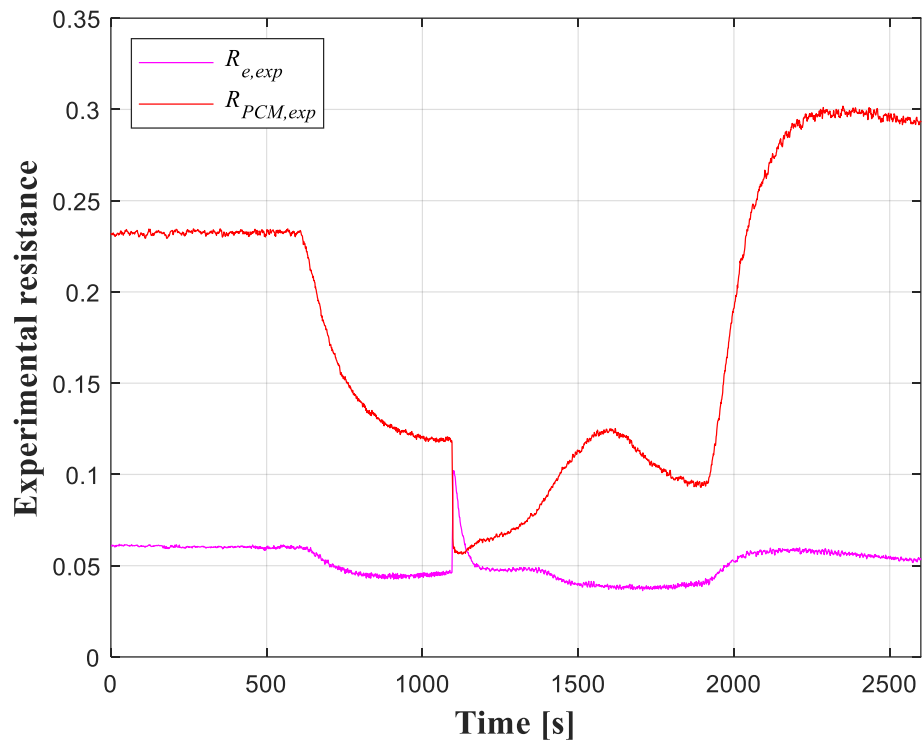


Figure B.19. Experimental evaporator and PCM resistances as a function of time for test 23 (Table 3.4), with PCM container (C).

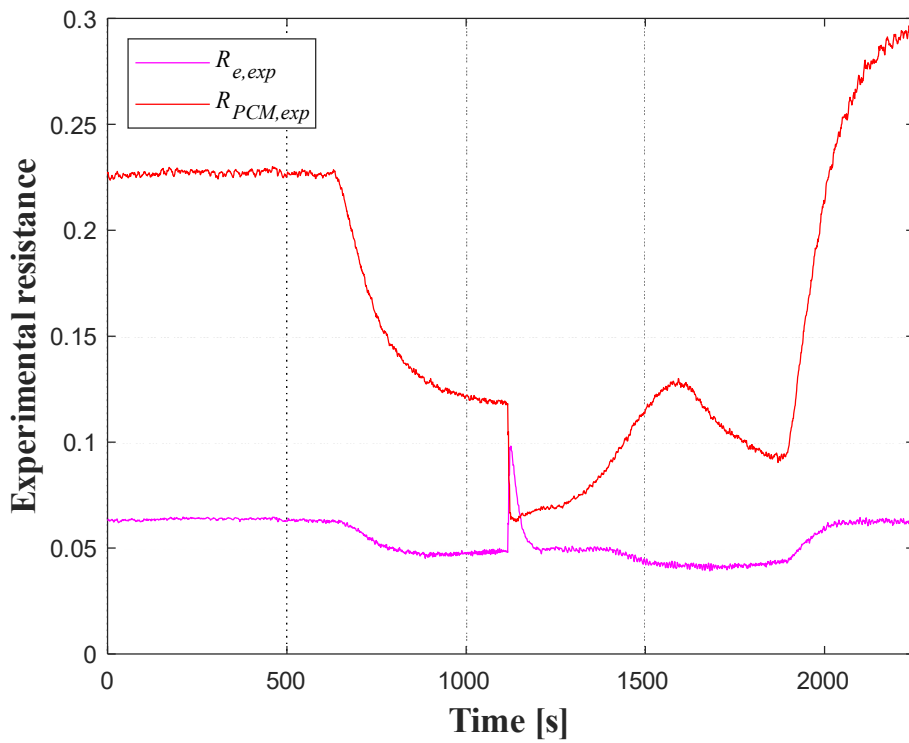


Figure B.20. Experimental evaporator and PCM resistances as a function of time for test 24 (Table 3.4), with PCM container (C).